LA-11893-T
Thesis

UC-410
Issued: August 1990

LA--11893-T

DE90 016725

Measurement of the $2^2S_{1/2}-2^2P_{3/2}$ Fine Structure Interval in Muonium

*Steven Herbert Kettell**

**Guest Scientist at Los Alamos, Temple University, Physics Department, Philadelphia, PA 19122.*

Los Alamos National Laboratory
Los Alamos,New Mexico 87545

Acknowledgements

I would like to thank my advisor Vernon Hughes for his invaluable guidance and helpful insights throughout this work. I would also like to thank all of the people who helped make this experiment possible: Hyo Ahn, Klaus-Peter Arnold, Frank Chmely, Mort Eckhause, Paul Guss, John Kane, Yunan Kuang, Björn Matthias, Hans-Jürgen Mundinger, Benwen Ni, Reiner Schaefer, Kim Woodle, and Jim Reidy, Gisbert zu Putlitz, Michael Gladisch, and Andreas Badertscher. I would like to especially acknowledge the contributions of Herbert Orth for the early design of this experiment and for his encouragement and insights in the development of the low pressure MWPC.

There are numerous people at both LAMPF and Yale who have provided technical and moral support. I would like to acknowledge the help and assistance of many people at Yale, including Bob Broughton, Larry Trudell, Pat Fleming, Barbara Voiges, Harley Pretty and Sara Batter. The experimental and personal support at LAMPF has been tremendous. I would like to especially thank Joe Ivie, Steve Cushing, Bobby Rector, Dick Werbeck, Lew Agnew, Cy Hoffman and Martha Hoehn.

I would like to thank H. Grotch and F. Pipkin for useful discussions and M. Eckhause, V. Hughes, R. Schaefer, K. Woodle, B. Matthias, and M. Hoehn for their careful reading and discussions of this manuscript.

Contents

List of Figures

List of Tables

MEASUREMENT OF THE $2^2S_{1/2}$–$2^2P_{3/2}$ FINE STRUCTURE INTERVAL IN MUONIUM

by

Steven Herbert Kettell

ABSTRACT

The ($2^2S_{1/2}$–$2^2P_{3/2}$) fine structure transition in muonium has been observed for the first time. The measured value is 9895^{+35}_{-30} MHz. This measurement, when included with the theoretical value for the $2^2P_{1/2}$–$2^2P_{3/2}$ fine structure interval, gives a value for the Lamb shift ($2^2S_{1/2}$–$2^2P_{1/2}$) independent of previous direct measurements. From the theoretical value for the fine structure interval, 10921.833(3) MHz [Lep84], the value for the Lamb shift determined from this experiment is 1027^{+30}_{-35} MHz and is in agreement with the prediction of quantum electrodynamics (QED) of 1047.5(3) MHz [Eri88]. Previous experimental values for the Lamb shift ($2^2S_{1/2}$–$2^2P_{1/2}$) in muonium are 1070^{+12}_{-15} MHz [Ora84a] and 1042^{+21}_{-23} MHz [Woo90]. Combining this result with these previous results gives a new experimental value of 1058^{+10}_{-12} for the Lamb shift in muonium. Muonium, the bound state of two structureless leptons (μ^+e^-), is an ideal system for testing bound state quantum electrodynamics (QED) because of the lack of hadronic structure as exists in the hydrogen system.

The measurement makes use of the technique of atomic beam microwave spectroscopy. Muonium atoms (μ^+e^-) in the 2S state are produced by the beam-foil technique at the Clinton P. Anderson Meson Physics Facility (LAMPF) with a low momentum, sub-surface muon beam. A variable frequency microwave field is applied to drive the atoms from the 2S to the 2P states, with the subsequent observation of the Lyman alpha photon from the decay of the 2P state to the 1S ground state. The frequency is varied from 9.0–11.0 GHz, driving the F=0→F=1, F=1→F=1 and F=1→F=2 transitions.

Chapter 1

Introduction

Muonium (M), an atom consisting of two structureless leptons—a muon (μ^+) and an electron (e^-), is an ideal system for testing bound-state quantum electrodynamics (QED) [Hug77]. With both constituents leptons, there are no contributions arising from hadronic interactions. In particular, corrections to the energy levels due to the finite size of the nucleus are absent. Therefore, a measurement of the Lamb shift in muonium can provide a more stringent test of QED than the measurement of the Lamb shift in hydrogen, in which the electromagnetic radius of the proton and its uncertainty must be taken into account.

The measurement of the Lamb shift ($2^2S_{1/2}$–$2^2P_{1/2}$ interval) in hydrogen [Lam47] stimulated the development of modern QED [Bet47]. Lamb's and co-workers' extensive measurements of the fine structure of hydrogen [Lam50,Lam51,Lam52a] and deuterium also provided the best value at the time for the fine structure constant α [Lam52b,Tri53,Day53]. Recent precision measurements of the Lamb shift in hydrogen give values of 1057.845(9) MHz [Lun81] for the $2^2S_{1/2}$–$2^2P_{1/2}$ transition and 9911.117(41) MHz [Saf80] for the $2^2S_{1/2}$–$2^2P_{3/2}$ transition. The theoretical values are 1057.867(11) MHz [Eri88] and 9911.177(11) MHz [Lep84], respectively, using the most recent value for the proton radius [Sim80]. The most recent value for the radius of the proton, $\langle r \rangle_{rms}$=0.862(12) fm, however, differs from the previously accepted value of 0.805(11) fm [Han63] by 3.5 standard deviations. These different values correspond to contributions of 0.145(4) MHz or 0.127(3) MHz respectively

Experimental Measurement	(MHz)
Direct measurements of the $2^2S_{1/2}$–$2^2P_{1/2}$ interval	
Andrews and Newton [And76]	1057.862(20)
Lundeen and Pipkin [Lun81]	1057.845(9)
Pal'chikov [Pal83]	1057.8514(19)
From Measurements of the $2S_{1/2}$–$2P_{3/2}$ interval	
Cosens and Vorburger [Cos70]	1057.874(40)
Kaufman, *et al.* [Kau71]	1057.664(30)
Shyn, *et al.* [Shy71]	1057.794(60)
Safinya *et al.* [Saf80]	1057.927(41)
Weighted average	1057.851(2)
Theory [Eri88]	1057.867(11)

Table 1.1: Measurements of the Lamb shift in hydrogen.

to the calculation of the Lamb shift in hydrogen, a difference of 0.018 MHz. The errors on the QED contribution to the Lamb shift in hydrogen are smaller than the uncertainty from the choice of the proton radius. Therefore the measurement of the Lamb shift in hydrogen is another determination of the electromagnetic radius of the proton [Kin84]. A summary of the experimental and theoretical status of the Lamb shift in hydrogen is given in Table 1.1.

The muonium atom was discovered in 1960 [Hug60] at the Nevis cyclotron in an experiment in which muons were stopped in an Ar gas target. Important measurements of the ground state hyperfine interval $\Delta\nu$ [Mar82] have contributed to our knowledge of the fundamental constants and have been a fertile testing ground for bound-state QED. However, any muonium atoms formed in the 2S state in a gas target will be rapidly quenched by collisions with other atoms. In 1980, muonium in vacuum was discovered [Bol81] at the Clinton P. Anderson Meson Physics Facility(LAMPF) using a beam-foil technique. With the discovery of vacuum muonium came the first opportunity for observing muonium in the 2S state and the ability

to measure the Lamb shift [Bad84a,Ora84b].

The muonium atom has also served as a testing ground for the standard model of the electroweak interaction [Gla61,Wei67,Sal68], through searches for the conversion of muonium to antimuonium. The conversion of muonium to antimuonium ($M \rightarrow \overline{M}$) is also suppressed by collisions. The use of beam-foil muonium in vacuum [Ni87], and more recently, thermal muonium in vacuum [Hub88,Mun89,Hub89] have led to substantially lower limits on this rare lepton-number violating decay than was possible in earlier experiments using gas targets [Ama68].

The purely QED value for the Lamb shift in muonium differs from that for hydrogen primarily because of reduced mass and relativistic recoil terms. The uncertainty in the theoretical value of the Lamb shift in muonium is larger than that in hydrogen because the uncalculated terms of the expansion in the electron/nucleus mass ratio are larger by a factor of ~ 9 (m_e/M_μ=1/200 while m_e/M_p=1/1800). Improvements in the theoretical uncertainty appear straightforward.

Measurement of the fine-structure interval $2^2S_{1/2}$–$2^2P_{3/2}$ provides an independent technique for determining the muonium Lamb shift. The experiment detailed in this paper uses a fast atomic beam, produced by the beam foil technique [Ber77]. A microwave resonance method is used to drive the atomic transition with a flop-in technique [Ram56]. Flop-in implies that the Lyman alpha photons from those atoms quenched by the microwaves are observed directly, as compared to a flop-out experiment, in which atoms in the 2S state *not* quenched by the microwaves are observed in a subsequent detector system. The microwaves excite the normal modes of a low Q cavity, with windows for the observation of the Ly_α radiation.

A new transition, the $2^2S_{1/2} \rightarrow 2^2P_{3/2}$ interval has been measured in the muonium atom. This measurement complements previous spectroscopic measurements in muonium: the ground state hyperfine interval $\Delta\nu$, the $2^2S_{1/2} \rightarrow 2^2P_{1/2}$ Lamb shift and the observation of the $1^2S \rightarrow 2^2S$ transition [Chu88]. This measurement provides an independent value for the Lamb shift in muonium to compare to earlier direct measurements. In addition, this measurement can be combined with the measurements of the $2^2S_{1/2} \rightarrow 2^2P_{1/2}$ interval to determine the value of the $2^2P_{1/2} \rightarrow 2^2P_{3/2}$ fine-structure interval. The current experimental precision is at

the same level as the expected isotope shift relative to hydrogen.

Chapter 2

Theory

The muonium atom can be thought of as a light isotope of hydrogen with much of its general structure similar to that of hydrogen. The primary differences in the energy levels arise from proton structure and reduced mass effects. Since muonium consists only of leptons, its energy levels can be calculated precisely by QED. In particular, there are no corrections for the finite size of the nucleus as there are in hydrogen. This makes muonium an ideal system for testing bound state QED.

In muonium, as in hydrogen, the 2S state is metastable, with a radiative lifetime of 1/7 s for decay by two photons; the lifetime of the 2P state is 1.60 ns. The lifetime of the 2S state in vacuum and isolated from external fields is actually dominated by the muon lifetime, $\tau_{\mu^+} = 2.19703(4)\mu$s [Agu88]. The ground state lifetime is also determined by the muon lifetime.

2.1 Energy Levels of the Muonium Atom

Figure 2.1 shows the energies of the n=1 and n=2 levels of the muonium atom (not to scale) and the transitions driven in this experiment. The 1S–2S, fine structure and Lamb shift intervals are smaller than in hydrogen primarily due to the smaller reduced mass in muonium. The hyperfine intervals are larger in muonium than in hydrogen because of the larger magnetic moment of the muon. A complete treatment of the energy levels starts with a fully covariant relativistic two-body

equation such as the Bethe-Salpeter equation [Sal51].

2.1.1 Fine Structure

Expansion of the solution to the Dirac equation in powers of $Z\alpha$ leads to the following expression for the energy levels of a hydrogen-like atom:

$$\frac{E}{mc^2} = 1 - \frac{1}{2}\left(\frac{Z\alpha}{n}\right)^2 - \frac{1}{2}\left(\frac{Z\alpha}{n}\right)^4 \left[\frac{n}{(j+\frac{1}{2})} - \frac{3}{4}\right] - \frac{1}{8}\frac{(Z\alpha)^6}{n^3(j+\frac{1}{2})^3}\left[1 + 3\frac{(j+\frac{1}{2})}{n} - 6\frac{(j+\frac{1}{2})^2}{n^2}\right] + \ldots \quad (2.1)$$

where j is the electron angular momentum quantum number and n is the principal quantum number. In muonium $Z = 1$, but will be left explicitly in the formulas to indicate the origin of terms from the Coulomb binding between the muon and the electron as distinguished from terms arising from radiative corrections. This leads to a fine structure splitting in the n=2 level of

$$\Delta E = \frac{(Z\alpha)^4 mc^2}{32}[1 + \frac{5}{8}(Z\alpha)^2] \,, \quad (2.2)$$

for an infinitely massive nucleus. An expansion of the relativistic two-body Breit equation gives a correction proportional to $(m_e/M_\mu)^2$ [Bar55]. The correction to the leading term is

$$\Delta E = \frac{(Z\alpha)^4 mc^2}{32}\left[1 - \left(\frac{m_e}{M_\mu}\right)^2\right]\left(\frac{m_R}{m_e}\right)^3 . \quad (2.3)$$

There is in addition a contribution to the fine structure arising from the anomalous magnetic moment of the electron, which contributes an energy level shift of

$$\delta E^{mm}(n,\ell) = \frac{\alpha(Z\alpha)^4 mc^2}{2\pi n^3}\frac{C_{\ell j}}{2\ell+1} \quad (2.4)$$

where $C_{\ell j} = 1/(\ell+1)$ for $j = \ell+1/2$ states and $C_{\ell j} = -1/\ell$ for $j = \ell-1/2$ states, and ℓ is the orbital angular momentum quantum number. The reduced mass corrections to the S states are given by $(m_R/m_e)^3$ and to the P states by $(m_R/m_e)^2$ [Bar55].

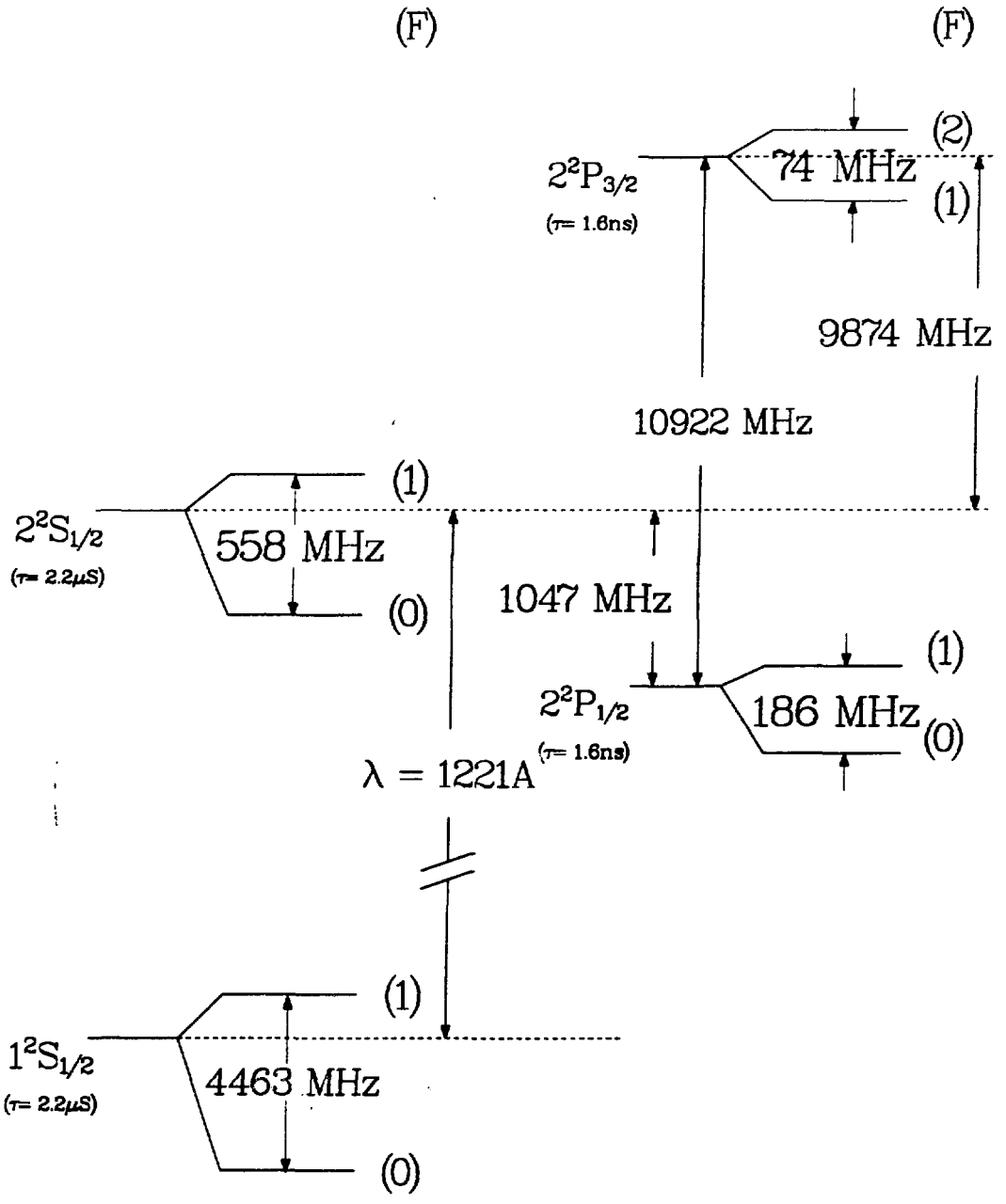

Figure 2.1: Muonium n=1,2 Energy Levels

Constant	Value
α	1/137.035 989 5(61) [Coh87]
c	2.997 924 58 $\times 10^{10}$ cm/ns [Coh87]
R_∞	109 737.315 72(4) cm^{-1} [Agu88,Bir89]
$a_e = (g_e - 2)/2$	1.159 652 193(10) $\times 10^{-3}$ [Coh87]
$(m_R/m_e)^{-1} = 1 + m_e/M_\mu$	1.004 836 332 18(71) [Coh87]
m_e/M_μ	4.836 332 18(71) $\times 10^{-3}$ [Coh87]
$(m_R^H/m_e)^{-1} = 1 + m_e/M_p$	1.000 544 617 013(11) [Coh87]
m_e/M_p	5.446 170 13(11) $\times 10^{-4}$ [Coh87]

Table 2.1: Fundamental Constants

The complete expression for ΔE is given by

$$\begin{aligned} \Delta E &= \frac{Z^4\alpha^2 R_\infty c}{16}\left\{\left[1+\frac{5}{8}(Z\alpha)^2\right]\left[\frac{m_R}{m_e}\right] - \left[\frac{m_e}{M_\mu}\right]^2\left[\frac{m_R}{m_e}\right]^3\right. \\ &\quad \left. + 2a_e\left[\frac{m_R}{m_e}\right]^2 - \frac{\alpha}{\pi}(Z\alpha)^2[\ln(Z\alpha)^{-2} + \delta_{FS}]\right\} \\ &= 10921.833(2) \end{aligned} \tag{2.5}$$

where $\delta_{FS} = 11/24 \pm 3/2$ represents Erickson's estimate of the uncalculated higher order corrections arising from the admixture of the small $2^2S_{1/2}$-like components of the $2^2P_{1/2}$ state [Eri77]. The constants used in evaluating Equation 2.5 and in future sections are given in Table 2.1. The constant c is the speed of light in vacuum, α is the fine structure constant, R_∞ is the Rydberg constant for infinite mass, a_e is the electron anomalous moment, m_R is the reduced mass for the muonium atom, and m_R^H is the reduced mass for the hydrogen atom. The uncertainty in ΔE arises mainly from the uncertainty in the estimate of δ_{FS}. Note that this fine structure interval in muonium, 10921.833(2) MHz, is smaller than the corresponding interval in hydrogen, 10969.040(2) MHz (see Section 2.2).

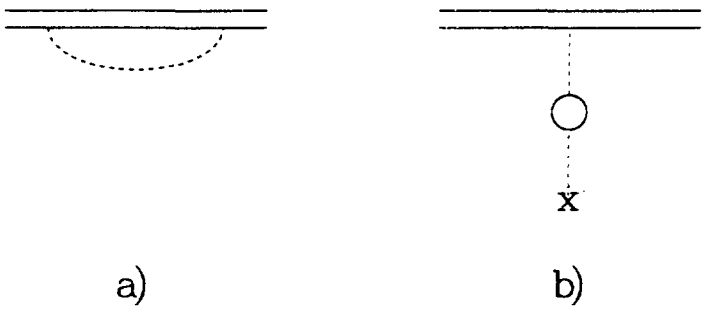

Figure 2.2: Dominant Lamb Shift Diagrams

2.1.2 Lamb Shift

In the relativistic treatment of the muonium atom using the Dirac equation the $2^2S_{1/2}$ and $2^2P_{1/2}$ states are degenerate in energy. This degeneracy is lifted by radiative corrections to the energy levels. In 1947, Bethe made a nonrelativistic calculation of the interaction of the electron in the 2S state with the quantized radiation field. By renormalization of the electron mass, he calculated the Lamb shift to be 1040 MHz [Bet47]. The dominant contribution to the $2^2S_{1/2}$ energy level shift comes from the self energy of the electron , (see Figure 2.2a) where the double line represents the complete bound state wave function. This contribution is of order $\alpha(Z\alpha)^4 \ln(Z\alpha)^{-2}mc^2$. Other second order contributions are from vacuum polarization and the anomalous magnetic moment of the electron. The vacuum polarization term was first calculated by Uehling in 1935 to be -27 MHz [Ueh35]. This term can be represented by the diagram in Figure 2.2b. The anomalous magnetic moment contributes corrections to both the 2S and the 2P states as described by Equation 2.4. There are several fourth order contributions as well. The fourth order self-energy contributions were calculated by Appelquist and Brodsky [App70] (see Figure 2.3).

The complete self-energy contribution to the Lamb shift, including the anomalous magnetic moment terms and all terms up to order $\alpha(Z\alpha)^6$ [Moh75] is given for an infinitely massive nucleus as

$$\mathcal{S}^{SE} = \frac{\alpha(Z\alpha)^4 mc^2}{6\pi}\left\{\ln(Z\alpha)^{-2} - \ln\frac{K_o(2,0)}{K_o(2,1)} + \frac{11}{24} + \frac{3}{8} + \frac{1}{8} +\right.$$

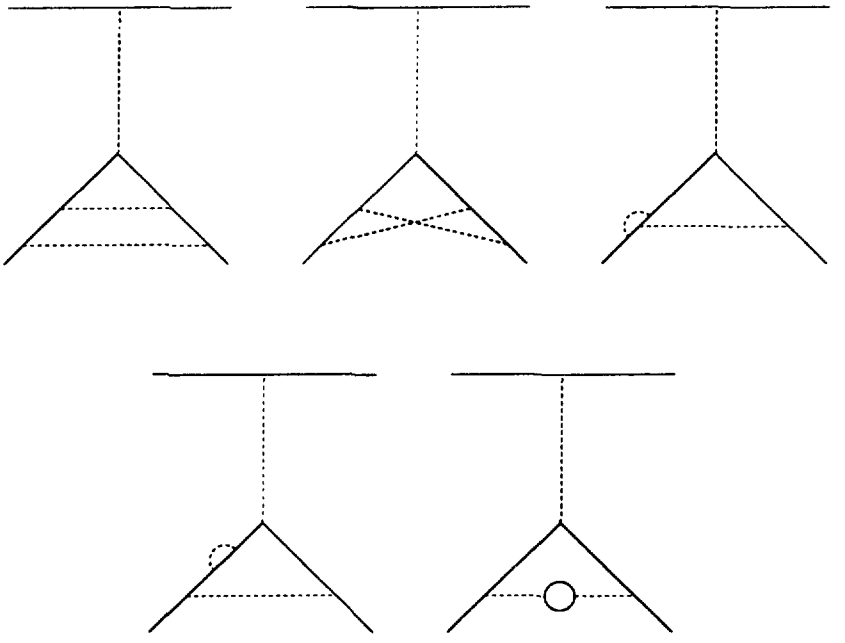

Figure 2.3: Some Fourth Order Lamb Shift Diagrams

$$3\pi Z\alpha(1+\frac{11}{128}-\frac{1}{2}\ln 2)+$$
$$(Z\alpha)^2\left[-\frac{3}{4}\ln^2(Z\alpha)^{-2}+\left(\frac{299}{240}+4\ln 2\right)\ln(Z\alpha)^{-2}+G_{SE}(Z\alpha)\right]\Big\} \quad (2.6)$$

where $G_{SE}(Z\alpha)$ has been numerically evaluated by Mohr as $G_{SE}(Z\alpha) = 23.4 \pm 1.2$. The expression $K_o(2,0)/K_o(2,1)$ is that part of the Bethe logarithm that is not dependent on $(Z\alpha)$ or m_e. Values for the Bethe logarithm for the n=2 state are given by [Kla73]:

$$\begin{aligned} \ln K_o(2,0) &= 2.8117698931(3) \\ \ln K_o(2,1) &= -0.0300167086(3)\ . \end{aligned} \quad (2.7)$$

The reduced mass correction to the self energy is given by multiplying Equation 2.6 by the reduced mass factor $(m_R/m_e)^3$, except for the 1/8 term which comes from a shift of the 2P state and needs to be multiplied by $(m_R/m_e)^2$. In addition there is a mass dependence in the Bethe-log term, which gives a correction $\ln(m_R/m_e)$ term.

The complete expression for the vacuum polarization contribution to the Lamb shift to the same order is given by

$$\mathcal{S}^{VP} = \frac{\alpha(Z\alpha)^4 mc^2}{6\pi}\left\{-\frac{1}{5}+\pi(Z\alpha)\frac{5}{64}-(Z\alpha)^2\left[\frac{1}{10}\ln(Z\alpha)^{-2}+G_{VP}(Z\alpha)\right]\right\} \quad (2.8)$$

The expression $G_{VP}(Z\alpha)$ has been numerically evaluated by Mohr with the result that $G_{VP}(Z\alpha) = -0.5585$.

The pure recoil terms of order $(Z\alpha)^5(m_e^2/M_\mu)$ arise from relativistic treatment of the two body problem and were first calculated by Salpeter [Sal52,Ful54,Gro69]. Additional recoil corrections to these terms have been calculated recently by Erickson and Grotch [Eri88]. Radiative-recoil correction terms of order $\alpha(Z\alpha)^5\,(m_e^2/M_\mu)$ have been calculated by Bhatt and Grotch [Bha85,Bha87a,Bha87b]. Recent reviews [Owe86,Gro88] have included the recoil term of order $(Z\alpha)^4(m_e^3/M_\mu^2)$ [Bar55].

The dimensionless expansion parameters for calculating the Lamb shift are

- $Z\alpha$ characterizes the strength of the interaction between μ^+ and e^-.
- α characterizes the interactions with the quantized radiation field.

- m_e/M_μ characterizes effects from reduced mass and other recoil interactions.

The expansion in m_e/M_μ contributes corrections at a level that is an order of magnitude larger in muonium than hydrogen. The experimental measurements in muonium are not yet sensitive enough to measure these corrections to the Lamb shift. The Lamb shift interval in the n=2 level is reduced from 1057.867(11) MHz in hydrogen to 1047.485(300) MHz in muonium. The theoretical expression for the Lamb shift in muonium is given in Equation 2.9

$$\begin{aligned}
\mathcal{S} &= \frac{Z^4\alpha^3 R_\infty c}{3\pi} \times \left\{ \left[\ln(Z\alpha)^{-2} - 2.20845 - \ln\left(\frac{m_R}{m_e}\right) \right] \left(\frac{m_R}{m_e}\right)^3 \right. \\
&\quad + \frac{1}{8}\left(\frac{m_R}{m_e}\right)^2 + 2.2962\pi Z\alpha \left(\frac{m_R}{m_e}\right)^3 \\
&\quad + (Z\alpha)^2 \left[-\frac{3}{4}\ln^2(Z\alpha)^{-2} + 3.9184\ln(Z\alpha)^{-2} + G(Z\alpha) \right] \left(\frac{m_R}{m_e}\right)^3 \\
&\quad + 0.323\frac{\alpha}{\pi}\left(\frac{m_R}{m_e}\right)^3 \\
&\quad + Z\left[\frac{1}{4}\ln(Z\alpha)^{-2} + 2.39977 + \frac{3\pi Z\alpha}{4}\left\{ \frac{5}{2} - \ln\left(\frac{2}{Z\alpha}\right) \right\} \right] \frac{m_e}{M_\mu} \\
&\quad \left. - 4.684(9) Z\alpha \frac{m_e}{M_\mu} \right\} - Z^4 \frac{\alpha^2 R_\infty c}{24} \left(\frac{m_e}{M_\mu}\right)^2 \\
&= 1047.485(300)
\end{aligned} \tag{2.9}$$

where $G(Z\alpha) = G_{SE}(Z\alpha) + G_{VP}(Z\alpha) = -24.0(1.2)$. The uncertainty of 0.3 MHz is an estimate of the contribution of uncalculated terms of order $\alpha^3 R_\infty (m_e/M_\mu)^2$ and $\alpha^4 R_\infty (m_e/M_\mu)$

2.1.3 Hyperfine Structure

The hyperfine interaction results from the interaction of the magnetic moment of the nucleus and the angular momentum of the electron and has the form

$$H_{HFS} = a(n, L, J)\mathbf{I} \cdot \mathbf{J} \tag{2.10}$$

where L is the electron orbital angular momentum, J is the electron total angular momentum and I is the nuclear angular momentum. The energy level shift arising

from this interaction is given by the the expectation value

$$< H_{HFS} >= \frac{g_\mu Z^3 \alpha^2 c R_\infty}{n^3} \left(\frac{\mu_\mu}{\mu_B}\right) \left(\frac{m_R}{m_e}\right)^3 \cdot \frac{F(F+1) - I(I+1) - J(J+1)}{(2L+1)J(J+1)} \quad (2.11)$$

where F is the total angular momentum The ground state (1S) hyperfine interval has been a fertile testing ground for QED. The ground state hyperfine splitting can be expressed as

$$\Delta\nu = \epsilon_F(1+\delta) \quad (2.12)$$

where the Fermi contact term ϵ_F is given by

$$\epsilon_F = \frac{8 g_\mu Z^3 \alpha^2 c R_\infty}{3} \left(\frac{\mu_\mu}{\mu_B}\right) \left(\frac{m_R}{m_e}\right)^3 \quad (2.13)$$

and δ represents relativistic, radiative and binding corrections. One obtains the value for ϵ_F by taking $n = 1$ and taking the difference of the expectation values for the two hyperfine levels with $F = 1$ and $F = 0$. Both the experimental [Mar82] and theoretical [Sap83] values for $\Delta\nu$ interval are well determined and are in good agreement. The theoretical value is given as $\Delta\nu$ = 4 463 303.6(1.5)(0.2)(1.0) kHz where the 1.5 kHz error arises from the uncertainty in knowledge of μ_μ/μ_p, the 0.2 kHz error arises from numerical integrations and the 1.0 kHz error arises from uncalculated terms. The experimental measurement gives $\Delta\nu$ = 4 463 302.88(0.15) kHz.

The hyperfine splittings of the n=2 states are necessary for understanding the lineshape in the fine structure interval measurement. To the needed level of accuracy $\Delta\nu$ can be scaled by $1/n^3$ to obtain the hyperfine splitting in the $2^2S_{1/2}$ state. Dividing the ground state measurement $\Delta\nu$ by 8, the hyperfine splitting in the 2S state is given by $\Delta\nu_{(2S_{1/2})}$ = 558 MHz. The splitting in the 2P states can be determined directly from Equation 2.11, with the result that $\Delta\nu_{(2P_{1/2})}$ = 186 MHz and $\Delta\nu_{(2P_{3/2})}$ = 74 MHz.

2.2 The Hydrogen Atom

The theoretical value of the fine structure interval ΔE in the n=2 level ($2^2P_{1/2}$–$2^2P_{3/2}$) in hydrogen can be calculated from Equation 2.5. The result is 10969.040(2)

Term		Muonium MHz	Hydrogen MHz
$\Delta E =$	$Z^4\alpha^2 R_\infty c/16\,\{$	10,949.2853(10)	10,949.2853(10)
	m_R/m_e	−52.6995	−5.9599
	$+\frac{5}{8}(Z\alpha)^2 m_R/m_e$	0.3627	0.3642
	$-[m_e/M_\mu]^2\,[m_R/m_e]^3$	−0.2524	−0.0032
	$+2a_e\,[m_R/m_e]^2$	25.1509	25.3671
	$-\alpha/\pi(Z\alpha)^2[\ln(Z\alpha)^{-2} + \delta_{FS}]\}$	−0.0139(20)	−0.0139(20)
		10,921.833(2)	10,969.040(2)

Table 2.2: Contributions to the Fine Structure in Hydrogen and Muonium

MHz. A summary of the contributions of each of the terms in Equation 2.5 to the splittings in both muonium and hydrogen is given in Table 2.2. The uncertainties in both ΔE in muonium and in hydrogen arise predominantly from the uncertainty in $\delta_{\rm FS}$.

The theoretical value of the Lamb shift interval in the n=2 level of hydrogen is 1057.867(11) MHz [Eri88]. The reduced mass corrections are smaller than for muonium. There is in addition a correction to the 2S state from the finite size of the proton. The theoretical expression for the Lamb shift in hydrogen is given in Equation 2.14.

$$\begin{aligned} \mathcal{S}_H \;=\; & \frac{Z^4\alpha^3 R_\infty c}{3\pi} \times \left\{ \left[\ln(Z\alpha)^{-2} - 2.207909\right] \left(\frac{m_R}{m_e}\right)^3 \right. \\ & + \frac{1}{8}\left(\frac{m_R}{m_e}\right)^2 + 2.2962\pi Z\alpha \left(\frac{m_R}{m_e}\right)^3 \\ & \left. + (Z\alpha)^2 \left[-\frac{3}{4}\ln^2(Z\alpha)^{-2} + 3.9184\ln(Z\alpha)^{-2} + G(Z\alpha)\right] \left(\frac{m_R}{m_e}\right)^3 \right. \\ & + 0.323\frac{\alpha}{\pi}\left(\frac{m_R}{m_e}\right)^3 \end{aligned}$$

Origin	Order	Muonium MHz	Hydrogen MHz
Self Energy	$\alpha(Z\alpha)^4\,[\ln(Z\alpha)^{-2}, 1, Z\alpha, (Z\alpha)^2]$	1085.812	1085.812(9)
Vacuum Polarization	$\alpha(Z\alpha)^4\,[\ln(Z\alpha)^{-2}, 1, Z\alpha, (Z\alpha)^2]$	−26.897	−26.897
Fourth Order	$\alpha^2(Z\alpha)^4$	0.102	0.102
Reduced Mass	$\alpha(Z\alpha)^4 m_e/M\,[\ln(Z\alpha)^{-2}, ...]$	−14.493	−1.646
Relativistic Recoil	$(Z\alpha)^5 m_e/M\,[\ln(Z\alpha)^{-2}, 1, ...]$	3.159	0.356
Higher Order Recoil	$(Z\alpha)^4\left(\frac{m_e}{M}\right)^2$	−0.171	−0.002
Nuclear Structure	$(Z\alpha)^4 m_e^2\langle r_p\rangle^2$	0	0.145(4)
Radiative Recoil	$\alpha(Z\alpha)^5 m_e/\mathrm{M}$	−0.022	−0.003
		1047.9(3)	1057.867(11)

Table 2.3: Contributions to the Lamb Shift in Hydrogen and Muonium

$$
\begin{aligned}
&+Z\left[\frac{1}{4}\ln(Z\alpha)^{-2} + 2.39977 + \frac{3\pi Z\alpha}{4}\left\{\frac{5}{2} - \ln\left(\frac{2}{Z\alpha}\right)\right\}\right]\frac{m_e}{M_\mu} \\
&- 4.684(9)Z\alpha\frac{m_e}{M_\mu}\Bigg\} - Z^4\frac{\alpha^2 R_\infty c}{24}\left(\frac{m_e}{M_\mu}\right)^2 + \frac{1}{6}Z^4\alpha^2 R_\infty c m_e^2 < r_p >^2 \\
= \;& 1057.867(11) \qquad (2.14)
\end{aligned}
$$

A summary the contributions to the Lamb shift in both muonium and hydrogen is given in Table 2.3.

2.3 Non-Resonant Quenching of the 2S State

The 2S state is metastable when free of external perturbations; however, when electric fields are present, the 2S state mixes with the 2P state and rapidly decays

to the ground state. Therefore external electric fields or collisions with other atoms will quench the 2S state. A static magnetic field will also quench the 2S state due to the electric field component induced by the Lorentz transformation of the magnetic field to the rest frame of the atom.

For Stark energies that are small compared to the fine structure splitting ($|\mathbf{E}| < 3.5$ kV/cm), only the $2^2S_{1/2}$ and $2^2P_{1/2}$ need be considered. The lifetimes $\tau_\pm$ of the mixed states can be related to the lifetime τ_p of the 2P state by [Bet77]

$$\tau_\pm = \tau_p \cdot \left[1 + \left(\frac{2b}{\omega_{LS} \pm \sqrt{\omega_{LS}^2 + (2b)^2}}\right)^2\right] \tag{2.15}$$

where b is the matrix element connecting the $2^2S_{1/2}$ and $2^2P_{1/2}$ states and ω_{LS} is the Lamb shift splitting. The Stark matrix element connecting the 2S and 2P states is $\sqrt{3}a_o eE = 2.22E(\mathrm{V/cm})$ MHz (see Section 2.4). At a field of 475 V/cm the Stark splitting is equal to the field-free Lamb shift splitting. Equation 2.15 can be rewritten in terms of the electric field strength as

$$\tau_\pm = \tau_p \cdot \left[1 + \left(\frac{2 \cdot \mathrm{E}/475}{1 \pm \sqrt{1 + 4 \cdot (\mathrm{E}/475)^2}}\right)^2\right] \tag{2.16}$$

where the electric field E is expressed in Volts/cm. This problem can also be treated using the two-level solution given in Section 2.4, but the above expression is sufficient for the current discussion. For small fields this expression can be approximated by

$$\begin{aligned} \tau_- &\simeq \tau_p \left[1 + \left(\frac{475}{\mathrm{E}}\right)^2\right] \\ &\simeq \tau_p \left(\frac{475}{\mathrm{E}}\right)^2 \end{aligned} \tag{2.17}$$

for the long lived state. From Equation 2.17, it can be observed that for E < 26 V/cm, the lifetime of the 2S state will be dominated by the μ^+ lifetime. As the M(2S) atoms enter the active field region the fields become large and the 2S state will be quenched. The lifetime for the long-lived state in the static electric field of 600 V/cm, from Equation 2.16, is $3.2\tau_p = 5$ ns. This is small compared to the average interaction time of 13 ns (see Section 5.3) and most of the M(2S) atoms will be quenched.

We must also consider the effects of motional electric fields, i.e. the effects of the relativistic transformation of stray laboratory magnetic fields into electric fields in the rest frame of the atom. The transformation is given by:

$$\begin{aligned} \mathbf{E}' &= \gamma(\mathbf{E} + \boldsymbol{\beta} \times c\mathbf{B}) - \frac{\gamma^2}{\gamma+1}\boldsymbol{\beta}(\boldsymbol{\beta}\cdot\mathbf{E}) \\ c\mathbf{B}' &= \gamma(c\mathbf{B} + \boldsymbol{\beta} \times \mathbf{E}) - \frac{\gamma^2}{\gamma+1}\boldsymbol{\beta}(\boldsymbol{\beta}\cdot c\mathbf{B}) \end{aligned} \tag{2.18}$$

where $\mathbf{E}'$ and $\mathbf{B}'$ are the electric and magnetic fields in the rest frame of the muonium atom. For the case of zero laboratory electric field, Equation 2.18 reduces to

$$\mathbf{E}' = \gamma\boldsymbol{\beta} \times c\mathbf{B} \tag{2.19}$$

for the electric field in the M rest frame. With the measured magnetic fields and M(2S) velocity distribution, the lifetime τ_- is essentially unchanged from the M(2S) lifetime $\tau_s = 2.197\mu$s.

2.4 Theory of the Resonance Lineshape

The Hamiltonian for the system of atom and field can be written as

$$H = H_o + V \tag{2.20}$$

where H_o is the Hamiltonian for the unperturbed atomic system and V is the perturbation from the external microwave field.

A general solution to the Schrödinger equation can be obtained by expanding the wave function of the atom-field system in eigenfunctions of the unperturbed atomic system

$$\Psi(\mathbf{r},t) = \sum_{n=1}^{\infty} C_n(t)u_n(\mathbf{r})e^{-i\omega_n t} \tag{2.21}$$

where $\hbar\omega_n$ are the eigenenergies and u_n are the eigenfunctions of H_o and $|C_n(t)|^2$ is the probability of being in the state n at the time t. The time dependent Schrödinger equation can be written as

$$i\dot{C}_m(t) = \sum_{n=1}^{\infty} C_n(t)V_{mn}e^{i\omega_{mn}t} + i\frac{\gamma_m}{2}C_m(t) \tag{2.22}$$

where we have allowed for decay of the atomic levels, with decay rate γ_m. The energy difference between the m and n levels is $\omega_{mn} = \omega_m - \omega_n$. If only one sublevel of the $2^2P_{3/2}$ state is near resonance with the microwave field for any given $2^2S_{1/2}$ initial state, all other states can be ignored and Equation 2.22 can be written as:

$$\begin{aligned} \dot{C}_s &= -\frac{\gamma_s}{2}C_s - iV_{sp}e^{i\omega_{sp}t}C_p \\ \dot{C}_p &= -\frac{\gamma_p}{2}C_p - iV_{sp}^{*}e^{-i\omega_{sp}t}C_s \end{aligned} \tag{2.23}$$

where the decay constants are given by $\gamma_s = 0.0004ns^{-1}$ and $\gamma_p = 0.625ns^{-1}$.

The electric field inside of the microwave cavity can be described either in terms of a standing wave or travelling waves. The electric field is given by:

$$\mathbf{E}(\mathbf{x},t) = \mathbf{E}\cos(\mathbf{k}\cdot\mathbf{x} - \nu' t) \tag{2.24}$$

where ν' is the frequency and $\mathbf{k}$ is the wave vector of the travelling wave. The atom will experience a Doppler shifted microwave frequency as it interacts with this field,

$$\nu = \nu'(1 + \mathbf{k}\cdot\boldsymbol{\beta}) \ , \tag{2.25}$$

where ν is the microwave frequency in the atom's rest frame, $\mathbf{k}$ is the wave vector of the microwave field and $\boldsymbol{\beta}$ is the atomic velocity. The waves are counter-propagating so the microwave frequency will be symmetrically shifted up and down as the atom interacts with the two waves. In the electric dipole approximation the interaction energy is given by

$$V = -e\mathbf{E}(\mathbf{x},t)\cdot\mathbf{r} \ . \tag{2.26}$$

If the interaction with each of the waves is treated separately, using the additive approximation [Ben77], the matrix element V_{sp} will be a function of only one frequency and a closed form solution can be obtained. Since there are no external fields the axis of quantization can be chosen to lie along the microwave electric field direction. Then using the rotating wave approximation, in which the component of the field rotating out of phase with the atomic transition is neglected, the matrix elements of the interaction Hamiltonian can be written as

$$V_{sp} = < u_p| - e\mathbf{E}(\mathbf{x},t)\cdot\mathbf{r}|u_s > = \frac{-eE}{2} < u_p|z|u_s > e^{-i\nu t} = be^{-i\nu t} \tag{2.27}$$

The dipole approximation implies that **E**(x,t) is constant over the atomic dimensions.

We can now rewrite Equation 2.23 as

$$\begin{aligned} \dot{C}_s &= -\frac{\gamma_s}{2}C_s + ibe^{i\Omega t}C_p \\ \dot{C}_p &= -\frac{\gamma_p}{2}C_p + ib^*e^{-i\Omega t}C_s \end{aligned} \tag{2.28}$$

where $\Omega = \omega_{sp} - \nu$ and $\omega_{sp} = \omega_s - \omega_p$, is the splitting between the 2S and 2P states. If we differentiate the first equation and substitute the second we obtain

$$\ddot{C}_s + \left(\frac{\gamma_s + \gamma_p}{2} - i\Omega\right)\dot{C}_s + \left(|b|^2 + \frac{\gamma_p\gamma_s}{4} - \frac{i\Omega\gamma_s}{2}\right)C_s = 0 \tag{2.29}$$

If we assume a solution of the form s = $e^{i\mu t}$ and define two new quantities d and γ, such that

$$\begin{aligned} d &= \frac{\gamma_p - \gamma_s}{2} \\ \gamma &= \frac{\gamma_p + \gamma_s}{2} \end{aligned} \tag{2.30}$$

then the two solutions for μ are

$$\mu_\pm = 1/2\left[(\Omega + i\gamma) \pm \sqrt{(\Omega + id)^2 + 4|b|^2}\right] \tag{2.31}$$

Now if we assume that initially the 2P state is unpopulated $[C_p(0) = 0, C_s(0) = 1]$, the expression for $C_p(t)$ can be written

$$C_p(t) = \frac{b}{\mu}e^{-i\Omega t/2}e^{-\gamma t/2}(e^{i\mu_+ t} - e^{i\mu_- t}) \tag{2.32}$$

where μ is the complex Rabi flopping frequency, defined as

$$\mu = \mu_+ - \mu_- = \sqrt{(\Omega + id)^2 + (2b)^2} \tag{2.33}$$

The probability of the atom being in the 2P state at a time t is given by

$$|C_p(t)|^2 = \frac{4|b|^2}{|\mu|^2}e^{-\gamma t}\sin\left(\frac{\mu t}{2}\right)\sin\left(\frac{\mu^* t}{2}\right) \tag{2.34}$$

The complex Rabi flopping frequency μ is the frequency of oscillation between the two atomic levels. The probability of detecting a decay from an atom driven to the

	$\|2^2S_{1/2},0,0>$	$\|2^2S_{1/2},1,0>$	$\|2^2S_{1/2},1,\pm1>$
$<2^2P_{3/2},1,\ 0\|$	$\sqrt{6}ea_oE$	0	0
$<2^2P_{3/2},1,\pm1\|$	0	0	$\mp\sqrt{6}/2ea_oE$
$<2^2P_{3/2},2,\ 0\|$	0	$\sqrt{6}ea_oE$	0
$<2^2P_{3/2},2,\pm1\|$	0	0	$\pm3/\sqrt{2}ea_oE$
$<2^2P_{3/2},2,\pm2\|$	0	0	0

Table 2.4: Electric dipole matrix elements between $2S_{1/2}$ and $2P_{3/2}$ states

2P state is given by integrating Equation 2.34 over the interaction time with the microwave field, from $t' = 0$ to $t' = t$ [Kus59]

$$I(t) = \gamma_p \int_0^t |C_p(t')|^2 dt' \tag{2.35}$$

where the factor of γ_p accounts for the decay from the 2P state. This expression can be evaluated, using Equations 2.33 and 2.34 as

$$\begin{aligned} I(t) &= \frac{2|b|^2 e^{-\gamma t}}{|\mu|^2} \times \left(\frac{\gamma\cos(xt) - x\sin(xt)}{\gamma^2 + x^2} - \frac{\gamma\cosh(yt) + y\sinh(yt)}{\gamma^2 - y^2} \right) + \\ & \frac{2|b|^2\gamma}{\gamma_s} \times \left[\Omega^2 + \gamma^2 \left(1 + \frac{4|b|^2}{\gamma_p\gamma_s} \right) \right]^{-1} \end{aligned} \tag{2.36}$$

where:

$$\begin{aligned} x &= \mathrm{Re}(\mu) \\ y &= \mathrm{Im}(\mu) \end{aligned} \tag{2.37}$$

The matrix elements between sublevels of the $2^2S_{1/2}$ and $2^2P_{3/2}$ states,

$$2b = -eE < u_p(\mathbf{r})|z|u_s(\mathbf{r}) > = -eE < 2^2P_{3/2}, F', m'_F|z|2^2S_{1/2}, F, m_F > \tag{2.38}$$

are given in Table 2.4. For the static case $2b$ is replaced by b and the matrix elements b between the $2^2S_{1/2}$ and $2^2P_{1/2}$ states are given in Table 2.5. All of the allowed transitions between the $2^2S_{1/2}$ and $2^2P_{3/2}$ states are driven in this experiment.

	$\|2^2S_{1/2},0,0>$	$\|2^2S_{1/2},1,0>$	$\|2^2S_{1/2},1,\pm1>$
$<2^2P_{1/2},0,\ 0\|$	0	$-\sqrt{3}ea_oE$	0
$<2^2P_{1/2},1,\ 0\|$	$-\sqrt{3}ea_oE$	0	0
$<2^2P_{1/2},1,\pm1\|$	0	0	$\mp\sqrt{3}ea_oE$

Table 2.5: Electric dipole matrix elements between $2S_{1/2}$ and $2P_{1/2}$ states

In a static electric field, where the $2^2S_{1/2}$ states will couple most strongly to the $2^2P_{1/2}$ states, the two-level approximation is a good one. Each of the 2S sublevels couples to only one 2P sublevel. Likewise, in the microwave experiment the $|2^2S_{1/2},0,0>$ and $|2^2S_{1/2},1,0>$ states each couple to only one of the $2^2P_{3/2}$ states.

The two-level approximation of course does not give the complete description for the interaction of the $|2^2S_{1/2},1,\pm1>$ states with the $2^2P_{3/2}$ states. Because the frequency separation between the 2P sublevels is less than the natural line width, the $|2^2S_{1/2},1,\pm1>$ state and the $|2^2P_{3/2},1,\pm1>$ and $|2^2P_{3/2},2,\pm1>$ states are significantly coupled, hence a correct treatment would involve solution of the three-level problem. The decay rate of the 2P states is very large, larger than the oscillation frequency between the 2S and 2P states, and there is no appreciable probability for an atom to be driven to one of the 2P levels, back to the 2S level and to the other 2P level. There is a coupling through the depopulation of the 2S state to the third level. This depopulation is accounted for through a reweighting of the 2S state populations, as is discussed in Chapter 5.

The treatment of the interaction of the atom with the counter-propogating electromagnetic waves neglecting interference terms is not a full description of the interaction. However, the error introduced should be small. Under the simplifying assumptions of an infinite interaction time and equal decay rates of the two levels, for the field strengths in this experiment, the transition probability under the additive approximation is very nearly the same as that obtained from a complete numerical integration [Ben77].

Chapter 3

Muonium Production

Located in Los Alamos, New Mexico, LAMPF is a half-mile long linear accelerator, accelerating protons to 800 MeV at up to 1 mA of average current with a duty factor between 6%–9%. The average duty factor over the course of this experiment was 6.8% and the average current was 830 μA. The repetition rate varies from 60 to 120 Hz and the beam gate length is typically 800 μs. The proton beam passes through two targets in the Area A experimental hall. The second of these targets, the A-2 target, is a 4.0-cm thick graphite disk.

3.1 The LAMPF Stopped Muon Channel

The A-2 target is open to the Stopped Muon Channel (SMC), where this experiment is performed. A drawing of the SMC is shown in Figure 3.1. The SMC consists of 21 quadrupole and 4 dipole magnets that are fixed in place. An additional 6 removable quadrupole magnets are installed as a channel extension in the Cave-A section of the SMC. This extension allows the experimental apparatus in the downstream portion of Cave-A to be left in place when other experiments are using the SMC. An $\mathbf{E} \perp \mathbf{B}$ separator, or Wien filter, a vacuum valve, and a thin 1.5 μm Mylar gas barrier are also installed in the Cave-A part of the SMC. The experimental apparatus is connected to the channel after the last quadrupole magnet, QM27. Downstream of the QM27 field clamp by 30 cm is a beam collimator, with the muon counter, a low

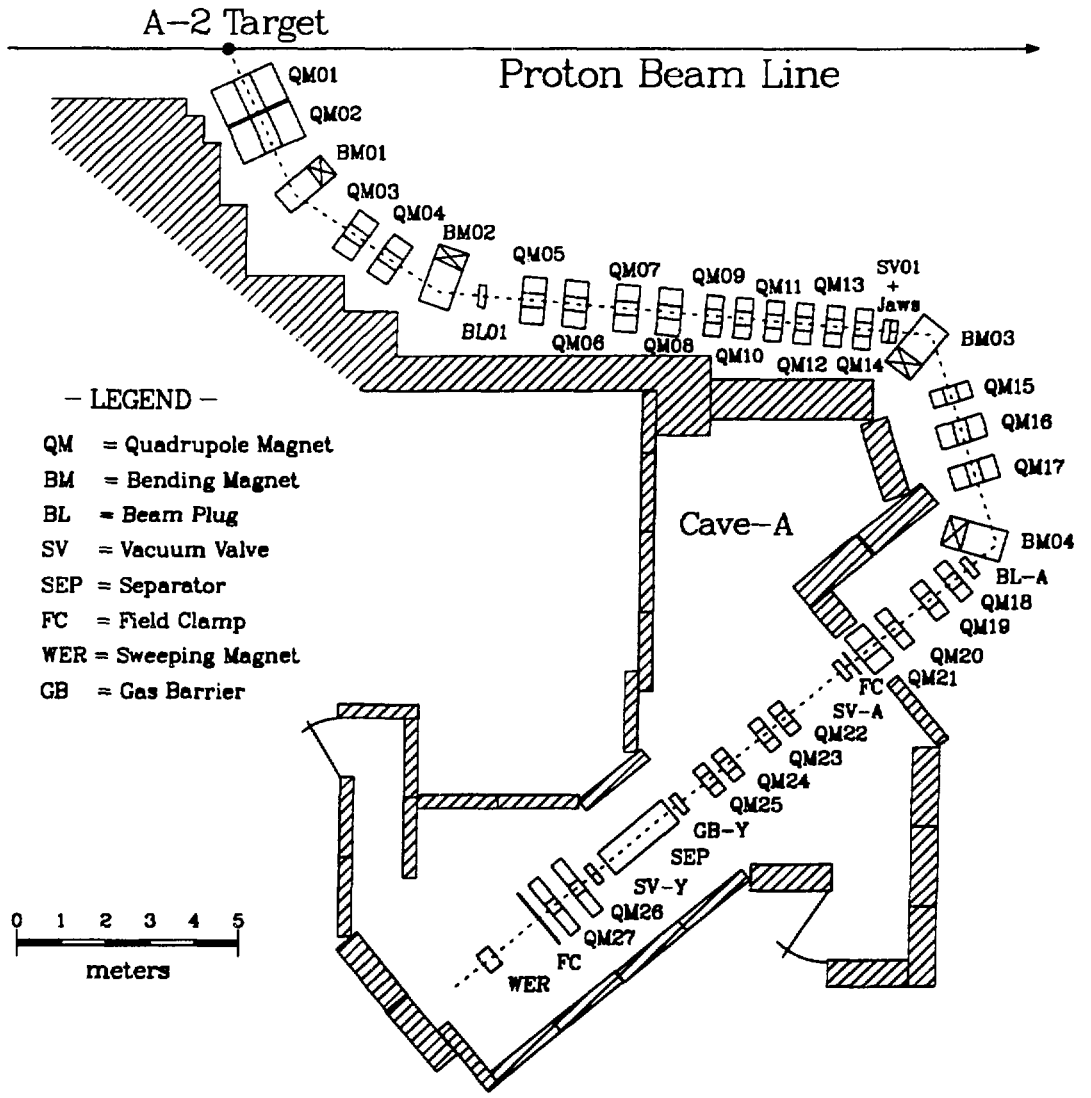

Figure 3.1: Stopped Muon Channel

pressure multi-wire proportional chamber (MWPC), 5 cm further downstream. For a more complete description of the MWPC see Section 4.1.1. The collimator is a 3.75-cm thick lead disk with an outer radius of 29 cm and an inner radius of 5 cm. The MWPC is used for tuning the μ^+ beam and as a normalization for the muonium formation experiment, as well as for the static quench and microwave measurements. The vacuum is maintained at 5×10^{-6} Torr by two turbo molecular pumps on the experimental apparatus and a cryogenic pump attached to the separator.

3.1.1 "Sub-surface" μ^+ Beam

Large numbers of pions are produced by strong interactions between the proton beam and the A-2 target. The SMC was originally designed to collect these pions, allow them to decay to muons and then momentum select the muons [Tho79]. A larger stopping density of positive muons is obtained by collecting muons from π^+ decaying at the surface of the target — a "surface" muon beam [Pif76,Rei78], rather than collecting those pions that escape out to the channel and then decay. The muons from the π^+ decaying at rest at the target surface have an energy of 4 MeV and a momentum of 30 MeV/c, determined from the kinematics of the pion decay, $\pi^+ \rightarrow \mu^+ + \nu_\mu$ and the pion and muon masses, $m_\pi = 140$ MeV, $m_\mu = 106$ MeV. Due to parity violation in the weak decay this muon beam is nearly 100% polarized with the muon spin anti-parallel to the momentum. The largest rate of muons as a function of momentum actually occurs at the slightly lower momentum of 28 MeV/c due to the larger numbers of pions produced just inside of the target surface.

An even higher fractional stopping density of low-energy muons is obtained by tuning the SMC to lower momenta and selecting muons from pions decaying further inside the target — a "sub-surface" muon beam [Bad85]. The fractional stopping density is defined as the number of muons stopping per unit of material(g/cm^2) per incident muon. From the muon range-momentum relation in this momentum region [Tro66]

$$R = a \cdot p^{3.5} \tag{3.1}$$

where R is the muon range and a is a constant depending on the production target material, one can calculate the expected muon rate as a function of momentum [Pif76]

$$r = ap^{3.5}e^{-m_\mu \ell/p\tau_\mu} \tag{3.2}$$

where r is the muon rate, p is the muon momentum, and the exponential factor is added to include losses due to muon decay in the channel: ℓ is the length of the channel, 38 m, and $m_\mu(\tau_\mu)$ is the muon mass (lifetime). Experimental measurements at the SMC support the momentum dependence of Equation 3.2 [Bad85]. The spread in the range arises from the momentum spread in the beam and from range straggling. If the straggling is taken as 10% of the range [Ste60], the range spread can be expressed as:

$$\Delta R = a \cdot p^{3.5}\sqrt{\left[0.10^2 + \left(3.5\frac{\Delta p}{p}\right)^2\right]} \tag{3.3}$$

The range spread is smaller at lower momentum.

For the low-momentum sub-surface beam the amount of material in the beam line is very small; a total of 1.05 mg/cm^2 for this sub-surface μ^+ beam. The range of a 7 MeV/c muon in carbon is 1.0 mg/cm^2 and is 1.5 mg/cm^2 for a 8 MeV/c μ^+. To optimize muonium production (see Section 3.2), the density of very slow muons emerging from the muonium production foil should be maximized This is accomplished by centering the stopping distribution at the downstream edge of the foil (i.e. the mean range should be 1.05 mg/cm^2). The absolute momentum of the μ^+ can be inferred from the fields in the bending magnets in the channel. The bending magnet settings correspond to a momentum of 7.3 MeV/c during the Lamb shift experiment. Another source of data for determining the momentum is the value of the fields in the separator(see Section 3.1.3), from which the momentum is determined to be 7.9 MeV/c. The emerging μ^+ energy, in conjunction with dE/dx calculations for the material in the beam, can also be used to deduce a value for the incident beam momentum of 7.6 MeV/c. The absolute channel momentum is important for considerations on the muon rate and the efficiency of muonium production, but will not effect the value of the RF measurement.

The channel magnets are set according to previous TRANSPORT [Bro77] calculations for the beam line [Kua88]. The magnets and the separator **E** field are then tuned for maximum rate at each momentum, where the bending magnet BM03 is not varied and fixes the momentum. The momentum determinations from each of the four bending magnet fields agree to within 3%.

One source of background for this experiment results from positrons in the beam, due to two sources:

- Pair production by gammas from π° decay in the target.
- Decays of μ^+ upstream, in the channel or the target.

These beam positrons are a source of background for both the Ly_α and MCP detectors. The other major source of background is from radioactive gas diffusing down the channel. All three detectors are sensitive to the radioactive gas.

3.1.2 Radioactive Gas

An important source of background is radioactive gas produced at the target when the primary current exceeds 250 μA (the target reaches 400 K at a proton current of 650 μA). The radioactive gas consists of spallation products that diffuse out of the target and then proceed down the beam line [Don83]. The gas consists mainly of two components: ^{6}He(τ = 1.165 s) with a 3.5 MeV β^- endpoint and ^{12}N (τ = 0.025 s) with a 16.3 MeV β^+ endpoint. A 1.5 μm Mylar gas barrier is inserted to minimize the radioactive gas in the experimental region. With the gas barrier removed, the count rates in the MCP and Ly_α detectors increase by two orders of magnitude. The gas barrier must be thin in order to reduce losses in muon beam intensity due to multiple scattering. The gas barrier serves as a direct barrier, stopping some of the radioactive gas; however, the ^{6}He can diffuse through. The gas barrier reduces the ^{6}He by separating the good vacuum in the downstream experimental apparatus from the rather poorer vacuum in the SMC upstream. With the worse SMC vacuum ($\sim 10^{-3}$ Torr) scattering of the gas with the residual air molecules effectively slows down the gas molecules, which then decay before reaching the experimental apparatus.

3.1.3 E ⊥ B Separator

Positrons are separated out of the beam through the use of an **E⊥B** separator. Electric and magnetic fields are applied perpendicular to each other and to the beam direction. This configuration serves as a velocity filter and, in combination with the channel magnets which select for momentum, a mass filter, passing muons and bending positrons out of the beam. The electric field is tuned such that the Lorentz force on a μ^+ is zero, i.e.

$$\mathrm{E(V/cm)} = 300 \cdot \beta_{\mu^+} \cdot \mathrm{B(Gauss)} \tag{3.4}$$

Two different types of separators are available at LAMPF: one is five feet long with **E** and **B** field regions of approximately equal length; the other is four feet long with the **E** field region significantly longer than the **B** field region. The shorter separator was used during initial studies and during the static quench portion of the experiment; the longer separator was used during the microwave portion of the experiment.

The electrodes on the short separator are 100 cm long and 15 cm wide, with a gap between the plates of 10 cm. The effective magnetic field length is however only 38 cm. Therefore Equation 3.4 has to be modified; the **B** field must be increased to compensate for the shorter length. The background rate in both the Ly_α tubes and the MCP is very sensitive to the positron rate. In order to achieve adequate muon beam purity it is necessary to operate this separator at fairly high fields. At these fields the transmission of muons drops to ~60% due to the unequal field lengths. The optimum setting was determined to occur at a magnetic field of 550 G (at 500 A) and an electric field of 3.9 kV/cm.

The electrodes on the long separator are 152 cm long and 20 cm wide, with a gap of 10 cm. The effective magnetic field length is 146 cm. The optimum settings are at a magnetic field of 375 G (440 A), and an electric field of 8.1 kV/cm. With use of this separator there is no significant loss of muons as the fields are increased.

3.2 Muonium Production

Muonium is produced by the beam foil technique [Bol82]. A μ^+ beam is passed through a thin (200 $\mu g/cm^2$) Al foil where some of these muons capture an electron to form muonium (an additional, smaller fraction will capture two electrons and form M^- ions [Kua87,Kua89]). The neutral M fraction is highly dependent on the incident μ^+ momentum: 0.06% at 28 MeV/c [Bol81], 4% at 9.75 MeV/c [Bad84b] and 12% at 7.3 MeV/c (see below). Only those μ^+ with velocities comparable to the Fermi velocity, will have an appreciable probability of capturing an electron. (The Fermi velocity v_F, for most metals, is approximately equal to the Bohr velocity $v_B = \alpha c$.) Therefore, to optimize the muonium formation the muon channel should be tuned to maximize the number of muons with velocity αc at the downstream surface of the Al foil. This corresponds to a muon energy of $\sim$ 5 keV. Based on data from beam foil experiments with protons, appreciable neutralization is expected only for muons with less than 10 keV [Phi55] (see Figure 3.2). For muonium formation experiments at different momenta the amount of material in the beam is varied such that approximately half of the incident beam is stopped in the degrader/production foil. With the centroid of the stopping distribution at the downstream edge of the production foil the number of low-energy μ^+, with a high probability of forming muonium, is maximized. If the momentum of the μ^+ is too low most will stop in the production foil and will not form muonium in the vacuum. If the momentum of the μ^+ is too high they will leave the MWPC with velocities that are too large for an appreciable fraction to form muonium. The muonium rate should be independent of the incident muon momentum for surface or sub-surface beams if the momentum is optimized for the amount of material in the beam. At lower incident beam momentum the degrading material has simply been shifted from the experimental area to the pion production target. The decrease in muon rate ($p^{3.5}$) is compensated by the decrease in the range spread ($p^{3.5}$), giving the same number of muons in a given energy range downstream of the production foil(i.e. 5 keV) independent of momentum. While the muonium rate should remain unchanged, the muon rate falls with the $p^{3.5}$ law (Equation 3.2). Therefore at lower momentum the muonium rate,

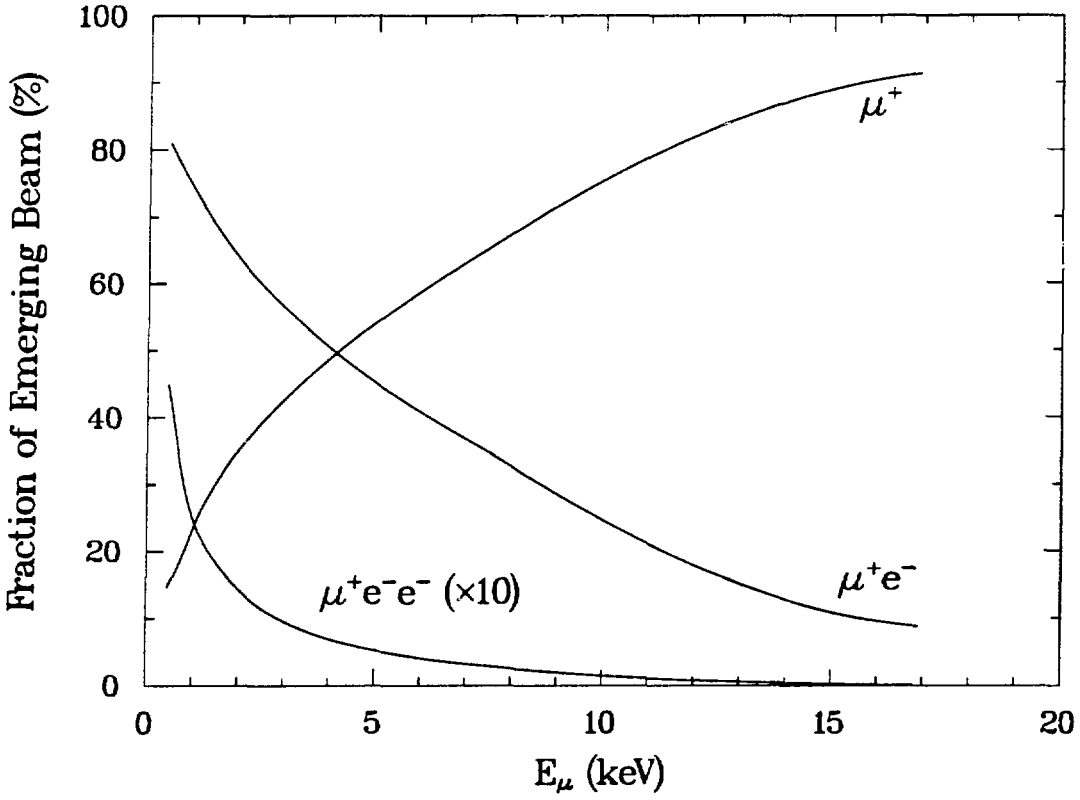

Figure 3.2: Charge State Fractions

and therefore the signal rate, remains the same but the background rate in all three detectors from μ^+ is reduced.

The apparatus for measuring the muonium formation rate is shown in Figure 3.3. The μ^+ are degraded and counted in the MWPC; then the beam passes through a sweeping magnet and is stopped on a teflon beam stop. The sweeping magnet is "H" shaped, with a 15 cm gap and 20 cm × 30 cm pole tips. When the magnet is off both μ^+ and muonium are transmitted to the beam stop and when the magnet is on (2.7 kGauss at 900A) only the neutral muonium atoms are transmitted. The radius of curvature for the μ^+ is given by

$$\mathrm{R(cm)} = \frac{|\mathbf{p}|\,(\mathrm{MeV/c})}{0.3 \cdot \mathrm{B(kGauss)}} \leq 10 \text{ cm (for } |\mathrm{p}| \leq 8\mathrm{MeV/c}) \qquad (3.5)$$

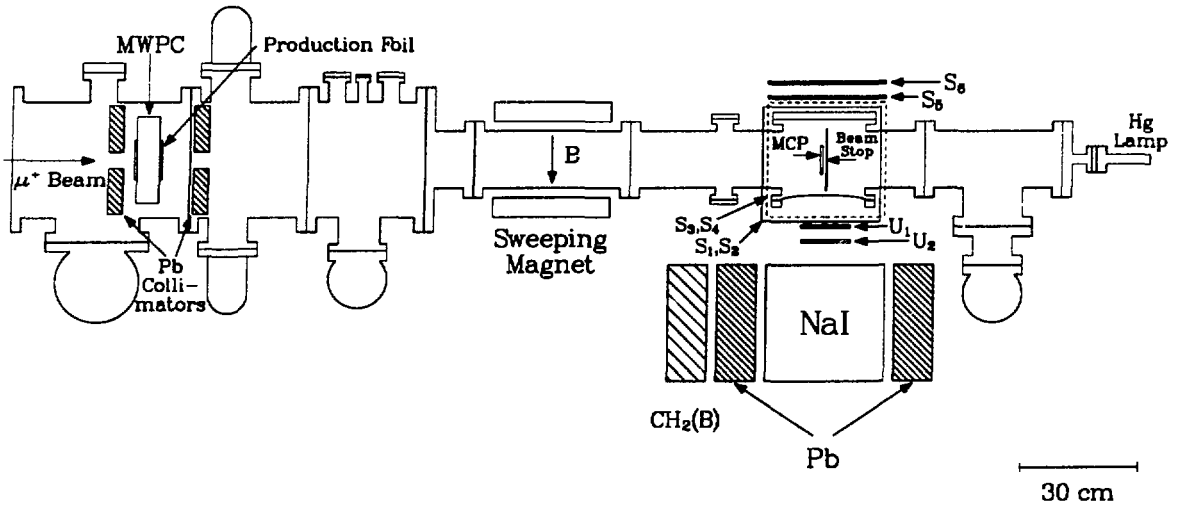

Figure 3.3: Muonium Formation Apparatus

The distance from the sweeping magnet to the beam stop is 70 cm, so with the magnet on only the neutral muonium atoms reach the beam stop. The μ^+ and muonium are detected by measuring the energy deposited in a NaI(Tl) crystal by e^+ from the μ^+ decay ($\mu^+ \rightarrow e^+ + \nu_e + \overline{\nu_\mu}$). A thin 125 μm Al window separates the evacuated beam line from the NaI detector. The NaI crystal is a right circular cylinder measuring 25 cm in diameter and 25 cm deep. Shielding for the crystal consists of 10 cm of borated polyethylene bricks (5% Boron) to thermalize and capture slow neutrons and 10 cm of Pb for shielding against gamma rays and charged particles. The crystal is mounted vertically under the beam line and is viewed by seven 7.5-cm diameter phototubes mounted under the crystal. The HV distribution of each tube base is adjusted with a ^{60}Co source to obtain equal pulse heights out of each tube. A schematic diagram of the tube bases is shown in Figure 3.4. The signal from the NaI is amplified by a Tennelec 203BLR linear amplifier with a time constant of 0.25 μs. The pulse height is measured with a LRS2259A peak-sensing ADC in the CAMAC crate.

The signature for an event in the NaI is a coincidence of the scintillator telescope ($U_1 \cdot U_2$) in anti-coincidence with the cosmic ray veto scintillator S_6, ($U_1 \cdot U_2 \cdot \overline{S_6}$).

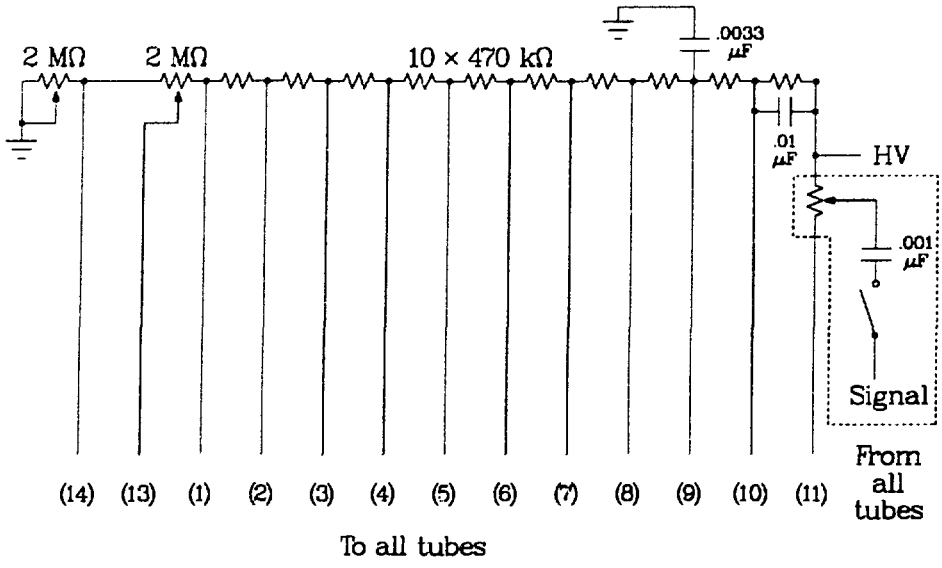

Figure 3.4: Diagram of the NaI Tube Bases.

A diagram of the trigger and ADC gating logic is shown in Section 4.3.2. The incident muon momentum is varied from 6.5 – 8.5 MeV/c by varying the currents in the channel magnets. The channel is then set to the momentum corresponding to the largest ratio of muonium production to incident μ^+. Muonium formation measurements were made during three different beam running times between 1986–1987. The fractional solid angle subtended at the center of the beam stop by the scintillator telescope varied from 2.7% to 3.7% during these runs. All measurements were made with the same crystal, although not always with the same ADC or data acquisition system. When the sweeping magnet is turned off, large numbers of decay positrons are observed in the NaI detector from the decay of the abundant μ^+. Data are collected under this configuration, primarily for determining the characteristics of the NaI crystal, such as its energy resolution, and for determining the energy calibration of the ADC.

Pulse height spectra of the NaI are shown in Figure 3.5 a) with the sweeping magnet off, b) with the sweeping magnet on, and c) with both the separator and sweeping magnet off. With the magnet off we see a Michel spectrum [Mic50] (ch ~

300–1400) from μ^+ decay. The cut off at channel 100 is from a discriminator and the peak in channel 2000 is from overflow events in the ADC. The counts below channel 250 are enhanced when the separator is off and positrons are not deflected out of the beam (see Figure 3.5c); these counts are presumably from scattered beam positrons. In Figure 3.5b, with the magnet on, the μ^+ are deflected out of the beam. The Michel spectrum can still be seen, although there is an enhancement of the background below channel 250 and of the counts above channel 1400 which are presumably cosmic-ray related and enhanced due to the lower trigger rate with muonium and no muons.

The energy and angular distribution of positrons from μ^+ decay can be described by the differential decay probability [Com83]:

$$\frac{d^2\Gamma}{dyd(\cos\theta)} = \frac{G_F^2 m_\mu^5}{192 \cdot \pi^3} 2y^2 \{(3-2y) + (2y-1)\cos\theta\} \tag{3.6}$$

The positron mass, which is small compared to the muon mass ($m_{e^+}/m_{\mu^+}=1/206.8$) has been neglected and the radiative corrections have not been included. The Fermi coupling constant is $G_F = 1.16637(2) \times 10^{-5} GeV^{-2}$ [Agu88] in units where $\hbar = c = 1$. The variable y is the positron energy normalized to its maximum value of 52.83 MeV. The energy corresponding to a given channel in the ADC spectrum is given by

$$E = E_o + f \cdot ch \tag{3.7}$$

where E_o, the energy corresponding to channel 0, and f, in units of MeV/channel, are parameters to be determined from the fits to μ^+ decays. For the detector geometry, with the observing direction 90° to the direction of the initial muon polarization, the Michel function is given by

$$N(y, \pi/2) = N_o(6-4y)y^2 \tag{3.8}$$

In addition, the characteristics of the detector itself must also be considered; in particular, the resolution and finite size must taken into account. The NaI detector is essentially the same one used for the experiments in which muonium in vacuum was first discovered and is described in more detail elsewhere [Bol82]. The resolution

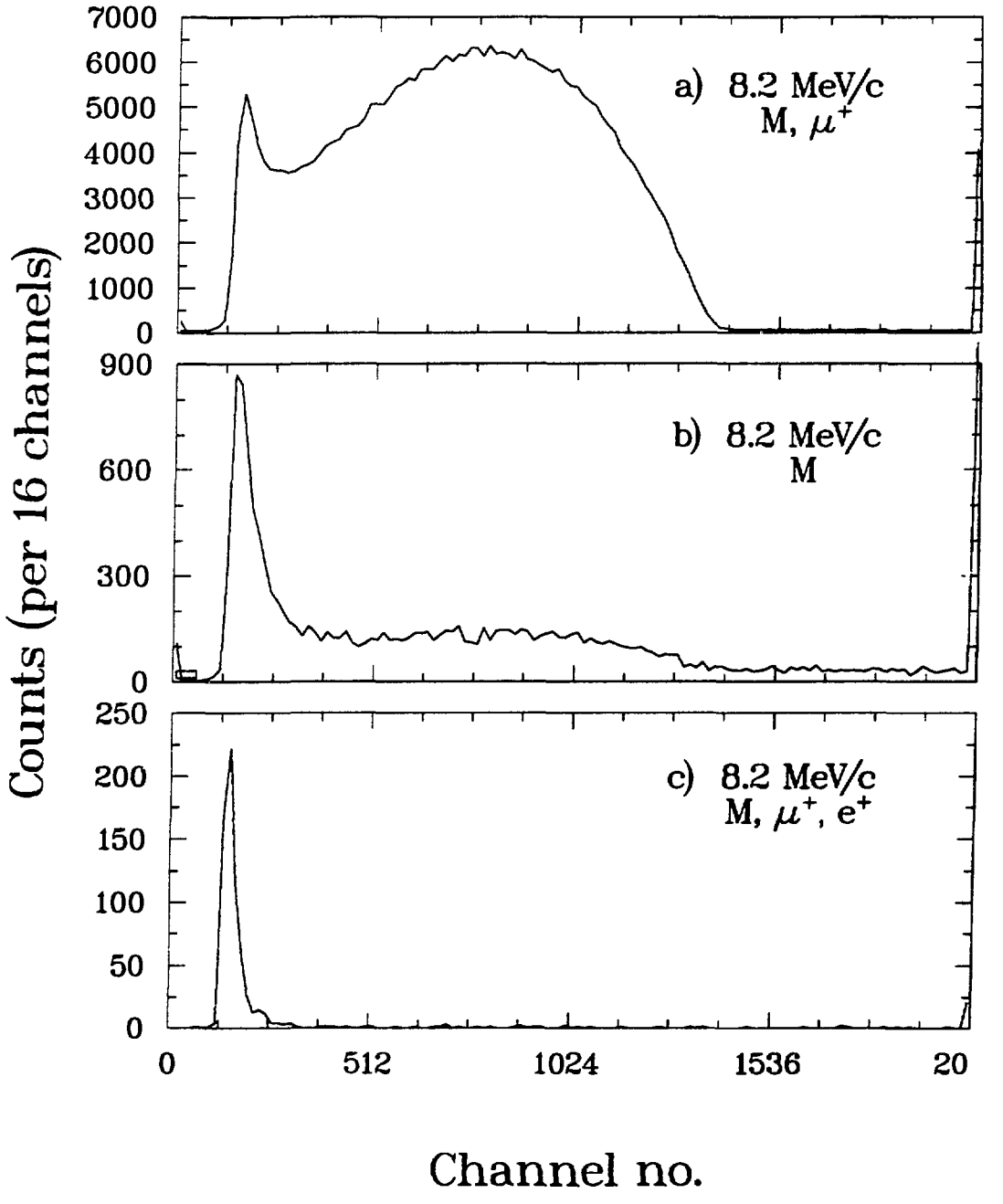

Figure 3.5: NaI Histograms — a) Sweeping Magnet Off, b) Sweeping Magnet On, and c) Separator Off

function is

$$R(z) = \sqrt{\frac{1}{2\pi\sigma}} \int_0^1 e^{-(y-z)^2/2\sigma^2} dy \tag{3.9}$$

where the number of counts $R(z)$ at the observed energy z contains contributions from all Michel energies. The assumption that the resolution σ is independent of energy over the Michel spectrum is approximately correct. If the resolution is proportional to $E^{-1/4}$ [Hug72], then from 10–50 MeV the variation in σ is only 30%. The empirical sensitivity function describing the loss of energy out of the crystal for higher-energy positrons is given by:

$$S(y) = 1 - sy \tag{3.10}$$

s is a fitting parameter. The expression for the number of positrons in each energy bin is then

$$N(z) = N_0 \sqrt{\frac{1}{2\pi\sigma}} \int_0^1 (6 - 4y) y^2 (1 - sy) e^{-(y-z)^2/2\sigma^2} dy + B \tag{3.11}$$

The background is flat above channel 1400 so a constant background term B has been added. This expression can be analytically integrated, using tabulated values of the error function.

$$\begin{aligned} N(z) \;=\; & N_0 \sqrt{\frac{1}{2\pi\sigma}} \{ F_{ab} \cdot (A_o + A_2 + 3A_4) \\ & + e_a \cdot \left[A_1 + aA_2 + (a^2+2)A_3 + (a^3+3a)A_4 \right] \\ & - e_b \cdot \left[B_1 + bB_2 + (b^2+2)B_3 + (b^3+3b)B_4 \right] \} + B \end{aligned} \tag{3.12}$$

where

$$\begin{aligned} A_o &= z^2 \left[4sz^2 - (4+6s)z + 6 \right] \\ A_1 &= \sigma z \left[16sz^2 - (12+18s)z + 12 \right] \\ A_2 &= \sigma^2 \left[24sz^2 - (12+18s)z + 6 \right] \\ A_3 &= \sigma^3 \left[16sz - 6s - 4 \right] \\ A_4 &= \sigma^4 \left[4s \right] \\ a &= -z/\sigma \end{aligned}$$

$$
\begin{aligned}
b &= \frac{1-z}{\sigma} \\
e_a &= e^{-a^2/2} \\
e_b &= e^{-b^2/2} \\
F_{ab} &= \sqrt{\pi/2}\left[erf(b/\sqrt{2}) - erf(a/\sqrt{2})\right] \\
erf(b/\sqrt{2}) &= \sqrt{2/\pi}\int_0^b e^{-x^2/2}dx
\end{aligned}
\tag{3.13}
$$

The fitting parameters for each data taking period are determined from μ^+ runs taken immediately before or after the muonium runs. The fitting parameters, as determined from μ^+ runs in July and September 1987 (see Figure 3.6) are

$$
\begin{aligned}
\mathrm{E_o} &= 0.5(3)\mathrm{MeV} \\
\mathrm{f} &= 0.0398(2)\mathrm{MeV/channel} \\
s &= 0.940(5) \\
\sigma &= 0.031(1)
\end{aligned}
\tag{3.14}
$$

which are dependent only on the detector system, and:

$$
\begin{aligned}
\mathrm{N_o} &= 1.394(1) \times 10^4 \\
B &= 62.7(1.5)
\end{aligned}
\tag{3.15}
$$

which are also dependent on beam conditions and running time. A fit to the 7.3 MeV/c muonium data from July 1987 is seen in Figure 3.7 where the χ^2 is 87 for 69 degrees of freedom. The values for the parameters $\mathrm{N_o}$ and B are

$$
\begin{aligned}
\mathrm{N_o} &= 236(5) \\
B &= 42(1)
\end{aligned}
\tag{3.16}
$$

In both the μ^+ and muonium data the channels fit are from 600–2000 (24.4–80.1 MeV). The channels below 24 MeV were not fit due to the large background at low energies. In the muonium fit the only parameters allowed to vary are $\mathrm{N_o}$ and B; the others are fixed from the μ^+ runs. Fits to the NaI spectra are made for muonium runs at several momenta; these counts are then normalized to the MWPC

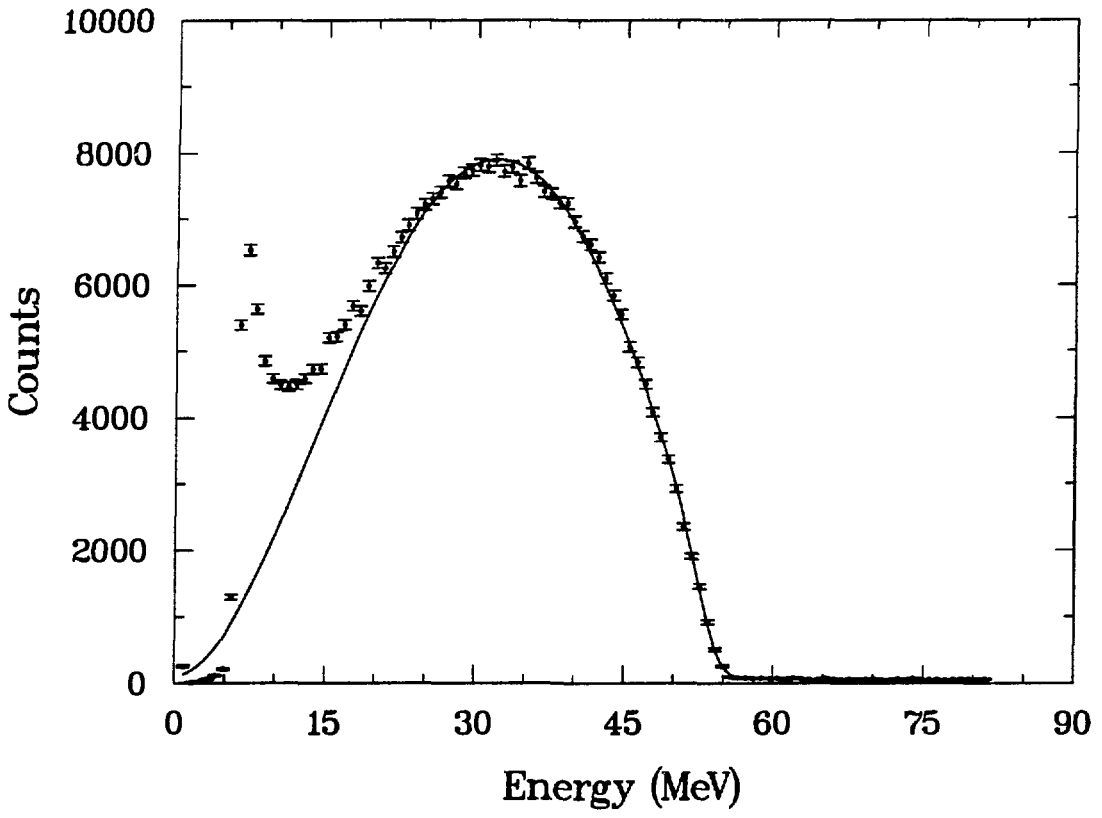

Figure 3.6: Fit to the Michel spectrum of decay positrons, with the sweeping magnet off

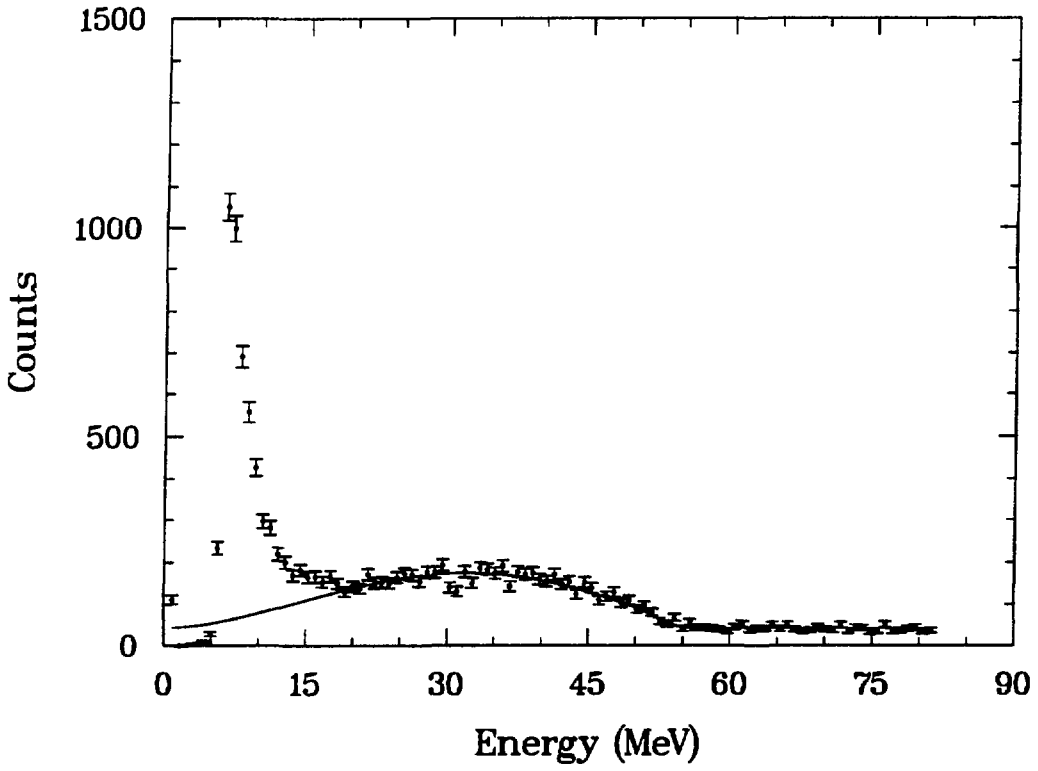

Figure 3.7: Fit to the Michel spectrum of decay positrons, with the sweeping magnet on

counts and scaled for the detector solid angles. A plot of the formation fraction vs. incident momentum is shown in Figure 3.8. The values of the muon momentum are determined from the currents in the channel bending magnets.[1] The error bars include the statistical counting error as well as the errors in the measurement of the solid angles. In order to compare with previously published formation fractions [Bad84b,Bol81], the muonium production is assumed to be isotropic. Monte Carlo calculations [Kua89] and recent experiments [Ahn89] indicate that the actual distribution is peaked in the forward direction, so the actual formation fraction at the production foil is somewhat lower. This estimate of the muonium rate at the production foil does not influence the determination of the resonance frequency.

3.3 Muonium 2S Production

Beam-foil experiments with protons indicate that $\sim$ 10% of the neutral atoms emerge in the 2S state [Gab81]. An experiment to measure the amount of muonium in the 2S state uses the same detectors and electronics as the microwave experiment (see Chapter 4) with a simpler system and a larger signal rate than is available with the microwave apparatus.

The application of an electric field mixes the metastable 2S state with the 2P state, with subsequent decay to the 1S ground state. The difference in the observed count rate for electric field on and electric field off conditions then gives a measure of the M(2S) formation rate.

For determining the M(2S) yield, a set of three wire planes is installed perpendicular to the beam direction centered between the Ly_α tubes (see Figure 3.9). The grids consist of 50 μm gold-plated tungsten wires spaced at 2 mm intervals; the grid planes are spaced 2 cm from each other. The outer two grids are grounded and the center grid is switched from -1200 V to ground at a rate of $\sim$ 1 Hz. The switching is done between beam gates; the switching circuit time $\sim 100\mu$s is small

[1]The calibration from magnet shunt reading, in mV, to channel momentum, in MeV/c, is given by: p_μ=4.0×BM01, p_μ=6.2×BM02 and p_μ=2.8×BM03(4). The shunt readings for the 7.3 MeV/c point were 1.86 mV, 1.17 mV, 2.67 mV, and 2.61 mV, respectively.

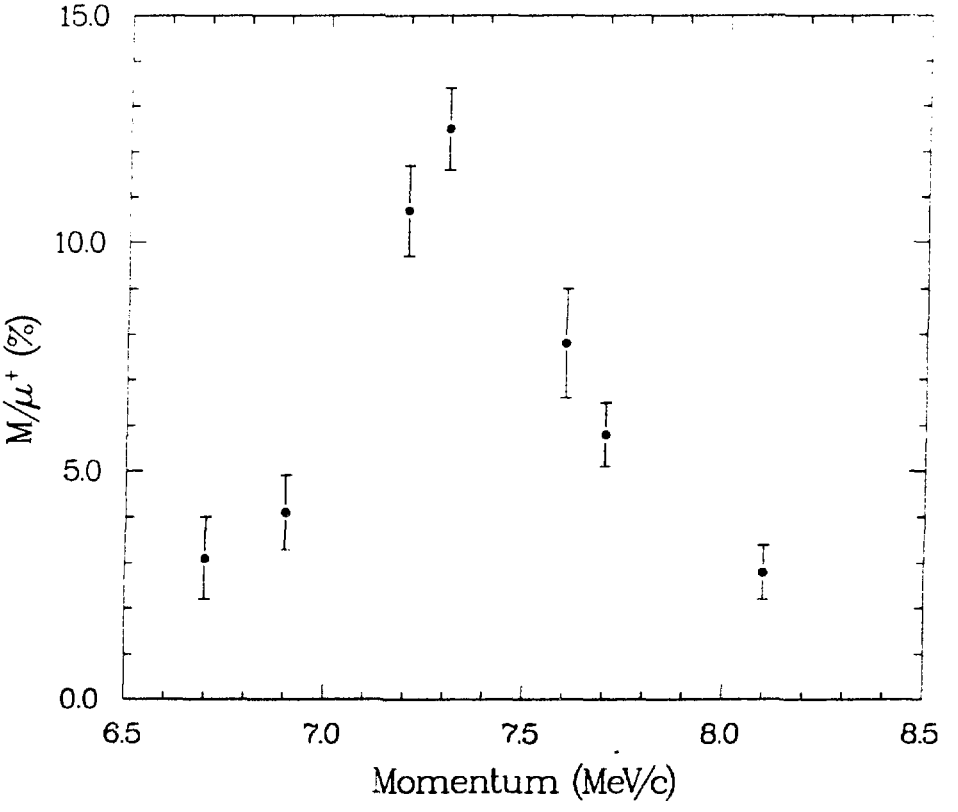

Figure 3.8: Muonium Formation Fraction

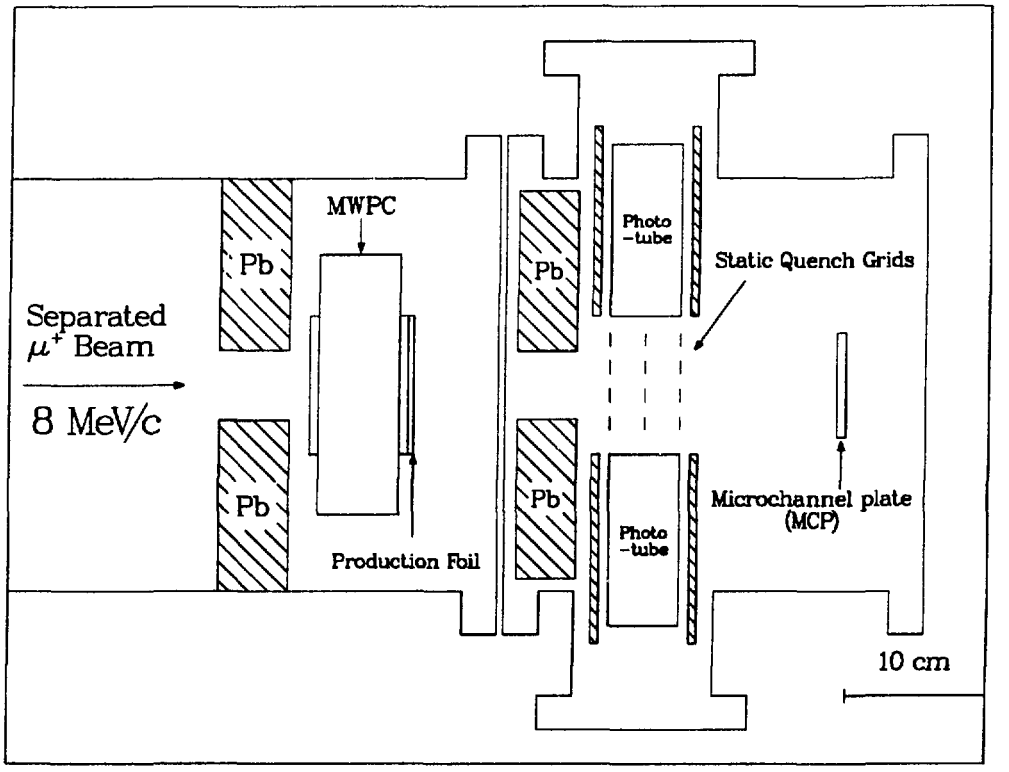

Figure 3.9: Static Quenching Beamline

compared to the time between beam gates(8 ms). The grid on phase, Grid_{ON}, provides a uniform field of 600 V/cm, and leaves any charged particle component of the beam unchanged in energy. Since the signature for M(2S) is a difference in the number of counts with the field on and with the field off it is important to insure that there are no systematic effects from the application of the field. A longitudinal field is chosen as it does not deflect charged particles. The outer grids are grounded in order to minimize any focussing effects on the charged components of the beam from the stray fields. A positive HV on the center grid would stop low energy charged particles (less than 1.2 keV), so a negative potential is applied. The choice of -1200 V on the center grid plane is made to minimize any of these effects which could have mimicked or masked the signal from 2S muonium by changing the background count rates during the Grid_{OFF} and the Grid_{ON} phases. The quenching probability can be determined from Equation 2.36, where the detuning Ω is replaced by the Lamb shift splitting ω_{LS} and the matrix elements b are given in Table 2.5. The quenching probabilities for each of the $2^2S_{1/2}$ sublevels are averaged according to their population distributions. At fields of 600 V/cm, $\sim$90% of the 2S atoms are quenched for the observed velocity distribution(see Chapter 5). The quenching probability as a function of electric field is shown in Figure 3.10.

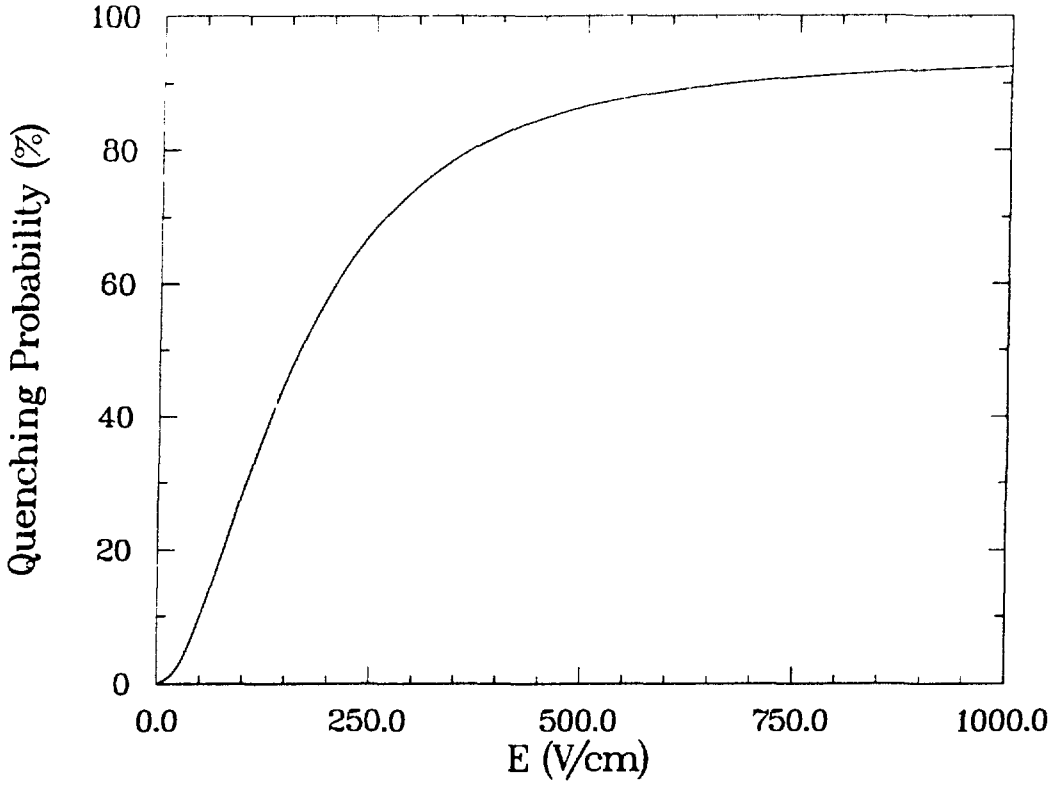

Figure 3.10: Quenching probability of 2S muonium as a function of electric field for an average muonium energy of 10 keV

Chapter 4

Apparatus and Procedure

The essential components of this experiment consist of: a system of detectors to identify a quenched muonium (2S) atom, the microwave system that drives the transition from the 2S to the 2P state, the electronics for processing the various detector signals and defining a trigger, and the data acquisition system for recording this data on tape and for providing information on the performance of the components of the experimental apparatus while data taking is in progress. Figure 4.1 shows the arrangement of the detectors and microwave cavity for the experiment.

4.1 Detectors

A signal from the muon counter in coincidence with signals from the Lyman alpha detector and the microchannel plate detector is an indication of a transition from the 2S state to the 2P state, with the subsequent emission of a Ly_α photon. The three detector systems consist of:

- A low pressure MWPC, for detection of the incident muon.
- A set of four UV sensitive phototubes, for detection of the Lyman alpha photon.
- A MCP detector, for detecting the muonium atom downstream.

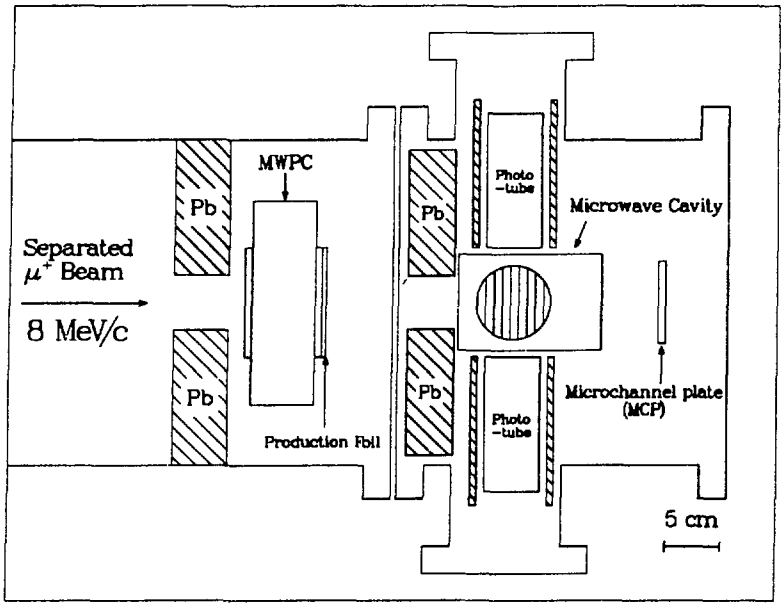

Figure 4.1: Lamb Shift Apparatus

4.1.1 Muon Counter

The muon (μ^+) counter used in this experiment is a low pressure multi-wire proportional chamber (MWPC) [Sau77,Bre77]. This counter serves three purposes: as a degrader to slow down the incident muons, as a beam counter to monitor the incident μ^+ rate, and as one part of the three-fold coincidence defining a 2S $\longrightarrow$ 2P transition.

Figure 4.2 is a diagram of the MWPC. The MWPC has 7.6-cm diameter entrance and exit windows covered with 1.5-μm Mylar windows. The body of the chamber is 23 cm in diameter and 6.0 cm thick; the inner volume is $\sim$ 1.0 liter. The chamber has been operated in a variety of wire plane configurations and at a variety of pressures. The configuration used for data taking is with five wire planes: the anode consists of 20-μm wires spaced 2 mm apart, the set of intermediate planes are also 20-μm wires at 2 mm, and the outside set of cathode planes are 50-μm wires at 2-mm spacing. The transmission through all five planes is 92%. At the operating condition of 10 Torr isobutane, the typical voltages applied are +810 V on the anode and −450

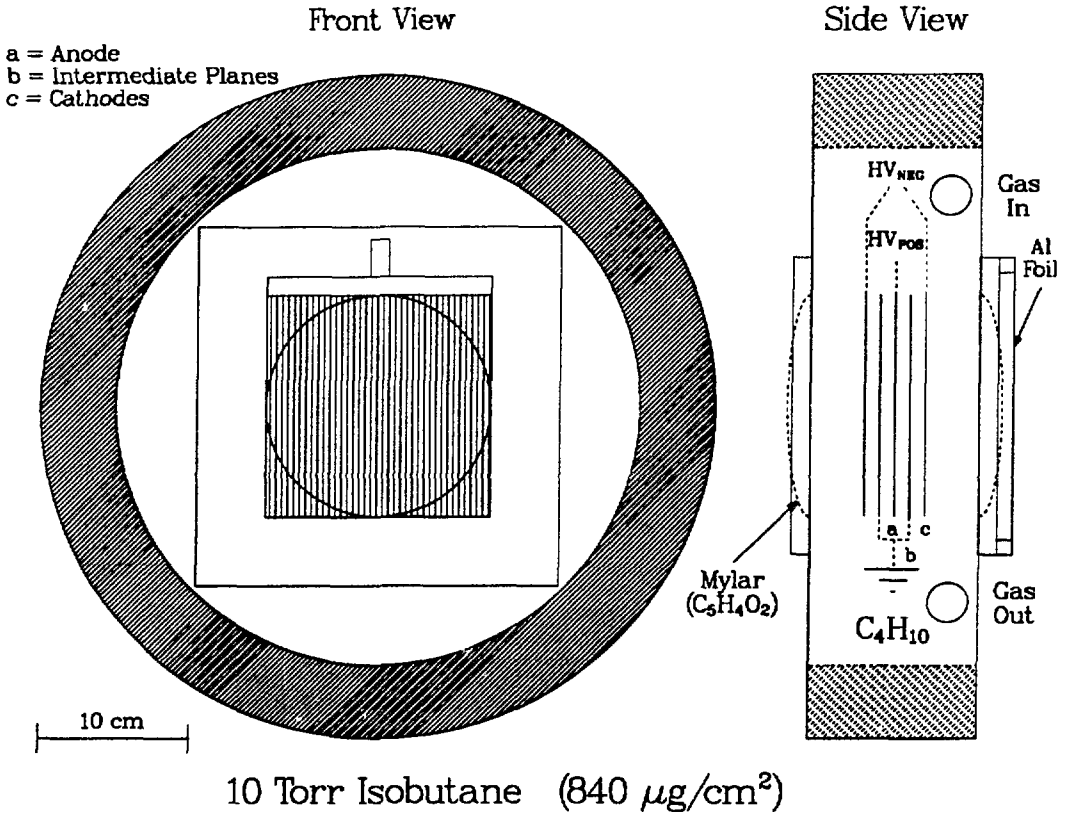

Figure 4.2: Diagram of the low pressure multi-wire proportional chamber

V on the outer cathode or at +750 V and −490 V, respectively. The intermediate planes are held at ground.

The typical operating pressure is 10 Torr of isobutane. The density of isobutane is 2.47 g/l (20°C), corresponding to 32.5 mg/l at 10 Torr. This gives 210 μg/cm^2 for the 6.5 cm thickness of isobutane. Each window (1.5 μm Mylar) has a thickness of 210 μg/cm^2 and the production foil thickness (0.77 μm Al) is 210 μg/cm^2. The total thickness for the operating configuration is 840 μg/cm^2.

The previous measurement of the Lamb shift at the LAMPF was done using a 20 μm plastic scintillator. The optimum momentum for M formation was found to be $p_\mu = 9.75$ MeV/c, and the M formation fraction was 4%. Attempts to use a thinner scintillator were unsuccessful because light collection falls off rapidly with decreasing thickness and pulse-height discrimination between beam μ^+ and e^+ becomes very difficult [Woo85]. Therefore, a program to develop a low pressure MWPC was instituted. Several versions of the MWPC have been used with varying degrees of success and with different total thicknesses. The first, and simplest, configuration consisted of three wire planes, the two outer cathode planes held at ground and the center anode plane at +HV. This configuration was found to be unacceptably unstable and inefficient. After several unsuccessful attempts to plateau the chamber in the muon beam, a new configuration was tested. The second arrangement consisted of two Al-Mylar cathode foils at ground potential and an anode wire plane at +HV. This permitted significantly more stable operation. With the use of solid foil cathodes no field leaked out between the wires to attract electrons liberated outside of the active region and the long $\sim$ 300 ns tail seen with the earlier configuration was eliminated. Two disadvantages to this second setup are that sparks between anode and cathode can burn holes in the thin cathodes (cathode thickness = 1.5 μm or 210 μg/cm^2 of which $\sim$ 10 μg/cm^2 are Al) and that the chamber thickness becomes much larger, 1.0 mg/cm^2 instead of 600 μg/cm^2. The third and final arrangement uses a separate pre-amplification region [Bre84]. Five wire planes are used, with the center anode plane at +HV, the two intermediate planes at ground, and the two outer cathode planes at −HV. This provides a reasonably stable mode of operation. A direct measurement of the chamber's efficiency for detecting sub-surface muons

has not been made; nevertheless, one can compare the rates of μ^+ detected using the MWPC at 7.5 MeV/c to those rates at 9.75 MeV/c using a similar beam line and a 20 μm scintillator. Scaling by $p^{3.5}$ from 9.75 MeV/c to 7.3 MeV/c and taking into account the transmission through the wire planes and the muon lifetime, one would expect the rate to be $\sim$ 45–65 kHz whereas we observe 40–45 kHz.

The two-stage MWPC, with five wire planes, makes use of the fact that at low pressures P, the reduced electric field $|\mathbf{E}|/P$ can reach large values without a particularly large field. At low pressure the collisional mean free path for electrons is large and the electrons can gain substantial energy so that the probability of ionizing collisions becomes much larger. Therefore in regions of lower electric field far from the anode wires the electrons will start to avalanche.

A trade-off between stability and rise time must be made. At relatively low beam rates, very high and symmetric potentials can be applied, giving reasonably fast rise times. At higher rates (i.e. full μ^+ beam) this leads to less stability. Empirical observations indicate that a lower potential on the outer planes provides a more stable operation, particularly at higher rates, but does lead to a deterioration in pulse rise time. For the case with HV= $+800, -450$ the rise time is $\sim$ 40 ns; for HV = $+750, -490$ the rise time is $\sim$ 25 ns. The 6–9% duty factor at LAMPF means that the instantaneous rates incident on the chamber are 10–20 times larger than the average rates. Operation with the foil cathodes gives a FWHM for 9 MeV/c muons of 25 ns whereas the two-stage operation results in a FWHM of 25–40 ns, depending on HV configuration. The MWPC has an added advantage relative to a thin scintillator in that it has a much lower background rate. For the minimum ionizing beam positrons, the active region of the chamber is less than 10% the thickness of a 20 μm scintillator. The pulse heights from positrons are such that even with a very low discriminator threshold very few are seen. However, the positrons may be contributing to the lack of stability in the MWPC operation. A possible explanation for the instabilities may be the fairly high current from large numbers of low pulse height signals from beam positrons. When the separator **B** field is turned down to bring positrons through the apparatus, the MWPC count rate drops, as the μ^+ are bent out of the beam. The current in the chamber increases

substantially, presumably due to the many low pulse-height positrons. The chamber can not operate with the full rate of beam positrons, even though the counting rate with a low discriminator threshold is not very high.

4.1.2 Lyman Alpha Detectors

Four Hamamatsu R2050 phototubes are used for detection of the 1221Å Lyman Alpha photons from the 2P $\longrightarrow$ 1S decay. Each tube is 5 cm in diameter with MgF_2 windows and semi-transparent CsI photocathodes. The phototubes are solar blind with a relatively narrow spectral acceptance (1150–2200Å). The lower energy limit is the result of the ionization potential of the CsI photocathode and the upper limit follows from the transmission through the MgF_2 window [Sam67]. Unfortunately, in the accelerator environment there are many charged particles which contribute substantially to the background seen by these tubes. The CsI photocathode has a high photoelectron quantum efficiency (Q.E. $\sim$ 15–20%) [Taf57] over its active area of 4.4 cm diameter and the MgF_2 transmission is $\sim$ 50% at 1221Å [Wil79]. The larger Q.E. available with an opaque photocathode is not enough to offset the loss in solid angle. The total efficiency claimed by the manufacturer is 10% [Ham83]. The relative pulse heights were measured with a Hg lamp and quartz vacuum window mounted to the downstream end of the apparatus. No deterioration in the UV signals was detected over the course of the experiment.

The four tubes are mounted an average of 6.0 cm from the beam axis, symmetrically about the four sides of the microwave cavity. They subtend a solid angle of 18%. Each tube is mounted in a copper cylinder 7.5 cm in diameter and covered by a 95% transparent Cu mesh to reduce RF pickup from the microwave system, from the accelerator and from the silicon controlled rectifier (SCR) magnet power supplies. A diagram of the voltage distribution to the tubes is seen in Figure 4.3. The signal from each tube is sent through a preamplifier immediately outside the vacuum can and then is again amplified and discriminated in the counting house. Two thresholds are set for each tube: a lower level constant fraction discriminator (CFD) to discriminate against noise and an upper level leading edge discriminator to discriminate against large pulse-height charged particles. These two thresholds

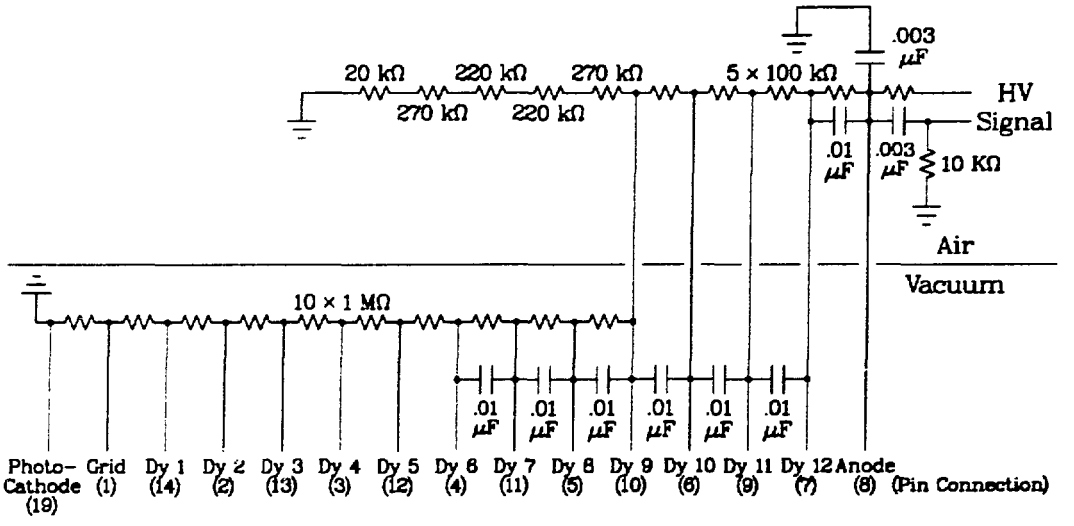

Figure 4.3: Lyman Alpha phototube base circuit diagram

are centered around the single photoelectron peak, nominally cutting off about 10% of the distribution at each end and rejecting as much background from other processes as possible. A condition of one and only one tube firing between these levels is imposed. One major source of background counts comes from beam positrons; even with the upper level veto some positrons will give pulse heights similar to a single photoelectron. Therefore, good positron rejection from the separator is necessary.

4.1.3 Microchannel Plate

The ground state muonium atom is detected by a microchannel plate detector (MCP) after it has passed through the microwave region. The MCP is not selective for the ground state, it also detects metastable muonium atoms that are not quenched, μ^+, and, with less efficiency, e^+. When the MCP signal is placed in coincidence with the Ly_α detector, the background from these other sources is greatly reduced.

The MCP is manufactured by the Galileo Electro-Optics Corporation (Model 3075) and consists of a pair of individual microchannel plates arranged in a chevron

configuration. The plates are constructed of a matrix of lead glass tubes, or fibers, with an open area fraction of $\sim$ 55%. The fibers are oriented at an 8° angle relative to the perpendicular to the surface of the plate and the two plates are oriented such that the angle between the fibers in the separate plates is 16°. This configuration reduces the ion feedback from positive ions liberated near the anode that travel back through the channels to the front surface and liberate secondary electrons that produce after-pulsing. The fiber diameter is 25 μm with a spacing of 32 μm and a length to diameter ratio of 90:1. The high resistance of the glass and a reasonably high secondary electron coefficient give a large gain for this continuous dynode electron multiplier [Wiz79].

To optimize the detection of muonium relative to positrons, the MCP is operated at 1900 V, corresponding to 685 V across each plate. This setting was determined as optimum in earlier measurements with M, μ^+, and e^+. No data on the efficiency of the MCP for detection of muonium is available, but from earlier experiments using H and p^+ beams the efficiency was determined to be $\sim$ 65$\pm$10% [Ort85,Gao84]. For this experiment, position sensitivity is not needed so a simple flat anode with no position read out is installed behind the second plate. A circuit diagram is shown in Figure 4.4. The active area of the MCP is 44 mm^2 and subtends a solid angle of 1% in the forward direction from the MWPC. The typical rise times for the MCP are on the order of 2–5 ns, so a fast preamp (manufactured at the University of Heidelberg), with a 2 ns rise time is used to amplify the signals further. For the case of poor vacuum the plates can be damaged by high voltage breakdown, so the high voltage for the MCP is interlocked to the pressure in the vessel. An increase of the vacuum to 10^{-5} Torr activates a relay that disconnects the HV from the MCP. The MCP is mounted on a retractable stainless steel rod with an O-ring vacuum seal. When muonium formation measurements are made the MCP is moved out of the beam path.

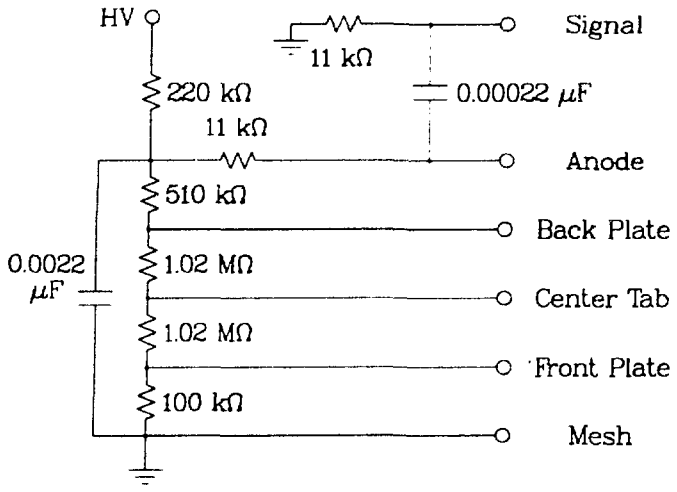

Figure 4.4: MCP Circuit Diagram

4.2 Microwave System

The requirements for a microwave system to drive the $2^2S_{1/2}$–$2^2P_{3/2}$ transition include a generating source in the X-band region, from 8.0–12.5 GHz. A power amplifier, as well as power and frequency measurement capabilities are needed. The dimensions of the cavity are dictated by the size of the beam, which is of the order of 5–10 cm in diameter. This requirement determines the choice of cavity dimensions and necessitates the choice of a high mode number to excite the cavity. In addition it is necessary to be able to tune the frequency across the range of the atomic transition, from 9.0–11.0 GHz. The microwaves must be available inside of the vacuum system for interaction with the atomic beam.

4.2.1 Microwave Circuitry

A schematic of the microwave circuit is shown in Figure 4.5. The microwaves are generated by a HP 2655A klystron and HP 716B power supply. The microwave source is phase-locked by a HP 2650A oscillator synchronizer either to its own internal oscillator or to an external source. The external source is used to lock the

microwaves at frequencies not accessible using the internal source. The output of a frequency synthesizer (HP 5105A Frequency Synthesizer/HP 5110B Synthesizer Driver) is amplified (ENI 503L RF Power Amplifier) and provides an external reference for the oscillator synchronizer. When the klystron is locked the frequency is stable to $\sim$ 100 Hz; when it is not locked the frequency is stable only to $\sim$ 100 kHz. The microwave signal is sampled at -20dB through a directional coupler by a frequency counter (HP 5255A Frequency converter and HP5245L Electronic Counter); the main part of the signal is amplified by a Hughes 8020H Travelling Wave Tube amplifier (TWT) which is protected at the output end by a one-way line. The input to the TWT is modulated by a PIN diode (HP8734B) driven between full open and full closed every 64 accelerator beam gates ($\sim$ 1Hz). The switching is done between accelerator beam gates. The rise and fall times of the switching circuit are $\sim$ 100 μs, which is small compared to the beam gate spacing of 8 ms.

The input power (P_{In}) and reflected power (P_{Refl}) are then monitored by back-to-back directional couplers after the one-way line and before the microwaves enter the vacuum chamber. The signal is sampled at -20 dB in each directional coupler. The P_{In} signal is further attenuated by another factor of 20 dB and is then measured by an HP8478B thermistor mount and HP432A power meter. The P_{Refl} signal is attenuated by 6 dB and is measured by an HP478A thermistor mount and HP431B power meter. The microwaves are then fed into the vacuum apparatus by a 0.64-cm diameter semirigid cable through a metal vacuum seal (Swagelok fitting). Inside the vacuum, the 0.64 cm cable is adapted to a 0.36 cm semirigid cable, which is brazed to the cavity. A second antenna samples the power in the cavity and is fed back out of the vacuum in the same manner. This transmitted power (P_{Tran}) is monitored through another directional coupler at -30 dB by an HP478A thermistor mount and an HP432A power meter.

4.2.2 Microwave Cavity

The microwave cavity (see Figure 4.6) is a rectangular parallelepiped made of five plates of 0.48 cm thick copper screwed together at each edge in a tongue and groove construction. The sixth side rests inside the box on microwave finger stock and is

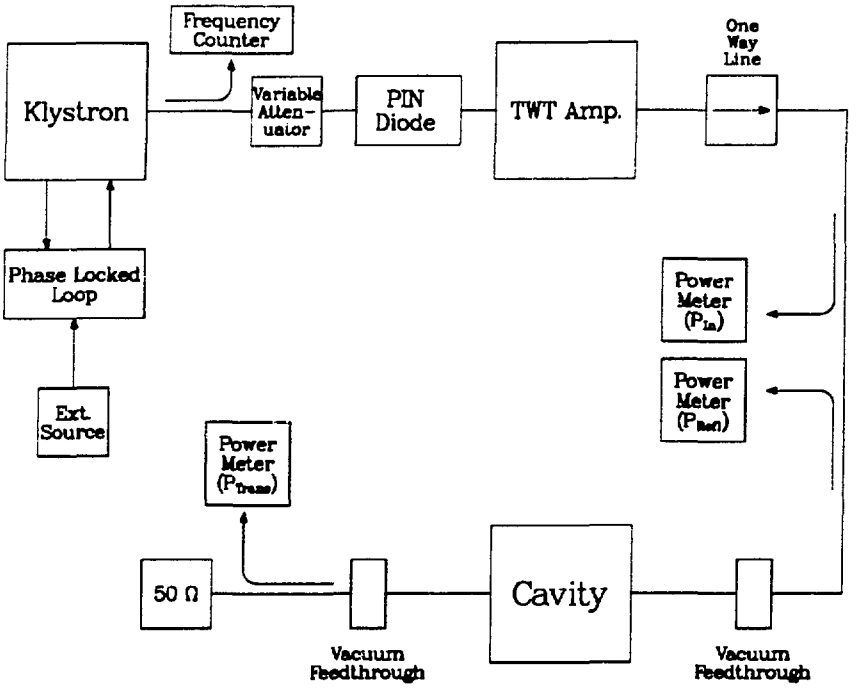

Figure 4.5: Microwave Circuit for 10 GHz Muonium Fine Structure Transition

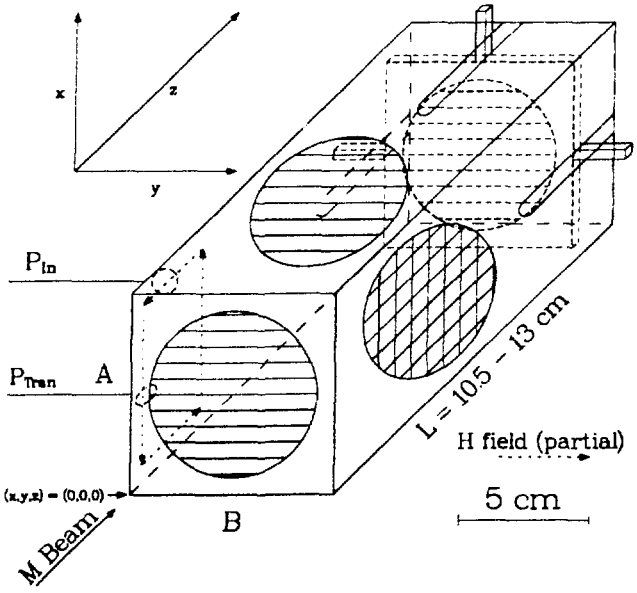

Figure 4.6: Microwave Cavity

guided along three grooves cut into the side walls. This wall is moveable to allow for the tuning of the cavity at different microwave frequencies. The cavity has circular holes cut in all six sides to allow for the passage of the muonium atoms through the cavity and to allow the detection of the Lyman alpha photons produced in the cavity. Five of the windows are 7.0 cm in diameter, whereas the hole in the back wall has a diameter of 6.0 cm. The openings on the front, back and two sides are covered by 20 μm Au-plated W wires strung with a 2 mm spacing, giving a 99% transmission fraction. The other two sides are covered by electroformed copper mesh, with a 5.0 wire/cm spacing and a transmission of 89.7%.

The outer dimensions of the cavity are 8.9 cm $\times$ 8.9 cm $\times$ 13.5 cm. The cavity has inner dimensions of 8.03(1) cm by 7.957(5) cm with a length variable from 10.5–13.0 cm. The sixth, or downstream, wall of the cavity is moved by an electric motor located inside the vacuum system. By moving the back wall, the resonance frequency of the cavity can be varied across the frequency range of the atomic transitions. The position of the back wall is monitored through the use of a variable resistor attached to the movable cavity wall. A potential is applied along the length

of the resistor and the voltage at the variable contact is read out. This signal is fed into another variable voltage divider outside the vacuum system to calibrate the digital volt meter (DVM) readout to $\sim$ 1 V/cm. Two comparators are used as limit switches to prevent the wall from being driven off the groove. A switch controls the direction of motion and a variable resistor controls the speed. There is hysteresis in the motion of the back wall, so the measurements of wall position are made with the wall moving in the upstream direction.

The motor and drive mechanism and, hence, the back wall are mounted onto a stainless steel block welded into the vacuum can. The cavity, on the other hand, has a brass plate screwed onto one side which in turn is mounted with set screws onto one of the copper shields for the Ly_α tubes. Three adjustment screws on the drive mechanism allow alignment of the cavity and the back wall. Extensive calibration measurements of the DVM in volts vs. the length (L) of the cavity in cm give a relationship between L and DVM.

$$L(\text{cm}) = 12.94(1) - 1.000(8) \times \text{DVM} \tag{4.1}$$

The effective cavity dimensions may be quite different, however, given the large surface area of the mesh and wire windows. By measuring the voltage across the variable resistor at the center of the cavity resonances for a number of different microwave frequencies several known modes are fit to find the cavity dimensions (see Figure 4.7). The frequencies of the cavity resonances ω_o can be expressed in terms of the Q, or quality factor, and the dimensions of the cavity:

$$\omega_o = 2\pi\nu = \pi c\sqrt{\left(\frac{\ell}{A}\right)^2 + \left(\frac{m}{B}\right)^2 + \left(\frac{n}{L}\right)^2}\left(\frac{1}{1+\frac{1}{2Q}}\right) \tag{4.2}$$

The indices ℓ, m, and n identify in which mode the cavity is resonating. The fitting parameters are the cavity dimensions A and B and the calibration constants relating the voltage readout to the cavity length L. The fits are made with a single value for the Q of the cavity as a fixed parameter. The final cavity dimensions are not sensitive to the value of Q. The Q measurements are discussed in more detail in Section 4.2.4. The typical χ^2 per degree of freedom for these fits is 2.0. We find the

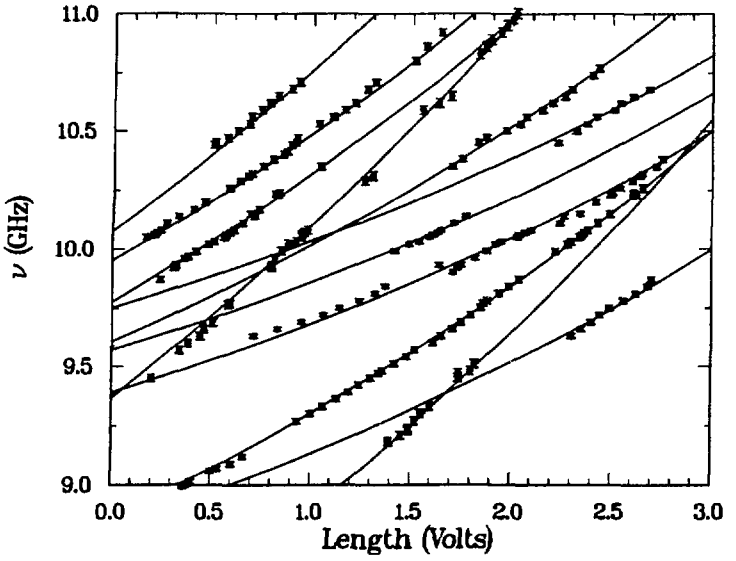

Figure 4.7: Fit to the Cavity Dimensions

effective cavity dimensions are

$$\begin{aligned} \mathrm{A} &= 8.04(1)\ \mathrm{cm} \\ \mathrm{B} &= 8.04(1)\ \mathrm{cm} \\ \mathrm{L} &= [13.02(2) - 0.984(2) \times \mathrm{DVM(Volts)}]\ \mathrm{cm} \end{aligned} \tag{4.3}$$

The meshes serve to make the cavity effectively larger by a small amount. This effect can be understood as a leakage of the microwaves through the meshes, filling a slightly larger volume.

The input coupling antenna is a loop with an average inner radius of 0.27(5) cm which couples to the H_z component of the field (see Figure 4.6). The plane of the loop is parallel to the x–y plane. The center of the loop is located at (x_i, y_i, z_i)=(A-0.50(3),0.92(2),0.75(3)), where the coordinate system is defined in Figure 4.6. The x-position is chosen to be as close to the wall as possible and the z-position is chosen to be approximately 1/4 wavelength from the front wall. This antenna couples to all $TE_{\ell 0n}$ modes with large n. The indices $\ell, 0$, and n refer to the mode numbers in the $\hat{x}, \hat{y}$ and $\hat{z}$ directions, respectively.

The output antenna loop, for monitoring the degree of coupling to the mode of interest (P_{Tran}), is located at (x_o, y_o, z_o)=(A/2,0.44(2),0.38(2)). It has an average inner radius of 0.22(5) cm and is oriented to couple to the H_x field component (i.e. the plane of the antenna loop is parallel to the y–z plane). This antenna couples well to all $TE_{\ell 0n}$ modes where ℓ is odd. In addition, the coupling to these modes is not very sensitive to variations in the back-wall position. Coupling to $TE_{0\ell n}$ modes is suppressed by the choice of wires and meshes on the cavity windows. Wall currents flow in the direction of the electric field in the cavity. The four sets of wires oriented parallel to the $\hat{y}$ direction select against $TE_{0\ell n}$ modes with the electric field in the $\hat{x}$ direction.

4.2.3 Mode Measurements

Substantial time has been spent determining in what mode the cavity is resonating. Careful maps of the cavity resonance frequency ν for many cavity lengths L are made experimentally. These can be compared to the calculated mode chart for the cavity. The expression relating the resonance frequency and length is given by Equation 4.2. Figure 4.8 shows the measured and calculated cavity resonances as a function of the resonance frequency ν and resonance length L for the given dimensions and Q of the cavity. An x-y recorder is connected to the wall read out and to the P_{Tran} meter and sweeps of the wall position are made at a sequence of different frequencies from 9.00–11.00 GHz in 10–30 MHz steps. All sweeps are made in the forward direction at a constant wall velocity. Each mode is characterized by the width of the resonance, the height of the resonance and the rate of change in the resonance position with frequency, i.e. the tunability. From this information the various resonances can be assigned to their proper modes. The modes chosen for data taking are TE_{108}, TE_{306}, and TE_{307}. These are well separated from neighboring modes, are well coupled to and cover the frequency range of the atomic transitions. These data taking modes all have only a y-component of electric field. By choosing modes with one transverse mode number of 0 there is no TM mode that is degenerate with the mode of interest. Their power profile is reasonably uniform across the beam profile. A diagram of some of the field lines and the pattern of the power distribution for the TE_{307} mode

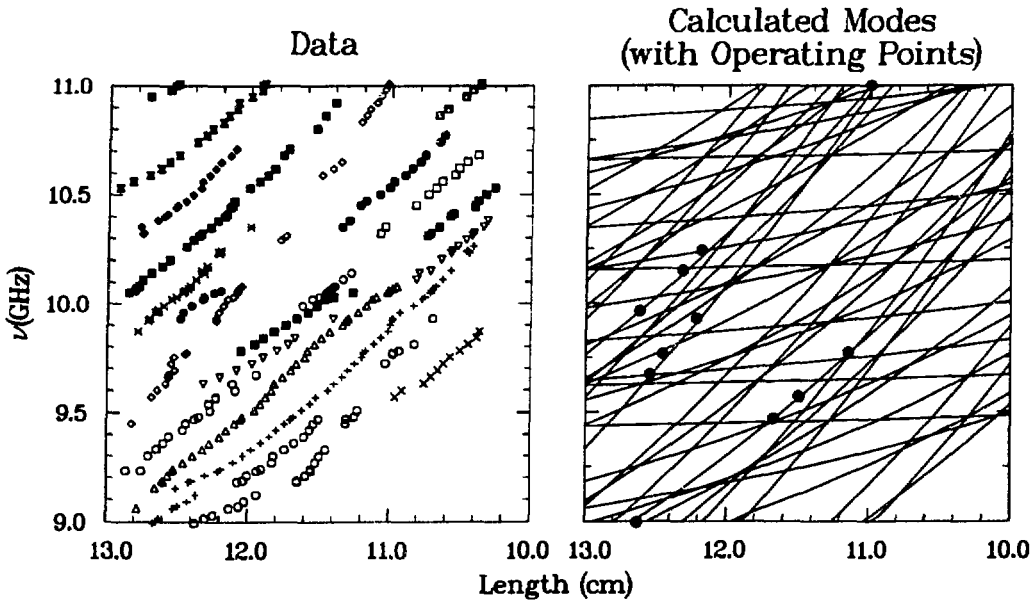

Figure 4.8: Calculated Mode Lines and Data Points for the Microwave Cavity

is given in Figure 4.9. The power has seven peaks along the length and three peaks across the width of the cavity for this mode.

4.2.4 Q Measurements

The Q of the cavity is determined by measuring P_{Trans} through the cavity resonance. The power is Lorentzian in frequency space and, under the condition of small variations in the back-wall position relative to the cavity length, it is Lorentzian in L also.

Attempts to measure the Q by more standard techniques of measuring the reflected power through the resonance by varying the frequency have not been successful due to large reflections from the vacuum feedthrough. Measurements of the reflected power show minima (as well as maxima) with a period of 95 MHz, independent of the cavity back-wall position. With the removal of the cavity and installation of a 50 Ω terminator, the resonance period is increased from 95 MHz to

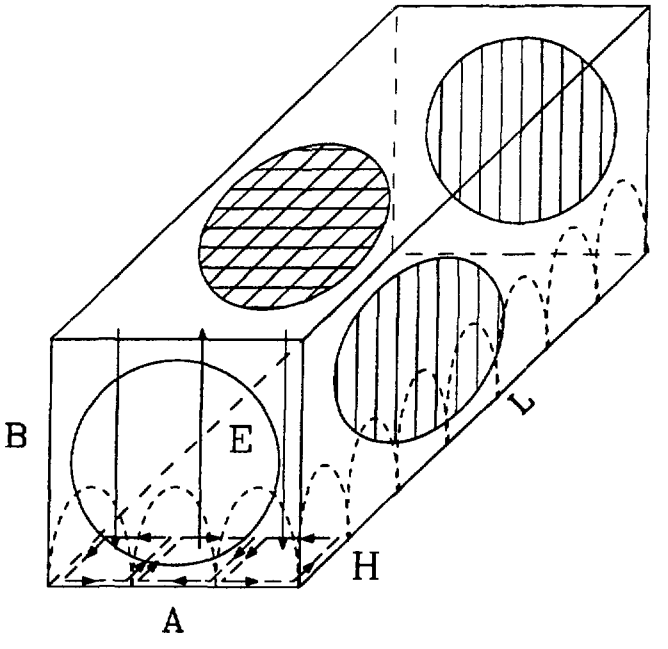

Figure 4.9: Electromagnetic Field Configuration in the Cavity for the TE_{307} Mode

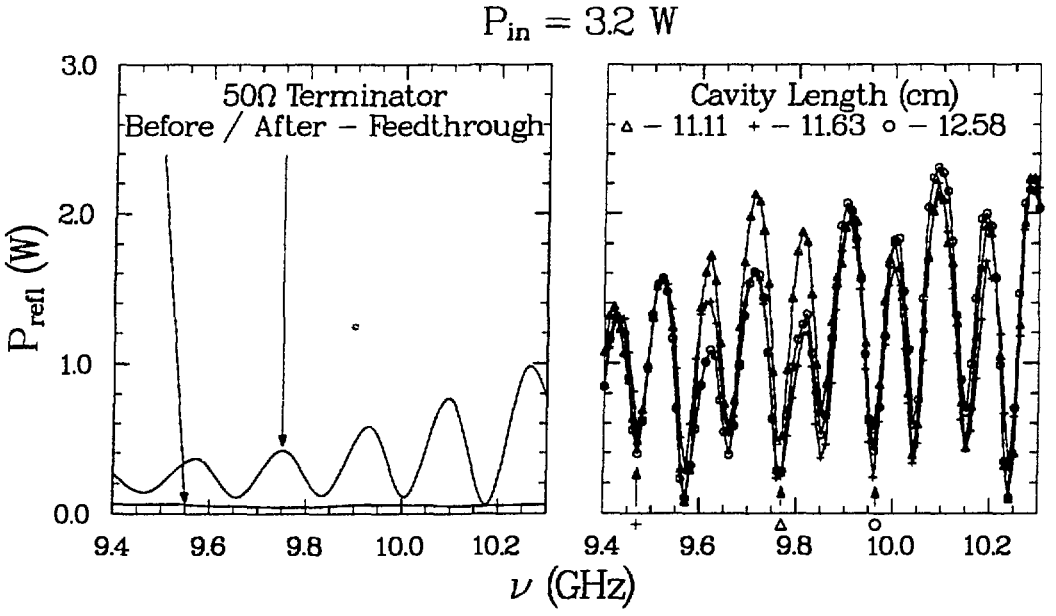

Figure 4.10: Resonances in P_{Refl} with Cavity and with Terminator

175 MHz (see Figure 4.10). With the terminator installed the reflections originate at the feedthrough and with the cavity in place the reflections come from both the feedthrough and the cavity itself.

Therefore, in order to measure the Q of the cavity, we keep the frequency fixed and vary the back-wall position. A sample curve for determining the Q for the TE_{306} mode at 9.770 GHz is shown in Figure 4.11. The transmitted power is plotted as a function of the cavity length. There will be perturbations in the coupling of the output antenna as the wall moves, but these are small. The fractional change in cavity length to span a resonance completely is $\leq 3\%$; this leads to a variation in output power for the $TE_{\ell 0n}$ modes of:

$$\frac{P+\Delta P}{P} \propto \frac{H_x^2(\pm)}{H_x^2(res)} = \frac{\sin^2\left(\frac{n\pi z_o}{1.015L}\right)}{\sin^2\left(\frac{n\pi z_o}{L}\right)} \sim 1.00 \pm 0.03 \qquad (4.4)$$

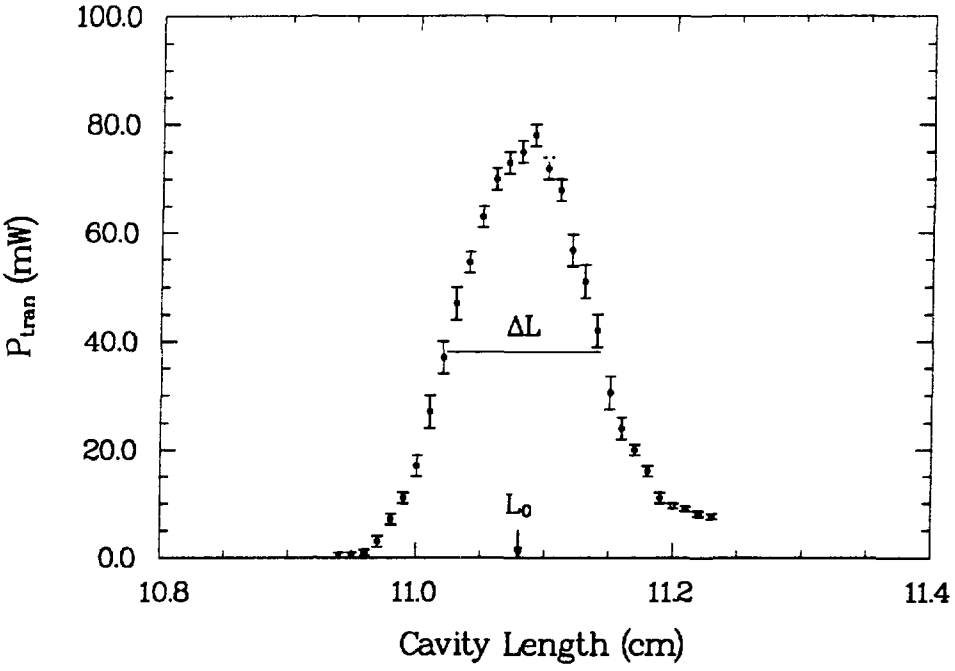

Figure 4.11: Data for the Q measurement at 9.770 GHz

As a function of frequency, the power is given by [Jac75]

$$P(\omega) \propto |E|^2 \propto \frac{1}{(\omega - \omega_1 - \Delta\omega)^2 + \left(\frac{\omega_1}{2Q}\right)^2} = \frac{1}{(\omega - \omega_o)^2 + \left(\frac{\omega_o \cdot [2Q+1]}{4Q^2}\right)^2} \tag{4.5}$$

where ω_1 is the resonance frequency for a cavity with Q=∞ and ω_o is the resonance frequency for the real cavity.

$$\omega_o = \omega_1 + \Delta\omega \simeq \omega_1 - \frac{\omega_1}{2Q} \simeq \omega_1 - \frac{\omega_o}{2Q} \tag{4.6}$$

If we define a new quantity γ such that

$$\gamma = \frac{\omega_o \cdot [2Q+1]}{4Q^2} \tag{4.7}$$

and then normalize the Lorentzian, we obtain an expression for the lineshape of the Q resonance curve as a function of frequency.

$$P(\omega) = \frac{P(\omega_o) \cdot \gamma^2}{(\omega - \omega_o)^2 + \gamma^2} \tag{4.8}$$

By defining Δ such that $\Delta \equiv L - L_o$, and making use of Equation 4.2 and using the fact that $\Delta/L \ll 1$, P(ω) can be rewritten in terms of the length L

$$P(L) = \frac{P(L_o) \cdot \gamma'^2}{\Delta^2 + \gamma'^2} \tag{4.9}$$

where

$$\begin{aligned} \gamma' &= \frac{L_o^3}{n^2} \cdot \left[\left(\frac{\ell}{A}\right)^2 + \left(\frac{m}{B}\right)^2 + \left(\frac{n}{L_o}\right)^2\right] \cdot \frac{2Q+1}{4Q^2} \\ &= \gamma \times \frac{L_o \cdot \omega_o}{\pi^2 c^2} \cdot \left(\frac{L_o}{n}\right)^2 . \end{aligned} \tag{4.10}$$

The expression for Q is

$$Q = \left(\frac{2\nu_o L_o}{nc}\right)^2 \frac{L_o}{\Delta L}\left[1 + \frac{\Delta L}{2L_o} \cdot \left(3 - \frac{1}{a}\right)\right] \cdot \left[1 - \frac{1}{2Q}\right] \tag{4.11}$$

where L_o is the center of the resonance at the frequency ν_o, ΔL is the length between half power points, a=$1+\left(\frac{\ell L_o}{nA}\right)^2$ and the two terms in brackets are correction terms

arising from the fact that the power profile is not strictly Lorentzian in length and from the fact that there is a shift in the cavity resonance from the finite Q. These two terms contribute corrections at the 1% level. The width of the resonance ΔL and the center L_o are obtained from measurements such as shown in Figure 4.11. With these measurements, the known cavity mode and dimensions, the measured frequency ν_o and Equation 4.11 the Q at each of the data conditions is determined.

Given the simple geometry of the cavity, we can calculate the Q of a solid cavity of the same dimensions for any given mode [Mon47]. For the real cavity we can replace the single skin depth for Cu by a combination of the skin depth of copper and an effective skin depth, δ_m, of the windows. For a $TE_{\ell 0n}$ mode the expression for the Q is given by

$$Q \times \frac{\delta}{\lambda} = \frac{\mathrm{ABL}}{2} \times \frac{(p^2 + r^2)^{3/2}}{p^2 L(A + 2B) + r^2 A(L + 2B)} \tag{4.12}$$

where p = l/A, r = n/L and the skin depth for Cu is $\delta_{\mathrm{Cu}} = 6.5 \times 10^{-5}$ cm. The fraction f of the total cavity surface area that is solid copper varies with the cavity length from 60.6% at 13.0 cm to 54.5% at 10.5 cm. If the skin depth of the cavity is written as

$$\delta = (1 - f) \cdot \delta_m + f \cdot \delta_{Cu} \tag{4.13}$$

the relative Q values for each of the data points can be calculated and compared to the measured values (see Table 4.1). By fitting to the measured Q values the value of δ_m is calculated to be 0.41(2) mm. The fit is not very good due to the large variation in the measured Q values, so this result is probably best treated as a order of magnitude estimate. With the 2.0 mm spacing of the wires and meshes on the cavity, a value of 0.4 mm for a penetration depth of the microwaves ($\lambda \sim 3.0$ cm) does not seem unreasonable.

4.2.5 Power Measurements

The input and reflected power are both measured with directional couplers placed in the circuit before the vacuum feedthrough. The various components in each of these circuits are measured for their frequency response in order to determine the relative

ν	Mode	λ (cm)	L (cm)	Q·δ (cm)	Q δ_m=0.41mm	Q meas.
8.995	TE_{306}	3.333	12.67	3.169	194(2)	226(4)
9.470	TE_{306}	3.166	11.71	3.114	181(2)	234(13)
9.570	TE_{306}	3.133	11.53	3.104	178(2)	172(3)
9.670	TE_{108}	3.100	12.58	3.504	213(2)	104(13)
9.765	TE_{108}	3.070	12.47	3.483	211(2)	168(8)
9.770	TE_{306}	3.068	11.19	3.076	173(2)	163(7)
9.930	TE_{108}	3.019	12.24	3.454	207(2)	142(21)
9.965	TE_{307}	3.008	12.67	3.227	197(2)	210(13)
10.150	TE_{307}	2.954	12.35	3.207	193(2)	175(8)
10.240	TE_{307}	2.928	12.19	3.197	191(2)	246(16)
11.002	TE_{108}	2.725	11.02	3.260	182(2)	230(19)

Table 4.1: Calculated and Measured Cavity Q Values

powers at each frequency. The attenuation coefficients are measured relative to the P_{In} thermistor mount. The resistive losses in the feedthrough were not measured, but these should not be very frequency dependent and therefore only contribute as a scaling factor to the power. To determine the relative electric field strength in the cavity the reflected power is subtracted from the input power

$$P_{Cav} = P_{In} - P_{Refl} \tag{4.14}$$

This represents an estimate of the power introduced into the cavity. As the resistive losses were not measured this represents an upper limit on the power in the cavity.

4.2.6 Average Electric Field $\overline{E}$

The energy U stored in the cavity can be written in terms of the electric field:

$$U = \frac{10^7 \cdot A \times B \times L}{32\pi c^2} \cdot |E_o|^2 \tag{4.15}$$

where A×B is the cross sectional area and L is the length of the cavity, as given by Equation 4.3. E_o is the amplitude of the electric field, where the field equations for

the $TE_{\ell 0n}$ modes are given by

$$\begin{aligned} E_y &= E_o \cdot \sin(k_x x)\sin(k_z z)\cos(\omega t) \\ H_x &= E_o \cdot \frac{k_z}{\mu_o c k} \cdot \sin(k_x x)\cos(k_z z)\sin(\omega t) \\ H_z &= -E_o \cdot \frac{k_x}{\mu_o c k} \cdot \cos(k_x x)\sin(k_z z)\sin(\omega t) \end{aligned} \tag{4.16}$$

The wave vector k is given by $k^2 \equiv k_x^2 + k_z^2$, where $k_x = \ell\pi/\mathrm{A}$ and $k_z = n\pi/\mathrm{L}$. The stored energy can also be expressed in terms of the Q of the cavity:

$$U = \frac{P \times Q}{\omega_o} \tag{4.17}$$

From these two expressions for U we can derive an expression for the square of the amplitude of the electric field:

$$\begin{aligned} |E_o|^2 &= \frac{P \times Q}{2\pi\nu} \times \frac{32\pi c^2}{10^7 \cdot A^2 \cdot L} \\ |E_o|^2 &= \frac{P \times Q(\mathrm{Watts})}{\nu(\mathrm{GHz}) \times \mathrm{L(cm)}} \times 222.5(3) \end{aligned} \tag{4.13}$$

In order to determine the average value of electric field experienced by the 2S muonium atoms as they traverse the microwave cavity, it is important to note that the cavity is larger in cross sectional area than the beam and that the beam traverses only the central cavity region. The spatial distribution of the M(2S) beam has not been measured, but from TRANSPORT calculations of the incident μ^+ beam and Monte Carlo calculations and measurements of the muonium distribution, an assumption of a uniform distribution over the acceptance of the apparatus seems reasonable. The cavity cross sectional area A×B is 64 cm^2; the beam area varies from 20–28 cm^2 as it traverses the cavity. For each cavity mode the electric field is averaged over a cylinder of diameter 5.5 cm, the average beam diameter and length L. For a given input power the average electric field experienced by the beam is smaller for the TE_{30n} modes than for the TE_{108} modes. The uncertainty in determining the average electric field is taken as the calculated values for the extreme diameters, 5.0 cm to 6.0 cm. This leads to a variation in $\overline{E}^2_{108}/\overline{E}^2_{30n} = \pm 9\%$ for a given power. The average fields for the TE_{108} and TE_{30n} modes are given by

$$\overline{E}_{108} = E_o \times 0.616(41)$$

ν (GHz)	Mode	Length (cm)	P_{In}^{meter} (mW)	P_{Refl}^{meter} (mW)	P (Watts)	Q	E_o (V/cm)	$\overline{E}$ (V/cm)
8.995	TE_{306}	12.66	0.840	1.68	7.7(5)	226(4)	58(2)	29(4)
9.470	TE_{306}	11.71	0.755	2.08	5.8(5)	234(13)	52(2)	26(3)
9.570	TE_{306}	11.54	0.715	1.51	5.8(4)	172(3)	45(2)	22(3)
9.670	TE_{108}	12.57	0.630	0.92	5.8(4)	104(13)	33(2)	20(2)
9.765	TE_{108}	12.48	8.10	1.60	7.3(5)	168(8)	47(2)	29(2)
9.770	TE_{306}	11.19	0.745	1.41	6.4(4)	163(7)	46(2)	23(3)
9.930	TE_{108}	12.25	1.11	9.20	5.7(9)	142(21)	39(4)	24(3)
9.965	TE_{307}	12.65	0.730	1.64	6.2(5)	210(13)	48(2)	23(3)
10.150	TE_{307}	12.35	0.848	3.40	6.9(5)	175(8)	46(2)	23(3)
10.240	TE_{307}	12.22	0.660	2.00	5.7(4)	246(16)	50(2)	24(3)
11.002	TE_{108}	11.02	9.40	3.20	9.0(5)	230(19)	62(3)	38(3)

Table 4.2: Summary of Microwave Data for each Frequency Point

$$\overline{E}_{30n} = E_o \times 0.488(59) \tag{4.19}$$

A summary of the microwave data and the calculated $\overline{E}^2$ for each frequency point is given in Table 4.2.

4.3 Electronic Circuitry

The purpose of the signal electronics circuitry is to provide a very loosely defined trigger. Most of the processing is done in software. Given the very low event rate, the rather large acceptance trigger did not lead to very much dead time for the data acquisition. The trigger rate is 1 Hz, with a dead time of 0.5%. The dead time in the beam gate is higher, but still very reasonable, 7%. Some very restrictive gates are set up in hardware, however, as a means of monitoring event rates on-line (on-line software reconstruction is also available).

4.3.1 Lyman Alpha Logic

The conceptually simplest signature for the Lamb shift would be to measure the Ly_α rate as a function of microwave frequency, but because of the very large background rates, it is not only necessary to make a coincidence experiment, it is necessary to take great care in defining the Ly_α signal. The four phototube signals are discriminated using Ortec 934 Constant Fraction Discriminators (CFD's) set above the noise level $L_{1/4\downarrow}$. They are also discriminated at a higher level $L_{1/4\uparrow}$ as a veto for large pulse heights from charged particles. A coincidence $L_{2/4}$ between any of the four lower level thresholds is also used to veto background events. The signature Ly_α for a Lyman Alpha photon is then $L_{1/4\downarrow} \cdot \overline{L_{1/4\uparrow}} \cdot \overline{L_{2/4}}$. The circuit diagram is shown in Figure 4.12.

4.3.2 Triggers

This experiment uses three different triggers, although only two are in operation at any given time. One trigger is set after counting a fixed number of beam gates (BG's), typically 64, and is used to read out the scalers and to switch the microwaves (or static quench grids) on and off. This trigger is labeled Event 6. A second trigger, Event 7, is used during the M formation part of the experiment; this trigger has two parts to it—to signal an event in the NaI and, when the MCP is mounted in its downstream position, to indicate an event in the MCP. The third trigger,Event 8, is used during the RF and static quench portions of the experiment to indicate a candidate M(2S) $\longrightarrow$ M(1S) event.

Event 6

A schematic diagram for the Event 6 trigger is given in Figure 4.13. This trigger is based on a flip-flop made of two coincidence units. After every 64^{th} beam gate the state of this flip-flop changes and the state of the electric field or microwaves also changes from off(on) to on(off). These transitions are delayed by 3 ms, approximately midway between beam gates, to minimize any effects from switching transients being detected in the MCP and Ly_α detectors. Each change of state also

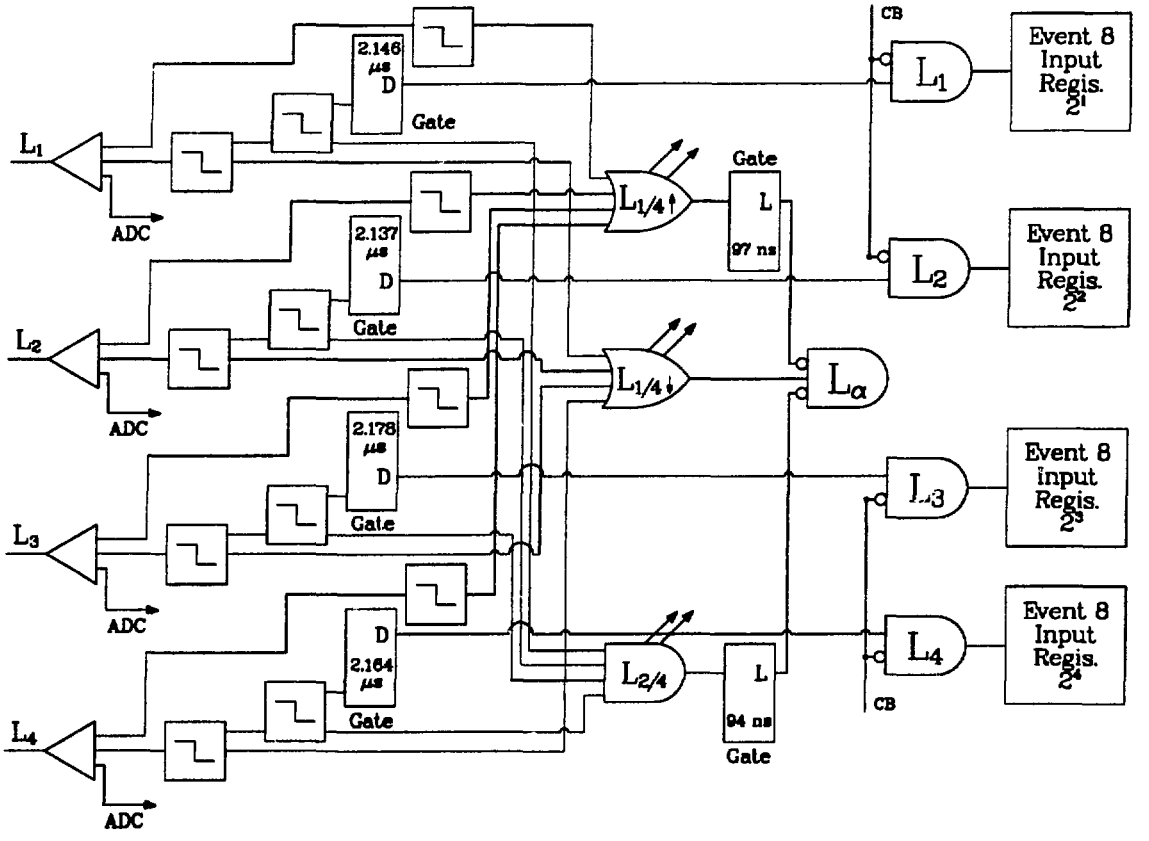

Figure 4.12: Lyman Alpha Signal Electronics

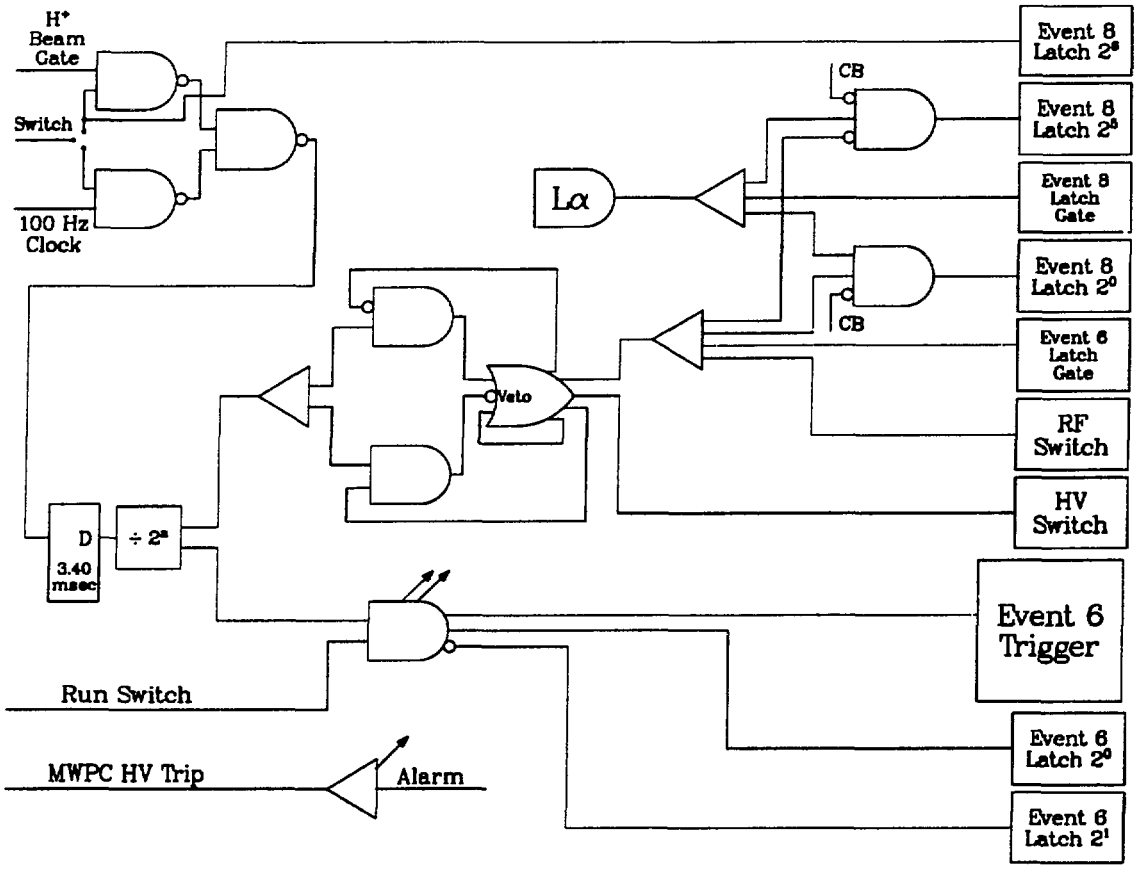

Figure 4.13: Event 6 Trigger Electronics

triggers the CAMAC scalers and an input register to be read. The input register, a Jorway Corporation Model 65 12 bit Input Register, records the state of the microwaves(static **E** field) and the scalers are used to monitor all aspects of the experiment. A listing of the scalers is given in Table 4.3.

Two modules, or 24 channels of scalers, are vetoed by the computer busy signal CB; three other modules are vetoed by the computer busy or the absence of the beam gate (CB + $\overline{\text{BG}}$); and one module is read by the Event 8 trigger (see Section 4.3.2). The scalers read by the Event 8 trigger are used to check for periodicity between triggers.

Ch.	$\overline{CB}$	$\overline{CB}$	$\overline{CB}$	BG·$\overline{CB}$	BG·$\overline{CB}$	BG (Event 8)
0	MWPC	$\mu_{(clean)}$	Ev I	MWPC	$\mu_{(clean)}$	
1	MCP	$CP_{(clean)}$	Ev II	MCP	$CP_{(clean)}$	
2	Ly_α	$Ly_{\alpha(clean)}$	Acc	Ly_α	$Ly_{\alpha(clean)}$	
3	$L_{1/4\downarrow}$	$2^{nd}\mu$	Good Event	$L_{1/4\downarrow}$	$2^{nd}\mu$	
4	$L_{1/4\uparrow}$	2^{nd}CP	Good μ	$L_{1/4\uparrow}$	2^{nd} CP	
5	$L_{2/4}$	$2^{nd}Ly_\alpha$	Good CP	$L_{2/4}$	$2^{nd}Ly_\alpha$	
6	L_1	Veto	Good Ly_α	L_1	Veto	
7	L_2	NaI·e^+	μ event	L_2	NaI·e^+	Event 6
8	L_3	$CP' \cdot e^+$	CP event	L_3	$CP' \cdot e^+$	p-click·BG
9	L_4		Ly_α event	L_4	Event 7	p-clicks
10	p-clicks		Event 6	p-clicks		10kHz·BG
11	10kHz		Event 8	10kHz	Alarm	10kHz

Table 4.3: CAMAC scalers

It is also possible, when the beam is off, to take data using a variable duty factor clock, instead of the accelerator beam gates, in order to measure non-accelerator associated background rates. The source of the trigger (either beam gates or clock) is recorded in an input register and read out with the TDC's and ADC's (on an Event 8 trigger); the microwave (grid) state is also recorded and read out during an Event 8 trigger.

Event 7

A circuit diagram for the Event 7 trigger is shown in Figure 4.14. The Event 7 trigger is used during the muonium formation runs. The analog NaI and MCP signals are digitized, as is the time between MWPC and MCP. The NaI information is used to determine the number of muonium atoms at a given incident momentum. The TOF information is used to determine the velocity distribution of the muonium atoms and the velocity distribution of the μ^+ when the sweeping magnet is off.

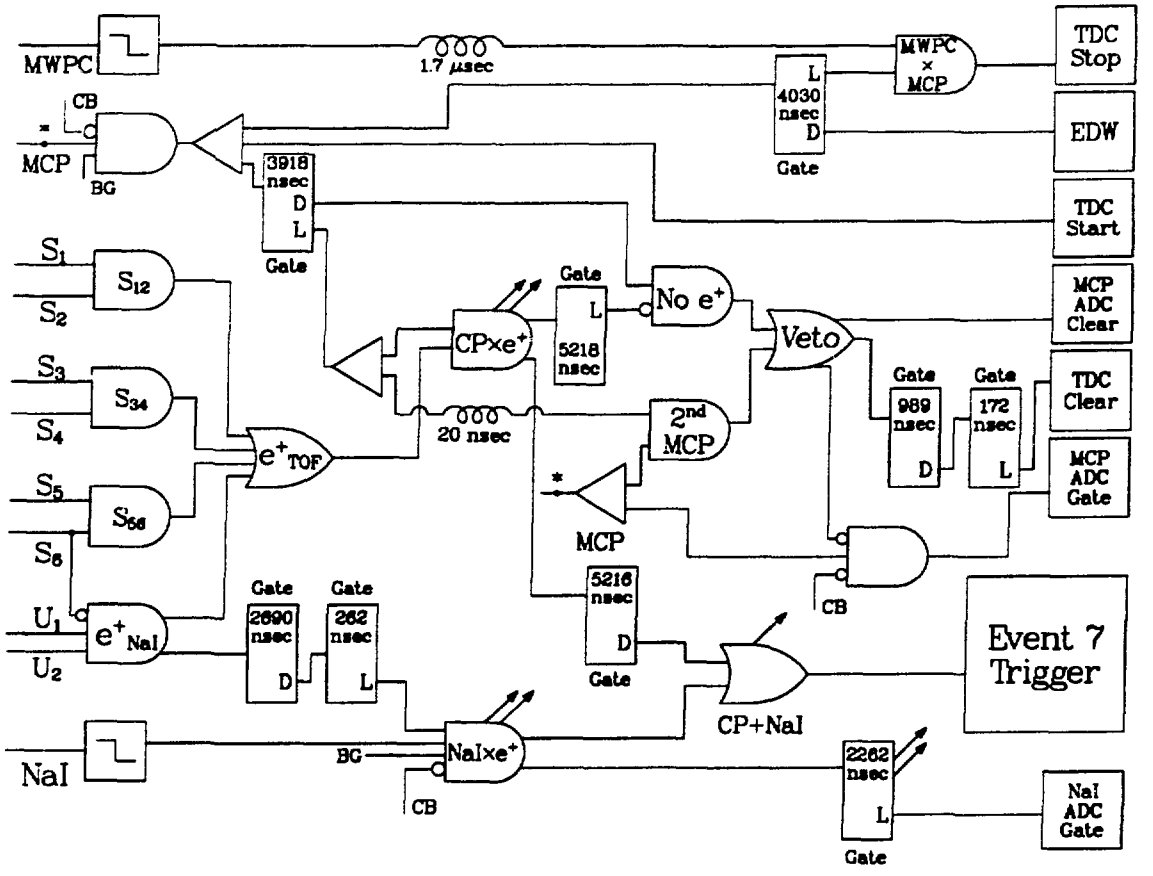

Figure 4.14: Event 7 Trigger Electronics

Event 8

The Event 8 trigger is the main data acquisition trigger for this experiment; it signals the presence of a candidate M(2S) atom that has been quenched. A fairly wide coincidence between the Ly_α and the MCP is made and this coincidence signal is used as the trigger (see Figure 4.15). In particular, the Ly_α signal is used to open a 2 μsec gate. If a MCP signal occurs during this gate, the trigger signal is created. The instantaneous MWPC is high and we expect more than one MWPC signal within the 2 μs gate. Therefore several multi-hit TDC's are used to digitize the time differences between the detectors. The Event 8 trigger reads 16 channels of TDC, 6 channels of ADC, 6 scaler channels, and an input register. The total time to read the data out of the CAMAC crate per trigger is 600 μs.

The ADC's have a shorter gate. The charge sensing ADC's (LeCroy 2248) are gated by the MCP, Ly_α and MWPC logic pulses with the requirement that a MCP arrives within 200 ns of a Ly_α. The widths for the three ADC gates are 7 ns, 10 ns and 50 ns, respectively. The full scale settings on the LRS2248 modules are 64 pC.

The trigger coincidence is also used to open two 2 μsec gates that are used to gate both the TDC starts and the TDC stops. The TDC's used in this experiment are LeCroy 4208 eight stop TDC's. Any combination of the stops can be cascaded together into multi-hit operation. One TDC is started by the MCP and has two separate stops, each in multi-hit mode. The Ly_α can have three hits, and the MWPC stop can have five hits. The second TDC is started by the Ly_α and has a three-hit MCP stop and a five-hit MWPC stop.

The input register, or latch, has seven inputs, one to record whether the beam gates are serving as a clock for the scaler read out, four to record which of the Lyman alpha phototubes has fired, and the last two to record the state of the microwaves (both the status level and its inverse are recorded as a redundancy check). The LRS2341 module is gated by the same signal that serves as the Ly_α TDC start.

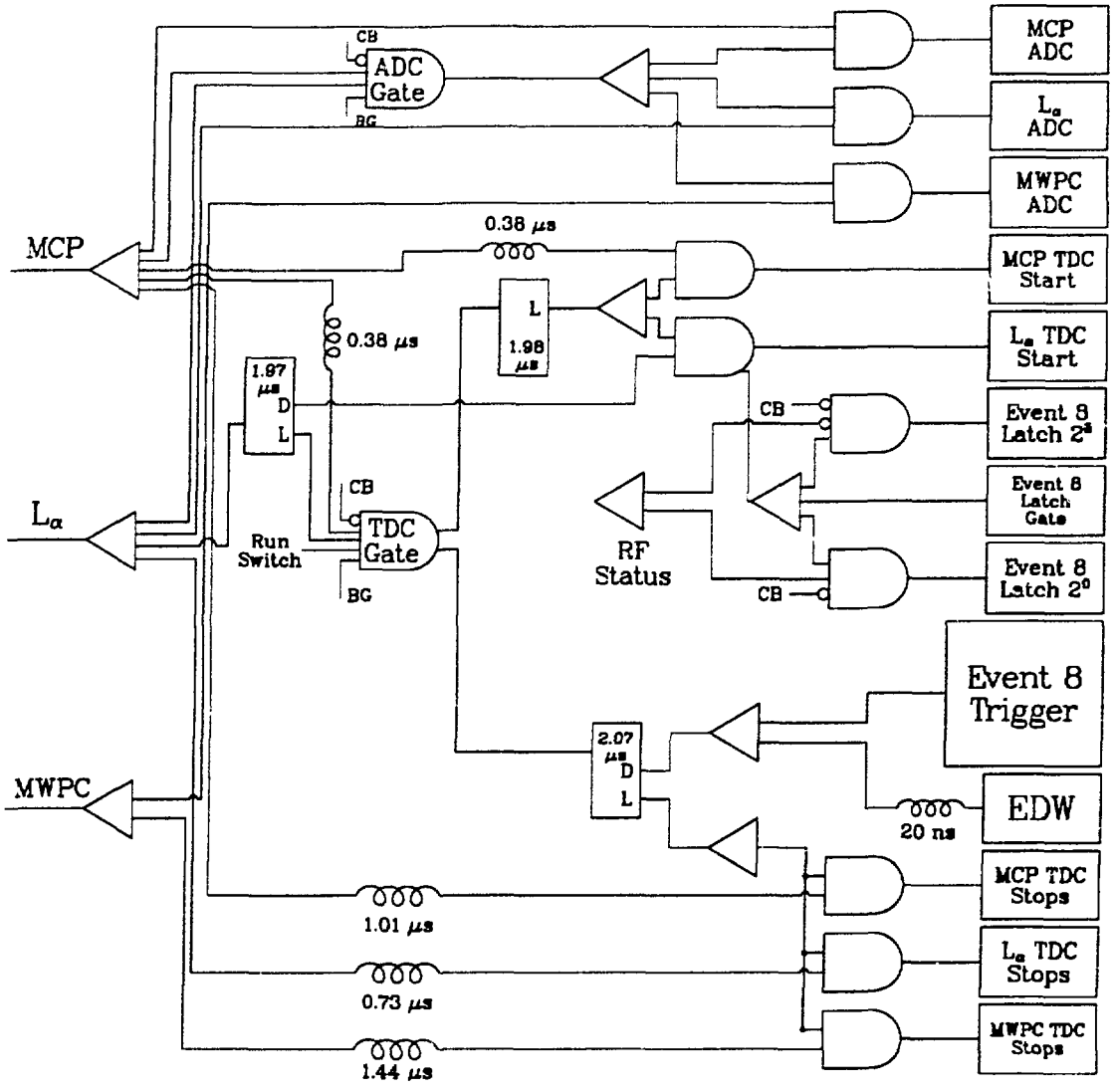

Figure 4.15: Event 8 Trigger Electronics

4.4 Data Acquisition System

The data acquisition system is based on a VAXStation II/GPX mini-computer and the Q software package [MP187]. Other hardware essential to the flow of data from the experiment to tape includes the Microprogrammable Branch Driver (MBD) and the CAMAC Trigger Module, both manufactured by BiRa Systems. The Q software is a modular program from which several of the packaged subsystems as well as several "user written" components are linked together. This code is written in FLECS [MP186], as well as in Assembly language and FORTRAN; the code for the MBD is written in its own specialized language [Shl74].

4.4.1 Microprogrammable Branch Driver / CAMAC

All analog and digital signals from the experiment are sent from the experimental area to the counting house via RG-58 coaxial cables. In the counting house the trigger is formed and further signal processing occurs. The information to be recorded on magnetic tape is fed into several modules in the CAMAC crate (three ADC's, two TDC's and six scalers). The CAMAC crate is controlled by a Standard Engineering Corporation(SEC) CC-A1 controller and a BiRa Event Trigger module serves as a LAM grader and interrupt register. The Trigger module has eight NIM inputs that can be individually enabled or disabled; each event is then flagged in the data stream by the Event number in the Trigger module. The CAMAC crate is read out through a parallel branch highway and dumped into a buffer in the MBD. Several lines of code to direct the readout for each separate Event number are written in the Q Assembly Language (QAL) and loaded into the MBD. The total memory available for both the QAL code and for the data buffer is 8k bytes. The data acquisition is set up such that whenever the MBD memory is filled, the MBD sends an interrupt to the VAX to dump its data into the Q data buffer in the VAX. The QAL code permits several different readout routines according to which input in the Trigger Module has fired. The size of each event readout from the CAMAC varies from 40–240 bytes depending on which event has been triggered.

4.4.2 VAXStation II

The data acquisition for this experiment is controlled by a Digital Equipment Corporation VAXStation II/GPX. This mini-computer is equipped with 5 Mbytes of memory and a 71 MByte hard disk. Since it is a Q-bus based machine it is equipped with a Q–Unibus converter (Able Computer Qniverter II) to interface to the Unibus based MBD. A Dilog tape coupler interfaces to two Kennedy 9100 tape drives (1600 bpi). The VAX Workstation software allows a multiple windowing capability with the DEC VR290 graphics terminal. A second VT100/Retrographics terminal (VT640 emulation) and a Decwriter III are also connected for control and monitoring of the experiment. The MBD reads out the CAMAC crate and serves as an intermediate buffer storage of the data before it is dumped into the computer.

Events are written directly to tape after being dumped from the MBD into the VAX buffer. These same events are then transferred to the various event processing routines.

4.4.3 Data Acquisition Software

The Q software system controlling the data acquisition, which was written at LAMPF, is more fully described elsewhere [MP187]. The Q system is highly modular, consisting of a histogramming system, a test package and a dynamic parameter array as part of a memory management region. In addition there are a cluster of run control programs. The run start program (QRU) reads in calibration constants, including the distances between detectors and the calibration for the TDC's, and various limits for the monitored processes. Each trigger Event then has its own subroutine (written in FORTRAN) that can do any necessary processing, including calling the histogramming or test packages. Other programs, completely separate from the Q system, can be linked with the memory management region and can then access information from the Q system. In this manner a separate scaler program is set up to read the scaler data from the Event 6 trigger.

Several important Event 6 scaler quantities are measured on a regular basis (typically every 300 Event 6 triggers, i.e. every five minutes). The accelerator current

and duty factor, the muon rate, and the MCP and Ly_α rates are all checked to verify that they remain within reasonable limits. In addition whenever the MWPC HV trips, data acquisition is suspended and an alarm sounds.

A separate scaler display program permits the reading of all of the scaler signals during the data-collection period. In addition, histograms using the Q HPL routines provide further on-line information. In particular, the various two dimensional TOF histograms provide a flexible way of checking on the signal rate.

4.5 Experimental Procedure

The 2S state is metastable, and under the experimental conditions its lifetime is dominated by the muon lifetime. The effects from stray electric and magnetic fields is small, as is the effect from collisions with residual air molecules. All surfaces in the experimental apparatus are conducting and well grounded. The apparatus is shielded from magnetic fields with a 100 μm layer of Conetic foil. The measured magnetic field along the beam path, under experimental conditions is $\mathbf{B} = 0.6$ gauss. From the average M(2S) velocity (see Chapter 5) and Equations 2.18 and 2.17, it is seen that for magnetic fields less than 7.5 gauss no appreciable shortening of the M(2S) lifetime occurs. The experimental vacuum is maintained at $\sim 5 \times 10^{-6}$ Torr. The cross section for de-excitation of the 2S state has been measured with hydrogen atoms for a number of gases [Byr70]. The largest cross section was measured for N_2 molecules at a hydrogen energy of 3 keV. If this cross section is used to calculate the probability of collisions with residual air molecules de-populating the M(2S) state, the probability of de-excitation by collisions over the 26 cm flight path is 1%.

A tight hardware timing requirement is used to monitor the experiment and a looser trigger enables writing the CAMAC data to tape. The data are recorded on an event by event basis onto magnetic tape at 1600 bpi. The scalers are written at ~1 Hz and the average Event 8 rate is also ~1 Hz. The scaler data are used to monitor the proton current, the duty factor, the computer live time, and the detector performance. The scaler data are also used for normalization purposes and as one of several methods to measure the signal on-line. The replay program is written to

process data only when the average primary proton current is greater than 300 μA and the duty factor is between 5% and 10%. In addition if the rates in any of the detectors (μ^+ counter, MCP or Ly_α) deviates from its average value by more than 50% the data are not included in the analysis. The purpose of these requirements is to minimize fluctuations in the data taking rate. The rates are normalized to the number of μ^+, so these cuts serve primarily to maintain background conditions as stable as possible.

Two scalers are set up as an on-line monitor of the microwave signal. These demand one and only one μ^+ in a 500 ns interval, and then within 450 ns one and only one MCP and one and only one Ly_α. Two different sets of three-fold coincidences between the MWPC, MCP and Ly_α look for events with a uniform velocity throughout the apparatus. One of these windows has a wide acceptance for the M(2S) velocity and one has a narrow window.

The TDC's have an internal 125 MHz clock and are calibrated using a 200 MHz Fluke synthesizer: for all 16 TDC stops, each time bin corresponds to 1 ns to within five parts in 10^4. The time-zero's are determined from positron runs. At four times during the course of the static quench and microwave experiments, the separator |B| field is turned off, allowing beam positrons to traverse the apparatus. The TOF for a positron from the MWPC to the MCP is 1 ns. The coincidences with the Ly_α tubes are presumably from *bremsstrahlung* in the Pb collimators or the Cu microwave cavity, where the *bremsstrahlung* photons liberate electrons at the photocathode of the tubes and from scattered positrons directly hitting the phototubes. These zero times were later checked for internal self consistency with pulser signals injected into the electronics circuit after the initial discriminators. They agree to within 1.5 ns, where the widths are from 2–4 ns. These widths from the electronics timing jitter are small compared to the total widths measured in the TOF spectra for positrons. The widths of the peaks in the positron TOF are:

- $\Delta T_{\mu^+ \rightarrow MCP} = 24$ ns and
- $\Delta T_{L_\alpha \rightarrow MCP}$ 11 ns

If the positron data are used to estimate the timing resolution for the muon runs,

the fractional width of $T_{\mu^+ \rightarrow MCP}$ for the average muon velocity of 0.30 cm/ns would be 25% and the fractional width of $T_{L_\alpha \rightarrow MCP}$ would be 25%. The timing widths for positron runs may be different than for muons; the pulse development for positrons and muons are very different. While CFD's were used, it may be expected that they were not so well suited for good timing of the positrons. The number of electron-ion pairs produced in the active MWPC region is only 3–5 and the upper level vetos in the Ly_α tubes were removed to get a reasonable rate.

The distances between the detectors for the RF runs, as shown in Figure 4.1 are

- Ly_α - MCP = 11.8(2) cm
- μ^+ - Ly_α = 14.4(4) cm
- μ^+ - MCP = 26.2(4) cm

During the static field quenching experiment the distance from the muon counter to the Ly_α counter was increased to 17.2(4) cm, and the μ^+ to MCP distance was then 29.0(4) cm.

For both static quenching data and the RF data a fast modulation technique is used. The RF(grids) are switched from on to off at a rate of $\sim$ 1 Hz. With this continuous monitoring of the background, drifts in the background rate that might mask the signal or create false signals are reduced. With measurements of the background at each RF frequency, correlations with the other frequency points are minimized. At each RF frequency the back wall of the cavity is moved to maintain the same cavity mode resonance. Before data are taken with the muon beam, a run is made without beam to check that no asymmetry in count rate occurs from pickup of the microwaves in the detectors. This is done without beam, so that the high count rate from the beam does not mask any small asymmetry.

The RF power is monitored continuously through remote readout of the P_{In}, P_{Refl} and P_{Trans} power meters. The RF frequency is monitored remotely through a parallel output of the frequency converter that is monitored in the counting house.

The July 1986 running period was devoted to a search for M(2S) using a static electric field. During this run, with the asymmetric separator field lengths, the

	$Grid_{ON}$	$Grid_{OFF}$	RF_{ON}	RF_{OFF}
μ^+	24.1 kHz	23.7 kHz	37.0 kHz	37.1 kHz
MCP	374 Hz	368 Hz	422 Hz	424 Hz
Ly_α	64.6 Hz	63.9 Hz	50.3 Hz	50.3 Hz

Table 4.4: Average Detector Rates

background from positrons per incident muon was higher than during the RF runs. A total of $3.1\times10^9\mu^+$ were detected. During the RF running in September–October 1986 a total of $3.5\times10^{10}\mu^+$ were detected. The detector rates for both periods are summarized in Table 4.4.

Chapter 5

Data Analysis

The data are replayed on the VAX 8650 cluster at the LAMPF Data Analysis Center using the Q system. The static quench data represents 36 hours of collection time and 132,00 triggers. The RF data, taken at 11 different frequencies represents 250 hours of collection time and 800,000 triggers. The total data storage space from these runs is 360 M bytes.

5.1 Initial Data Processing

The times digitized by the TDC's are the most important data for looking for signals from quenched muonium (2S). Other important information is read from the latch, recording the RF status and which Ly_α tube fired. It is found that a software requirement of one and only one Ly_α tube eliminates about 15% of the data on tape, which presumably is written due to inefficiencies in the hardware veto. All of the TDC processing is done with the calibrated TDC times. All times are calibrated to have forward timing, meaning that a positive time $T'_{a\to b}$ or $T_{a\to b}$ corresponds to an event occurring in the downstream detector(b) after the upstream detector(a). The prime is used to indicate a time that has been calibrated in this fashion, but with no further processing. Only the first stop in the multi-hit TDC's for the time between the Ly_α and the MCP are used; no more than 2% of all first hits are accompanied by a second or third hit. The second and third hits are not

used in any further analysis. The multi-hit TDC's involving the muon counter do have late hits and these are considered further.

Of the four sets of TDC times, $T'_{L_\alpha \to MCP}$, $T'_{\mu^+ \to L_\alpha}$, $T''_{L_\alpha \to MCP}$ and $T'_{\mu^+ \to MCP}$, two measure the same time interval. The time $T'_{L_\alpha \to MCP}$ is measured with a Ly_α start and the time $T''_{L_\alpha \to MCP}$ is measured with a MCP start. The time should be independent of which signal starts the TDC; Therefore, the first hit times $T'_{L_\alpha \to MCP}$ and $T'_{MCP \to L_\alpha}$ are required to agree to within the uncertainty δ_1.

$$\left| T'_{L_\alpha \to MCP} - T''_{L_\alpha \to MCP} \right| \leq \delta_1 \tag{5.1}$$

This requirement uniquely determines the Ly_α and MCP signals. The FWHM of the distribution of differences is 2.4 ns and 1% of the events does not pass this requirement for $\delta_1 = 5$ ns. The hardware trigger (see Section 4.3.2) accepts events with $T'_{L_\alpha \to MCP}$ such that -325 ns $< T'_{L_\alpha \to MCP} < 1670$ ns. Due to the gating of the TDC stops, however, the acceptance of $T''_{L_\alpha \to MCP}$ is smaller, -325 ns $< T''_{L_\alpha \to MCP} <$ 735 ns. The requirement imposed by Equation 5.1 will eliminate events with times greater than 735 ns, corresponding to a M(2S) kinetic energy of 75 eV or less. This requirement accepts most signal events. The actual time-of-flight between the Ly_α tubes and the MCP is then determined to be the average of the two times

$$T_{L_\alpha \to MCP} = \frac{1}{2}(T'_{L_\alpha \to MCP} + T''_{L_\alpha \to MCP}) \tag{5.2}$$

Having selected the Ly_α and MCP signals, the remaining task is to look for likely muon counter signals. Out of the 25 remaining combinations of hits (from two five-hit TDC's), we want to select combinations where the same MWPC signal stopped each TDC. This constraint is accomplished by the requirement that

$$\left| T'_{\mu^+ \to L_\alpha} + T_{L_\alpha \to MCP} - T'_{\mu^+ \to MCP} \right| \leq \delta_2 \tag{5.3}$$

The time δ_2 is chosen to be wide enough to cover the electronics jitter, and is set to $\delta_2 = \delta_1 = 5$ ns. This time is smaller than the dead time from the discriminators. Therefore no muon counter stop can satisfy Equation 5.3 more than once for the same trigger. If no further processing of the signals is done 45% of the triggers will have more than one candidate satisfying the zero-sum requirement. If cuts are

placed on the times $T'_{\mu^+ \to L_\alpha}$ and $T'_{\mu^+ \to MCP}$ accepting a narrower time region around our expected signal, the number of candidates per trigger satisfying Equation 5.3 is greatly reduced. With a reasonable choice of time windows

$$\begin{aligned} 0 \leq T_{\mu^+ \to L_\alpha} &\leq 225ns \\ 0 \leq T_{\mu^+ \to MCP} &\leq 250ns \end{aligned} \tag{5.4}$$

only 0.2% of the triggers have more than one candidate. It is observed that these cuts have little effect on the signal distribution. The small fraction of triggers with more than one candidate are not processed further. It is observed that if these cuts on the initial times are not limiting the final cuts (see Section 5.2), the final signal is not sensitive to variations in these cuts. The times for events satisfying the "zero-sum" requirement are labelled without primes: $T_{\mu^+ \to L_\alpha}$, $T_{L_\alpha \to MCP}$, and $T_{\mu^+ \to MCP}$. Of these three times, only two are independent, i.e. $T_{L_\alpha \to MCP}$ and $T_{\mu^+ \to MCP}$.

5.2 Velocity and Quenching Position of M(2S)

From the time $T_{\mu^+ \to MCP}$ the velocity VEL can be determined, and from the velocity and the time $T_{L_\alpha \to MCP}$ the location of the atom upon emission of the Ly_α photon POS can be determined. These variables, VEL and POS are physically more meaningful, and are therefore easier to make sensible cuts on, than are $T_{\mu^+ \to MCP}$ and $T_{L_\alpha \to MCP}$. The distance from the MWPC to the MCP is well defined and hence the time $T_{\mu^+ \to MCP}$ can be used to determine the velocity. The variable VEL is defined by

$$VEL = \frac{d}{T_{\mu^+ \to MCP}} \tag{5.5}$$

and the variable POS is defined by

$$POS = \frac{T_{L_\alpha \to MCP} \times d}{T_{\mu^+ \to MCP}} = T_{L_\alpha \to MCP} \times VEL \tag{5.6}$$

where d is the distance from the production foil to the MCP. For the microwave experiments the value of d is 26.2 cm. From the definition of POS, an event occurring simultaneously in the Ly_α tubes and the MCP will occur at $POS = 0$.

An event occurring with the time between Ly_α and MCP the same as the time between μ^+ and MCP, will have a value of $POS = d$. The POS variable measures the distance between the location of the atom upon emission of the Ly_α photon and the MCP(see Figure 4.1). For a real 2S muonium atom quenched by the fields we expect that POS should occur in the region of the microwave cavity(or quenching grids) at least to within the timing resolution. There is a further uncertainty in both VEL and POS introduced from variations in the path length from the MWPC to MCP. Taking the extremes of the possible path length, the variation is only 4%. This variation is small compared to the timing resolution. The variation in the propagation time of photons from atoms to the phototubes for atoms radiating at different locations in the cavity is also very small(< 1 ns).

The signal is then defined by placing cuts on both the velocity and position distributions. The velocity range expected for M(2S) formation should be similar to the muonium velocity distribution. From Figure 3.2 we would expect energies below $\sim$ 10 keV, corresponding to a velocity of 0.40 cm/ns. The expected distribution of quench positions would correspond to the location of the cavity. With some reasonable cuts, the signal is R_S is then defined as

$$R_S = R_{ON} - R_{OFF} = \frac{N_{ON}}{\mu_{ON}} - \frac{N_{OFF}}{\mu_{OFF}} \tag{5.7}$$

where $N_{ON(OFF)}$ is defined as the number of counts with the static quenching grids on(off) within the VEL and POS cuts and $\mu_{ON(OFF)}$ is the number of MWPC counts divided by 10^8 with the grids on(off). The rates R_S, R_{ON}, and R_{OFF} are always given per 10^8 MWPC counts.

5.3 Static Field Data

After applying the initial cuts on the times as given by Equation 5.4, and demanding one and only one candidate per trigger satisfy the zero-sum requirement, we can look at the VEL and POS distributions of the remaining events. The velocity distribution of the quenched muonium 2S atoms is given in Figure 5.1 for fairly wide cuts on POS: 4.0 cm $< POS <$ 17.0 cm. The velocity distribution is found

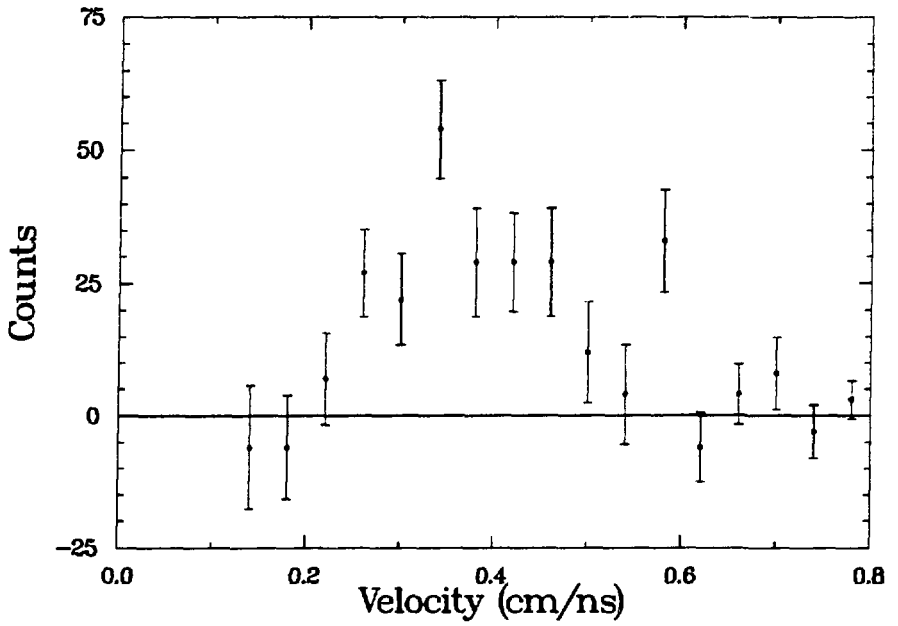

Figure 5.1: Muonium 2S Velocity Distribution from the Static Quenching Data ($1.5\times10^9\mu^+_{ON}$)

not to be very sensitive to the cuts on POS. This distribution is consistent with what is expected for M(2S). The background distribution has a peak at higher velocity (0.55 cm/ns).

The distribution of the decay positions of the M(2S) atoms is shown in Figure 5.2 where the positions of the MWPC, MCP and quenching grids are also drawn. These data have a wide cut on the velocity: 0.10 cm/ns $< VEL <$ 0.70 cm/ns. The position distribution is not very sensitive to the cuts on VEL. The background distribution is flat.

With wide cuts on both VEL and POS: 0.10 cm/ns $\leq VEL \leq$ 0.70 cm/ns and 4.0 cm $\leq POS \leq$ 17.0 cm the M(2S) rate is $R_S = 15.3(2.2)$. This corresponds to 13.3(1.9) muonium events per hour. The background rate with the grids off is $R_{OFF} = 30.6(1.4)$ [26.1(1.2) per hour]. With a narrower set of cuts 0.25 cm/ns $\leq VEL \leq$ 0.50 cm/ns and 7.0 cm $\leq POS \leq$ 17.0 cm, the rate is $R_S = 9.2(1.4)$

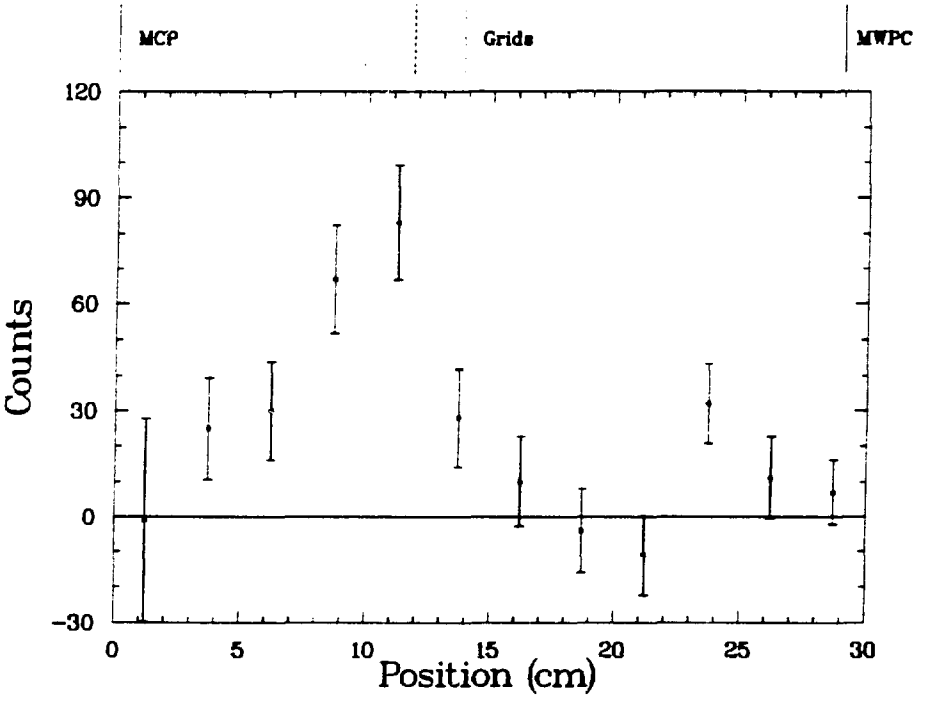

Figure 5.2: Location of the M(2S) Atoms upon Emission of the Ly_α Photon ($1.5\times10^9\mu^+_{ON}$)

	x869	x724
μ^+	24 kHz	70 kHz
Ly_α	64 Hz	38 Hz
MCP	450 Hz	265 Hz
M(2S)	9.2(1.4)/hr	4.7(7)/hr
Bckgd	9.8(0.8)/hr	3.3(4)/hr

Table 5.1: Rate Comparison Between this Experiment and a Previous LAMPF Lamb Shift Experiment

or 8.0(1.2) per hour. The background is reduced to $R_{OFF} = 9.8(0.8)$. In each case the signal is about seven standard deviations. The signal rate with the narrow cuts is an increase of a factor of 2.0(4) compared to a previous LAMPF experiment (x724), the previous rate was 4.7(7)/hr [Bad84b,Woo85]. Experiment 724, using an incident μ^+ momentum of 9.75 MeV/c with a rate of 220 kHz, had a hardware trigger requirement of one and only one μ^+ in 500 ns. In order to prevent pile-up in the trigger the μ^+ rate for x724 was reduced to 70 kHz (730 kHz instantaneous) by use of the jaws upstream of BM03. This loss of a factor of three in muonium rate should be regained by measuring at 7.3 MeV/c with the jaws open, so we would expect a factor of 3 increase in the M(2S) rate. This gain in rate is offset by the reduced μ^+ rate (40% loss) from the asymmetric separator. The background rate is increased by a factor of 3.0(4) [Bad84a]. The increase in background rate is primarily due to the worse separation of e^+ in the beam and may be in part due to the lower energy of the emerging μ^+ beam. The lower-momentum beam emerging from the production foil is less well separated in time from the slower muonium atoms and hence gives a higher number of three-fold coincidences per incident μ^+. A comparison of detector rates between the two experiments is given in Table 5.1.

The data from this experiment are consistent with a 10% M(2S)/M fraction, although there are several poorly-known efficiencies that enter into a determination of the absolute M(2S) yield. For the 24 kHz μ^+ rate, assuming a 10% M(2S) formation, the expected R_S would be 9(4) mHz. The measured rate with the wide windows is 4.3(6) mHz.

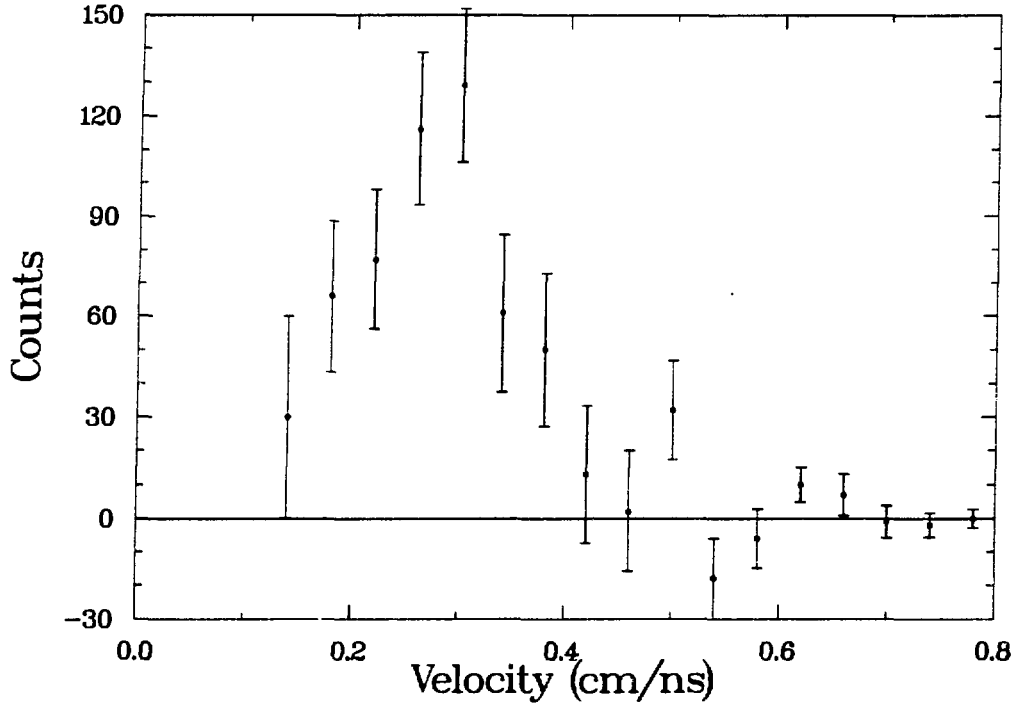

Figure 5.3: Velocity distribution from the RF data ($9.0 \times 10^9 \mu^+_{ON}$)

5.4 Microwave Data

The microwave data are analyzed in the same fashion as the static quench data, with the exception that different cuts on VEL and POS are used. The initial time cuts are given by Equation 5.4. The velocity distribution for the first 50,000 triggers in each of the runs between the frequencies of 9.570 GHz and 10.240 GHz is shown in Figure 5.3. The off resonance data ($\Omega/2\pi \geq 200$ MHz) are not included, as the expected signal is very small, and inclusion of these data (8.995 GHz, 9.470 GHz, and 11.002 GHz) would result in a decrease in the statistical significance of the already small signal.

These data are obtained from a subtraction of R_{OFF} from R_{ON} data; The initial time cut of $0 \leq T_{\mu^+ \rightarrow MCP} \leq 250$ ns cuts off the velocity spectrum below 0.10

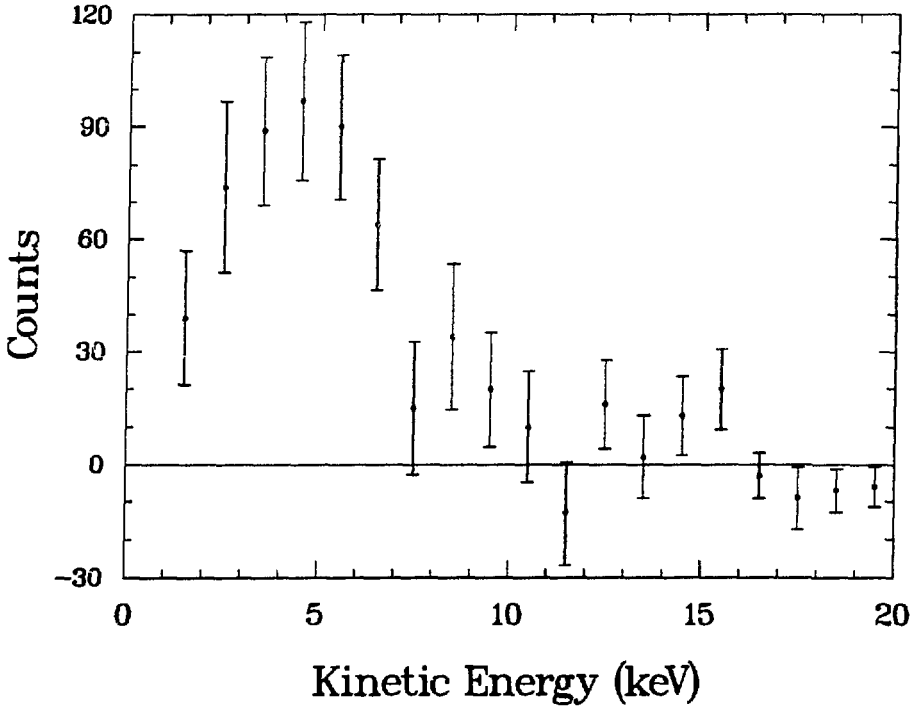

Figure 5.4: Energy distribution from the RF data ($9.0 \times 10^9 \mu^+_{ON}$)

cm/ns. The distribution falls off at lower velocity, indicating that the initial time cut is not cutting signal. The velocity distribution has a cut already applied on the position, such that 4.0 cm $\leq$ POS $\leq$ 17.0 cm. The signal distribution does not change significantly as a function of the position cuts. In an attempt to quantify the change in the velocity distribution as a function of the position cut, the velocity is fit to a Gaussian distribution. The fits are quite good with typical χ^2 per degree of freedom of 0.8. In varying the position cut from a very wide -10.0 cm $\leq POS \leq$ 40.0 cm to a narrow 5.0 cm $\leq POS \leq$ 13.0 cm, the centroid moves from 0.30(2) to 0.27(1) cm/ns. The FWHM of the peak varies from 0.15(4) to 0.17(3) cm/ns.

The kinetic energy distribution of the data is shown in Figure 5.4. This energy distribution can be compared to the expected distribution in Figure 3.2. We see that the signal falls off below 2 keV; this may be due to larger multiple scattering at low energies causing the muonium distribution to emerge at larger angles and,

hence, with fewer arriving at the MCP. There is a software requirement that cuts muonium below 0.6 keV. The velocity distribution from Figure 5.3 is used as a fixed input parameter in the fit to the lineshape (see Section 5.5). Consideration was given to using the velocity distribution from the static field data (see Figure 5.1), which is peaked at slightly higher velocity, in the fits. These data were collected with a different separator and without the cavity, in other words, with different backgrounds. Because of the differences in conditions the velocity distribution from the sum over the RF runs is used in the fit to the RF data.

The "quenching position", or position at which the muonium atom decays from the 2P state to the ground state is plotted for the same RF data in Figure 5.5. These data have a cut on the velocity distribution of 0.10 cm/ns $\leq VEL \leq$ 0.60 cm/ns, but the distribution also does not vary significantly with the choice of cuts. Fitting the position to a Gaussian results in a good χ^2 per degree of freedom of 0.9. As the velocity cuts are varied from 0.0 cm/ns $\leq VEL \leq$ 0.8 cm/ns to 0.20 cm/ns $\leq VEL \leq$ 0.35 cm/ns, the fitted centroid varies from 8.4(6) cm to 8.5(5) cm and the variation in the FWHM is 7.3(1.0)–8.1(1.3) cm. The position of the microwave cavity is plotted in the same figure and extends from 4.0 cm to 17.3 cm. The center of the phototubes are located at 11.8 cm. The actual position of the downstream end of the cavity varies from 4.3–5.7 cm from run to run.

Applying the initial time cuts mentioned above and two sets of final cuts:

- a wide cut which extends from 0.10–0.60 cm/ns and 4.0–17.0 cm and thus encompasses effectively all of the velocity distribution and the entire cavity,
- and a narrow cut, on the FWHM of each distribution, 0.20–0.35 cm/ns and 5.0–13.0 cm,

we find the signal rate as a function of RF frequency listed in Table 5.2.

Several other cuts have been analyzed with the conclusion that the value for the transition frequency is not sensitive to the choice of cuts. The distribution of rates as a function of microwave frequency for a representative sampling of cuts is given in Figure 5.6.

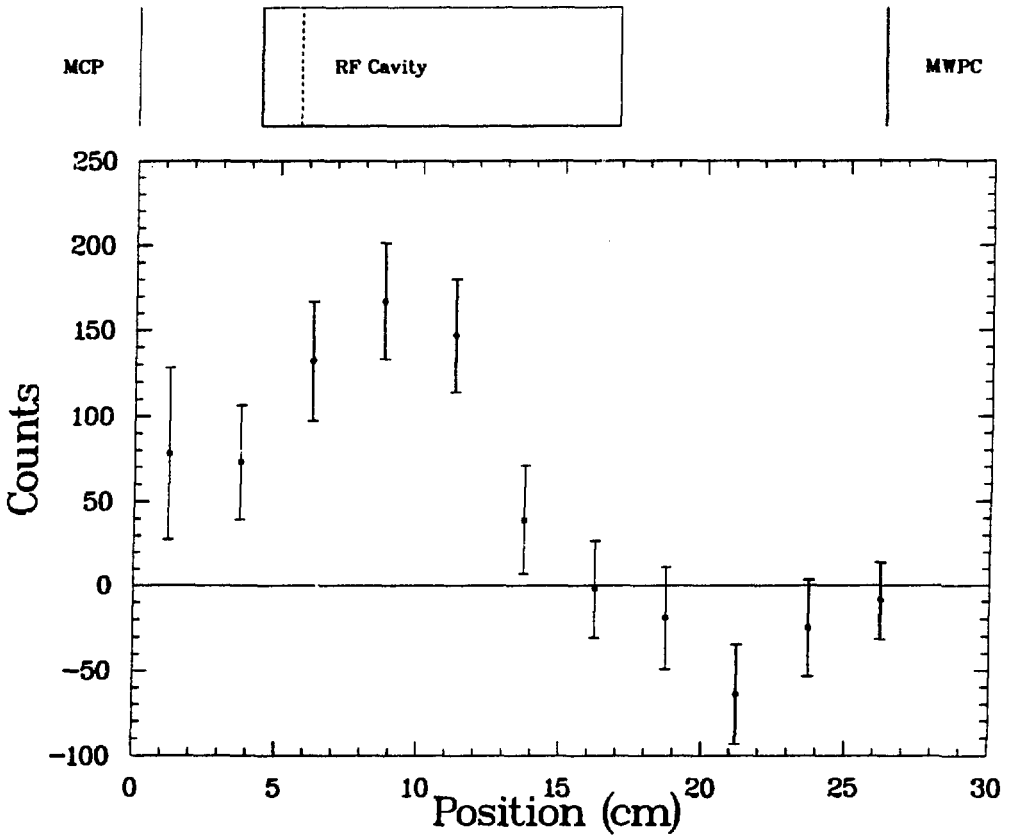

Figure 5.5: Position of the atom when de-excited ($9.0 \times 10^9 \mu^+_{ON}$)

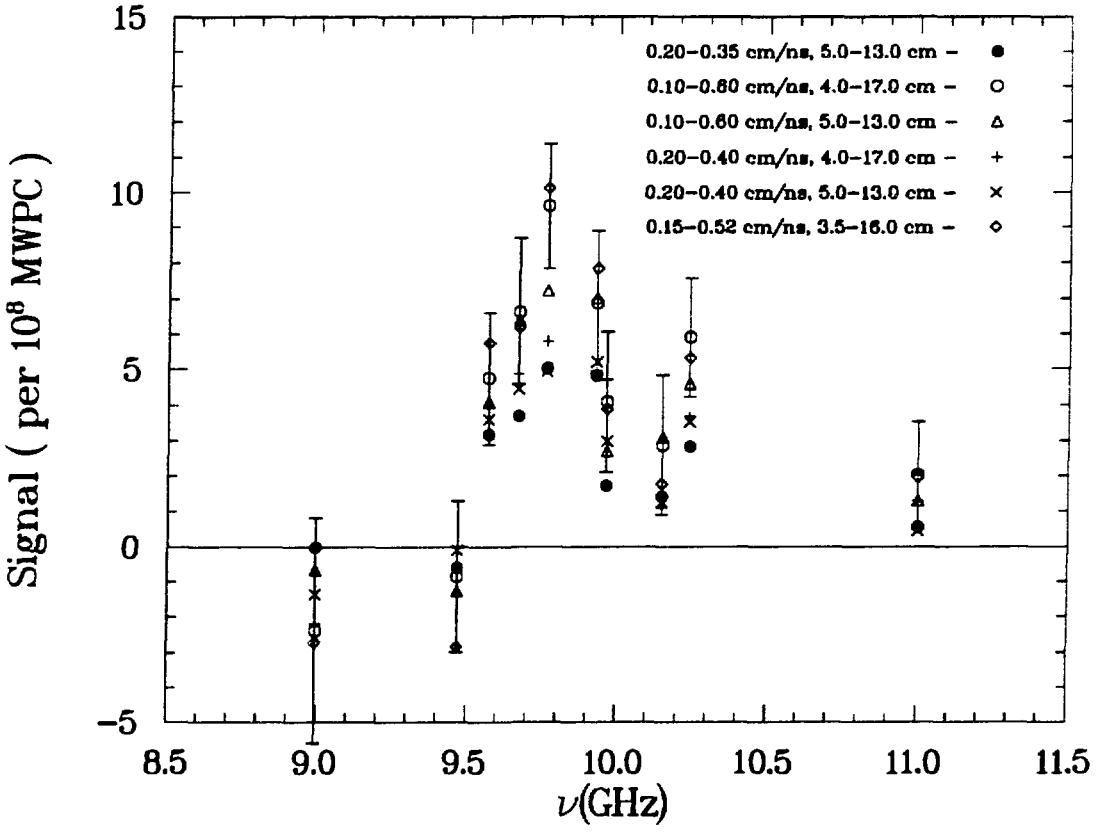

Figure 5.6: Signal rate as a function of microwave frequency for different VEL and POS cuts. The error bars are plotted for the wide cuts.

ν (GHz)	Wide Cuts S (per $10^8\mu^+$)	Wide Cuts R_{OFF} (per $10^8\mu^+$)	Narrow Cuts S (per $10^8\mu^+$)	Narrow Cuts R_{OFF} (per $10^8\mu^+$)
8.995	-2.39(3.21)	31.62(2.31)	-0.01(1.55)	7.10(1.08)
9.470	-0.85(2.14)	28.02(1.52)	-0.59(0.92)	5.41(0.67)
9.570	4.75(1.86)	25.88(1.26)	3.18(0.88)	4.72(0.53)
9.670	6.63(2.05)	35.48(1.38)	3.70(0.95)	6.60(0.59)
9.765	9.61(1.77)	32.24(1.17)	5.02(0.85)	5.90(0.50)
9.770	10.99(2.28)	26.12(1.46)	6.24(1.21)	5.75(0.68)
9.930	6.88(2.01)	37.98(1.36)	4.81(0.97)	7.23(0.59)
9.965	4.08(1.98)	27.46(1.35)	1.72(0.93)	5.72(0.61)
10.150	2.86(1.96)	24.53(1.35)	1.40(0.90)	4.82(0.59)
10.240	5.90(1.68)	25.07(1.13)	2.83(0.86)	5.83(0.54)
11.002	2.02(1.52)	19.99(1.05)	0.56(0.65)	3.51(0.44)

Table 5.2: Table of rates as a function of microwave frequency

5.5 Fit to the Resonance Lineshape

The lineshape is fit by a χ^2 minimization method using the CERNLIB program MINUIT, a global minimization routine [Jam75]. The lineshape that is fit is given by Equation 2.36 where the transitions between different hyperfine levels are summed over. The statistical population of the 2S level is 25% in $|2^2S_{1/2}, 0, 0>$, 25% in $|2^2S_{1/2}, 1, 0>$ and 50% in $|2^2S_{1/2}, 1, \pm 1>$. To account for the depletion of the $|2^2S_{1/2}, 1, \pm 1>$ state to the third level, not accounted for in the two-level approximation, the weighting factor for the two transitions from this state is divided in half. This assures that the maximum quenching of this state is 100%. This treatment introduces an error in the width of the line, which will be added to the error introduced from the uncertainty in the velocity distribution. The line center and the width are seen to be not very correlated (see below), and this approximation should introduce a small error. The natural line width is 100 MHz, but at the average power levels used each line is broadened to 150–250 MHz. The Doppler broadening of the line for the average velocity of 0.30 cm/ns is $\pm$100 MHz. The values of the hyperfine splittings in the 2S and 2P states are given in Section 2.1.3. In the fit to

the lineshape the separations between the resonances is fixed and the value of the $2^2S_{1/2}, F = 1 \rightarrow 2^2P_{3/2}, F = 2$ frequency ν_o is left as a variable parameter in the fit. The simplest approach to fitting the line is to allow for two variable parameters: the line center ν_o and the signal height R_S. R_S is the 2S muonium rate. The other data needed to determine the line shape are the atomic velocity distribution and the microwave field strength. The velocity distribution is obtained from the signal data in Figure 5.3. The average field strength is obtained from the measurements represented by the data in Table 4.2.

The χ^2 function that is fit to is

$$\chi^2 = \sum_{i=1}^{n} \frac{(S(\nu_i) - f(\nu_i; \nu_o, R_S, v, \overline{E}_{108}, \overline{E}_{30n}))^2}{(\Delta S(\nu_i)^2 + (df/d\overline{E}^2 \cdot \Delta\overline{E}^2)^2 + (df/dv \cdot \Delta v)^2} \tag{5.8}$$

where $f = R_S \cdot I$ and I is the quenching probability averaged over the 2S levels. The χ^2 weighting function includes the power and velocity measurement errors, in addition to the statistical error.

Using the data sample from the narrow cuts, the results of the χ^2 minimization, for values of the power and velocity fixed to our measured data, are as follows: a central frequency value of $\nu_o = 9783^{+35}_{-30}$ MHz and a M(2S) rate of $R_s = 7.4(0.7)$. The χ^2 is 12.0 for 9 degrees of freedom. The fit is shown in Figure 5.7. Since the data points were not all taken with the same power, they are scaled to an electric field value of 29.0 V/cm, the value at the 9.765 GHz point, in order to plot them together with the fit. A similar fit using the wide cuts results in a change in the central frequency of only 6 MHz, to 9789^{+39}_{-33} MHz, with a M(2S) rate of 13.9(1.5) and a χ^2 of 7.4 for 9 degrees of freedom.

Several different methods of parameterization of the power have been used. In addition to the fits where we fix the power to our measured values, the power has been allowed to vary with the ratio of field strengths in the different modes fixed to the calculated values. The motivation for two different power parameters arises because the cavity modes do not have the same field distributions across the beam profile (see Section 4.2.6).

Fits have been made with both the average velocity as well as the velocity distribution. In general, the fits are not sensitive to which method is used. The

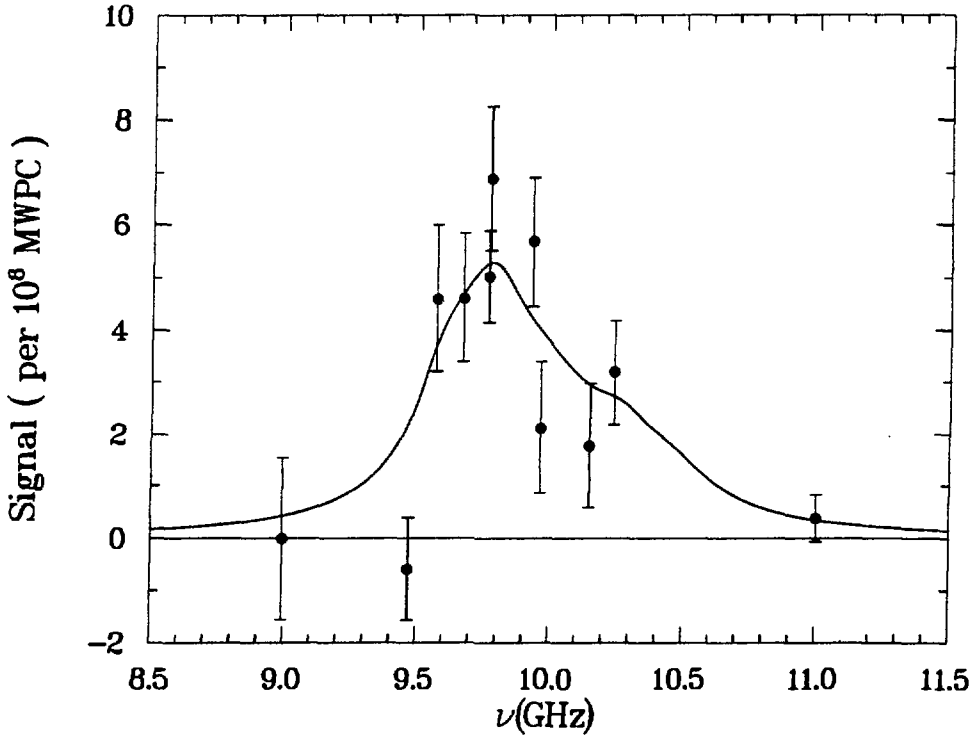

Figure 5.7: Fit to the RF data points.

average velocity depends on the choice of cuts: with the narrow cuts, the average velocity is 0.275(5) cm/ns, and with the wide cuts, the average velocity is 0.289(18) cm/ns.

The other fitting parameters are the line center ν_o and an amplitude parameter R_S. The amplitude parameter is the rate of 2S muonium with which to normalize the quenching probability. This parameter is in general highly correlated to the power parameter. The least correlation is obtained by factoring out the power dependence scaling the expression for the quenching probability and using the amplitude parameter as the only scaling factor. The M(2S) rate is then recovered by dividing out the power.

If the electric field is allowed to vary, the χ^2 is minimized at values for the central frequency that differ by less than 5 MHz for either set of cuts. The ratio of the average electric fields in the two different modes is fixed at the calculated value, which is 0.8(1) for the 9.765 and 9.770 GHz points. The relative fields at the other points in a given mode are scaled from these. The χ^2 minima occurs at: $\nu_o = 9786^{+31}_{-35}$, $\overline{E} = 18.4^{+7.9}_{-12.4}$ V/cm and $R_S = 10.6^{+10.9}_{-15.2}$ for the narrow cuts, with a χ^2 of 10.2 for 8 degrees of freedom. The fit is shown in Figure 5.8, where the data points are all scaled to an electric field of 18.4 V/cm. For the wide cuts we obtain: $\nu_o = 9784^{+34}_{-33}$ MHz, $\overline{E} = 18.5^{+8.7}_{-11.5}$ V/cm and $R_S = 20.0^{+22.3}_{-26.6}$, with a χ^2 of 6.0.

For either choice of cuts, allowing the electric field to vary, while the ratio of the average field strengths in the different mode is fixed at the calculated value, results in a small shift in ν_o and the values for R_S and the variable electric field are reasonably consistent with our measured data.

If both of the electric field parameters are allowed to vary, the χ^2 minimum occurs at values of muonium 2S rates that are unreasonable — at least a factor of three more M(2S) than was observed during the static quench measurement. The values for the central frequency, however, are shifted very little, to 9792 MHz and 9793 MHz for the narrow and wide cuts, respectively.

Further studies of the effects of the power on the value for the central frequency are summarized in Table 5.3. The value of the electric field is varied over a wide range of values. (The field values in column 1 are for the point at 9.765 GHz, whose

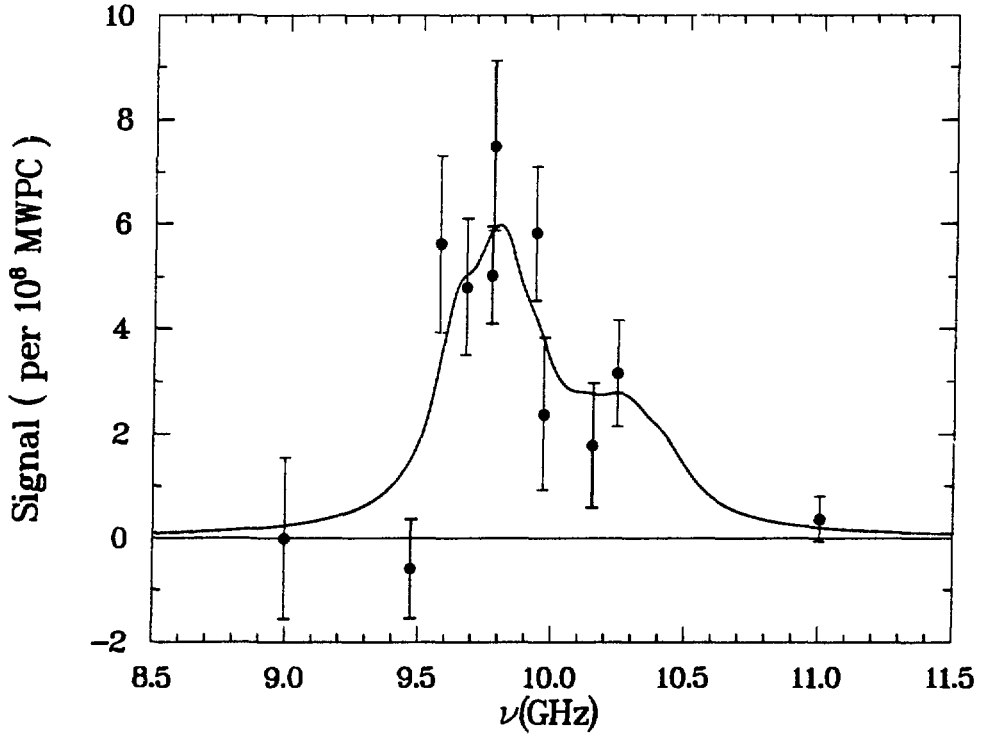

Figure 5.8: Fit to the RF data points.

E_{108} (V/cm)	Narrow Cut ν_o (MHz)	Wide Cut ν_o (MHz)
10	9796^{+18}_{-17}	9795^{+21}_{-22}
15	9794^{+24}_{-28}	9790^{+29}_{-33}
20	9782^{+31}_{-31}	9782^{+34}_{-32}
25	9779^{+32}_{-28}	9784^{+36}_{-32}
30	9784^{+36}_{-30}	9791^{+40}_{-34}
35	9795^{+39}_{-35}	9801^{+43}_{-38}
40	9805^{+38}_{-38}	9812^{+43}_{-42}

Table 5.3: Fits to the Line Center for Different Average Fields

$\|\mathbf{v}\|$	Narrow Cuts ν_o (MHz)	Wide Cuts ν_o (MHz)
v_{ave}	9783^{+35}_{-30}	9789^{+39}_{-33}
$v_{ave}+\sigma$	9778^{+32}_{-28}	9786^{+38}_{-34}
$v_{ave}-\sigma$	9797^{+30}_{-35}	9804^{+41}_{-40}

Table 5.4: Fits to the Line Center for Various Velocities

measured value is 29.0 V/cm.) The table shows the variation in ν_o as the power is varied over a wide range of powers is very small.

Variations in the central frequency caused by varying the average velocity v_{ave} by $\pm\sigma$, where $\sigma = 0.08$ cm/ns is the fitted width of the velocity distribution, are shown in Table 5.4. The average velocity depends on the choice of cuts, with $v_{ave} = 0.289(18)$ cm/ns for the wide cuts and $v_{ave} = 0.275(5)$ cm/ns for the narrow cuts. Again the variation in ν_o is quite small.

The fitted value of the line center ν_o is not very sensitive to the velocity v_{ave}, or the electric field $\overline{E}$, as can be seen in Tables 5.3 and 5.4. Variations in ν_o over reasonable ranges of these parameters are much smaller than the uncertainty in ν_o. Given the lack of sensitivity of the central frequency to wide ranging variations in

the parameters determining the lineshape, it would seem that errors introduced by using the two-level approximation for all 2S sublevels would also have a small effect on the determination of the line center. Corrections from other approximations made in deriving Equation 2.36 are small. Neglect of the counter rotating wave in the rotating wave approximation leads to a shift in the line center. This Bloch-Siegert shift [Blo40] is estimated to be $\sim$ 0.08 MHz. The RF-Stark effect, from mixing with non-resonant states is also estimated to be small $\sim$ 0.06 MHz.

Taking the values of the average electric field fixed at their measured values, the best fit to the data, shown in Figure 5.7, gives

- $\nu_o = 9783^{+35}_{-30}$ MHz and
- $R_S = 7.4(0.7)$.

This value for the frequency of the $2^2S_{1/2}, F = 1 \rightarrow 2^2P_{3/2}, F = 2$ transition is quite insensitive to variations in the values used for the average field or the average velocity.

Chapter 6

Results and Conclusions

The $2^2S_{1/2} \rightarrow 2^2P_{3/2}$ transition has been observed for the first time in the muonium atom. The value from the fit for the $2^2S_{1/2}, F = 1 \rightarrow 2^2P_{3/2}, F = 2$ transition frequency $\nu_o = 9783^{+35}_{-30}$ MHz can be corrected for hyperfine structure to give a value for $2^2S_{1/2} \rightarrow 2^2P_{3/2} = 9895^{+35}_{-30}$ MHz that is in agreement with the theoretical prediction of 9874.3(3) MHz. The theoretical value for the fine structure interval ΔE can then be used to obtain a value for the Lamb shift from this experiment $\mathcal{S} = 1027^{+30}_{-35}$ MHz that is in agreement with the QED calculation of 1047.5(3) MHz. A summary of the result is given in Table 6.1.

Combining this most recent result with previous measured values of the Lamb shift in muonium $\mathcal{S} = 1042^{+21}_{-23}$ [Woo90] and $\mathcal{S} = 1070^{+12}_{-15}$ [Ora84b], we obtain a new value of $\mathcal{S} = 1058^{+10}_{-12}$ MHz. All three measurements are in reasonable agreement with the theoretical prediction, although the TRIUMF measurement is a little more than one standard deviation higher than theory. A summary of the measured values is given in Table 6.2.

This measurement of the $2^2S_{1/2}$–$2^2P_{3/2}$ interval, along with the measurements of the $2^2S_{1/2}$–$2^2P_{1/2}$ interval can be used to obtain a value for the fine structure splitting ΔE. The measured value is $\Delta E = 10957^{+30}_{-30}$ MHz that is in reasonable agreement with the theoretical value of 10921.833(2).

The current experimental precision in the measurement of both $\mathcal{S}$ and ΔE is at the same level as the isotope shift relative to hydrogen. The uncertainty in the

Fit value for $2S_{1/2}$ F=1 $\rightarrow$ $2P_{3/2}$ F=2 transition	9783^{+35}_{-30} MHz
Bloch-Siegert shift	< 0.1 MHz
RF Stark shift	< 0.1 MHz
Adjustment for hyperfine structure	111.8 MHz
$2S_{1/2} \rightarrow 2P_{3/2}$ Measurement	9895^{+35}_{-30} MHz
Adjustment for fine structure $2P_{1/2} \rightarrow 2P_{3/2}$	10921.8 MHz
Lamb shift	1027^{+30}_{-35} MHz
Theory	1047.5(3) MHz

Table 6.1: Measurement of the Lamb Shift

Experimental Measurement	(MHz)
Oram, *et al.*	1070^{+12}_{-15}
Woodle, *et al.*	1042^{+21}_{-23}
This experiment	1027^{+30}_{-35}
Weighted average	1058^{+10}_{-12}
Theory	1047.5(3)

Table 6.2: Summary of Experimental Measurements of the Lamb Shift in Muonium

Lamb shift measurement (10 MHz) is almost three orders of magnitude larger than the uncertainty in the proton size correction(20 kHz) to the Lamb shift in hydrogen.

Some consideration has been given to methods that might improve the experimental sensitivity. The primary difficulty stems from the very low count rate. Some possibilities for an improved Lamb shift measurement include:

- Measure at 30° to the incident beam direction - an experiment measuring the angular distribution of beam foil muonium indicates that the muonium rate does not fall very much at 30° to the beam direction, and that the μ^+ rate does fall substantially. The ratio of M/μ^+ at 30° is $\sim$ 10 times greater than at 0°. With the already low count rates, it is not clear that losing a factor of 30% in the muonium rate is acceptable. The measurement of time zero may become more difficult as fewer positrons will scatter to 30°.

- Drive the transition at 10.24 GHz using a cavity with the wave vector perpendicular to the beam direction - reduction of the Doppler width of the line would allow the measurement of the isolated transition from the $|2^2S_{1/2}, 0, 0>$

sublevel. This line is separated from the others by 558 MHz. The frequency range needed to span this transition is reduced by ~ 7 compared to the overlapping lines driven in this experiment. However, since only 25% of the M(2S) atoms are involved, the rate is down substantially.

- Drive the isolated $2^2S_{1/2} \rightarrow 2^2P_{1/2}$ transition at 580 MHz - this could be driven with a waveguide perpendicular to the beam, reducing the Doppler effect even more. Without a cavity the power levels need to be much higher. In order to maintain a reasonable solid angle for the Ly_α detectors, it would probably be necessary to put the waveguide upstream of the Ly_α tubes and drive a flop out transition. The solid angle from the MWPC to the MCP would therefore be reduced somewhat.

- Improved Lyman α detection - some photosensitive gases, such as NO, have high quantum yields in the Ly_α region. Typically detectors using NO have operated without electron multiplication and did not detect single photoelectrons. There is, however, substantial work in the field of single photoelectron detection in the UV region, primarily for ring imaging Čerenkov detectors. Studies of low pressure MWPC's [Bre85,Sau86] indicate feasibility. Some consideration has also been given to the use of MgF_2 coated Al mirrors [Can66] that would allow the detectors to be moved further from the beam related background.

- Improved M(2S) production - phase space compressed μ^+ beam. For substantial improvement in the measurement of the Lamb shift an improved source of M(2S) must be developed. Taqqu at PSI (Swiss Institute for Nuclear Research) has worked on developing a phase-space compressed muon beam [Taq86]. This scheme makes use of fast detection of the position of the beam, using thin carbon foils as secondary electron emission sources with MCP's for the electron detection, with subsequent pulsing of electromagnetic elements downstream to reduce the transverse momentum of the beam. This is clearly a very ambitious project, but some studies have been made at PSI.

Bibliography

[Agu88] M. Aguilar-Benitez et al., 'Review of particle properties'. Phys. Lett, **204B** (1988).

[Ahn89] H. Ahn, 'Muonium angular distribution'. Yale internal memo, 1989.

[Ama68] J.J. Amato et al., 'Search for spontaneous conversion of muonium to antimuonium'. Phys. Rev. Lett., **21**, 1709 (1968).

[And76] D.A. Andrews and G. Newton, 'Radio-frequency atomic beam measurement of the $(2^2S_{1/2}$,F=0)-$(2^2P_{1/2}$,F=1) Lamb-shift interval in hydrogen'. Phys. Rev. Lett., **37**, 1254 (1976).

[App70] Thomas Appelquist and Stanley J. Brodsky, 'Order α^2 electrodynamic corrections to the Lamb shift'. Phys. Rev. Lett., **24**, 562 (1970).

[Bad84a] A. Badertscher et al., 'Formation of muonium in the 2S state and observation of the Lamb shift transition'. Phys. Rev. Lett., **52**, 914 (1984).

[Bad84b] A. Badertscher et al., 'The Lamb shift in muonium'. In Robert S. Van Dyck, Jr. and Norval E. Fortson, editors, ***Atomic Physics 9***, page 83, (World Scientific, Singapore, 1984).

[Bad85] A. Badertscher et al., 'Development of "subsurface" positive muon beam at LAMPF'. NIM, **A238**, 200 (1985).

[Bar55] W.A. Barker and F.N. Glover, 'Reduction of relativistic two-particle wave equations to approximate forms. III'. Phys. Rev., **99**, 317 (1955).

[Ben77] W.R. Bennett, Jr., *The Physics of Gas Lasers.* (Gordon and Breach, New York, 1977).

[Ber77] H.G. Berry, 'Beam-foil spectroscopy'. Rep. Prog. Phys., **40**, 12 (1977).

[Bet47] H.A. Bethe, 'The electromagnetic shift of energy levels'. Phys. Rev., **72**, 339 (1947).

[Bet77] H.A. Bethe and E.E. Salpeter, *Quantum Mechanics of One- and Two-Electron Atoms.* (Plenum, New York, 1977).

[Bha85] G. Bhatt and H. Grotch, 'Recoil contributions to the Lamb shift in the external- field approximation'. Phys. Rev. A, **31**, 2794 (1985).

[Bha87a] G. Bhatt and H. Grotch, 'Proton recoil and radiative level shifts'. Phys. Rev. Lett., **58**, 471 (1987).

[Bha87b] G. Bhatt and H. Grotch, 'Radiative-recoil corrections to the Lamb shift'. Ann. Phys., **178**, 1 (1987).

[Bir89] F. Biraben et al., 'New measurement of the Rydberg constant by two-photon spectroscopy of hydrogen Rydberg states '. Phys. Rev. Lett., **62**, 621 (1989).

[Blo40] F. Bloch and A. Siegert, 'Magnetic resonance for nonrotating fields'. Phys. Rev., **57**, 522 (1940).

[Bol81] P.R. Bolton et al., 'Observation of muonium in vacuum'. Phys. Rev. Lett., **47**, 1441 (1981).

[Bol82] Paul R. Bolton, *Production of Muonium in Vacuum.* PhD thesis, Yale University, 1982.

[Bre77] A. Breskin, 'A subnanosecond, low pressure MWPC for heavily ionizing particles'. NIM, **141**, 505 (1977).

[Bre84] A. Breskin et al., 'On the low-pressure operation of multistep avalanche chambers'. NIM, **220**, 349 (1984).

[Bre85] A. Breskin and R. Chechik, 'Detection of single electrons and low ionization radiation with low-pressure multistep chambers'. IEEE Trans. Nucl. Sci., **NS-32**, 504 (1985).

[Bro77] K.L. Brown et al., *TRANSPORT, A computer program for designing charged particle beam transport systems.* Technical Report SLAC-91, Rev. 2 UC-28, SLAC, 1977.

[Byr70] F.W. Byron et al., 'Quenching of metastable hydrogen'. Phys. Rev. Lett., **24**, 83 (1970).

[Can66] L.R. Canfield et al., 'Further studies on MgF_2-overcoated aluminum mirrors with highest reflectance in the vacuum ultraviolet'. Appl. Opt., **5**, 45 (1966).

[Chu88] Steven Chu et al., 'Laser excitation of the muonium 1S–2S transition'. Phys. Rev. Lett., **60**, 101 (1988).

[Coh87] E. Richard Cohen and Barry N. Taylor, 'The 1986 adjustment of the fundamental physical constants'. Rev. Mod. Phys., **59**, 1121 (1987).

[Com83] E.D. Commins and P.H. Bucksbaum, *Weak interactions of leptons and quarks.* (Cambridge University Press, Cambridge, 1983).

[Cos70] B.L. Cosens and T.V. Vorburger, 'Remeasurement of the $2^2S_{1/2}$–$2^2P_{3/2}$ splitting in atomic hydrogen'. Phys. Rev., **A2**, 16 (1970).

[Day53] Edward S. Dayhoff, Sol Triebwasser, and Willis E. Lamb, Jr., 'Fine structure of the hydrogen atom. Part VI'. Phys. Rev., **89**, 106 (1953).

[Don83] J.B. Donahue, 'Radioactive gas'. LAMPF internal memo, September 1983.

[Eri77] G.W. Erickson, 'Energy levels of one-electron atoms'. J. Phys. Chem. Ref. Data, **6**, 831 (1977).

[Eri88] G.W. Erickson and H. Grotch, 'Lamb-shift recoil effects in hydrogen'. Phys. Rev. Lett., **60**, 2611 (1988).

[Ful54] Thomas Fulton and Paul C. Martin, 'Two-body system in quantum electrodynamics. Energy levels of positronium'. Phys. Rev., **95**, 811 (1954).

[Gab81] G. Gabrielse, 'Measurement of the n=2 density operator for hydrogen atoms produced by passing protons through thin carbon targets'. Phys. Rev., **A23**, 775 (1981).

[Gao84] R.S. Gao et al., 'Absolute and angular efficiencies of a microchannel-plate position-sensitive detector'. Rev. Sci. Inst., **55**, 1756 (1984).

[Gla61] S.L. Glashow, 'Partial-symmetries of weak interactions'. Nucl. Phys., **22**, 579 (1961).

[Gro69] H. Grotch and D.R. Yennie, 'Effective potential model for calculating nuclear correction s to the energy levels of hydrogen'. Rev. Mod. Phys., **41**, 350 (1969).

[Gro88] H. Grotch, 'The Lamb shift in hydrogen'. Phys. Scr., **T21**, 86 (1988).

[Ham83] Hamamatsu, *Hamamatsu Technical Specification.* Hamamatsu Corporation, 1983.

[Han63] L.N. Hand et al., 'Electric and magnetic form factors of the nucleon'. Rev. Mod. Phys., **35**, 335 (1963).

[Hub88] T.H. Huber et al., 'Search for the conversion of muonium to anti-muonium'. Phys. Rev. Lett., **61**, 2189 (1988).

[Hub89] T.H. Huber et al., 'Search for the conversion of muonium to anti-muonium'. 1989, to be published in Proceedings of the Rare Decay Symposium, TRIUMF.

[Hug60] V.W. Hughes et al., 'Formation of muonium and observation of its Larmor precession'. Phys. Rev. Lett., **5**, 63 (1960).

[Hug72] E.B. Hughes et al., 'Properties and applications of large NaI(Tl) total absorption spectrometers '. IEEE Trans. Nucl. Sci., **NS-19**, 126 (1972).

[Hug77] V.W. Hughes and T. Kinoshita, 'Electromagnetic properties and interactions of muons'. In V.W. Hughes and C.S. Wu, editors, *Muon Physics I*, page 12, (Academic Press, New York, 1977).

[Jac75] J.D. Jackson, *Classical Electrodynamics*. (John Wiley and Sons, New York, 1975).

[Jam75] F. James and M. Roos, 'MINUIT - A system for function minimization and analysis of the parameter errors and correlations'. Comp. Phys. Com., **10**, 343 (1975).

[Kau71] S.L. Kaufman et al., 'Measurement of the $2^2S_{1/2}$–$2^2P_{3/2}$ interval in atomic hydrogen'. Phys. Rev., **A4**, 2128 (1971).

[Kin84] T. Kinoshita and J. Sapirstein, 'New developments in QED'. In Robert S. Van Dyck, Jr. and Norval E. Fortson, editors, *Atomic Physics 9*, page 38, (World Scientific, Singapore, 1984).

[Kla73] S. Klarsfeld and A. Maquet, 'Bethe sums for Lamb shift calculations in higher excited states '. Phys. Lett., **43B**, 201 (1973).

[Kua87] Y. Kuang et al., 'First observation of the negative muonium ion produced by electron capture in a beam foil experiment'. Phys. Rev., **A35**, 3172 (1987).

[Kua88] Yunan Kuang, *Observation of the Negative Muonium Ion in Vacuum*. PhD thesis, Yale, 1988.

[Kua89] Y. Kuang et al., 'Formation of the negative muonium ion and charge exchange processes for positive muons passing through thin metal foils'. Phys. Rev., **A39**, 6109 (1989).

[Kus59] P. Kusch and V.W. Hughes, 'Atomic and molecular beam spectroscopy'. In S. Flügge, editor, *Encyclopedia of Physics*, page 1, (Springer-Verlag, Berlin, 1959).

[Lam47] Willis E. Lamb, Jr. and R.C. Retherford, 'Fine structure of the hydrogen atom by a microwave method'. Phys. Rev., **72**, 241 (1947).

[Lam50] Willis E. Lamb, Jr. and Robert C. Retherford, 'Fine structure of the hydrogen atom. Part I'. Phys. Rev., **79**, 549 (1950).

[Lam51] Willis E. Lamb, Jr. and Robert C. Retherford, 'Fine structure of the hydrogen atom. Part II'. Phys. Rev., **81**, 222 (1951).

[Lam52a] Willis E. Lamb, Jr., 'Fine structure of the hydrogen atom. Part III'. Phys. Rev., **85**, 259 (1952).

[Lam52b] Willis E. Lamb, Jr. and Robert C. Retherford, 'Fine structure of the hydrogen atom. Part IV'. Phys. Rev., **86**, 1014 (1952).

[Lep84] G.P. Lepage and D.R. Yennie, 'The implications of QED theory for the fundamental constants'. In B. N. Taylor and W.D. Phillips, editors, *Precision Measurement and Fundamental Constants II*, page 185, National Bureau of Standards, (U.S. Department of Commerce, August 1984). NBS Special Publication 617.

[Lun81] S.R. Lundeen and F.M. Pipkin, 'Measurement of the Lamb shift in hydrogen, n=2'. Phys. Rev. Lett., **46**, 232 (1981).

[Mar82] F.G. Mariam et al., 'Higher precision measurement of the hfs interval in muonium and of the muon magnetic moment'. Phys. Rev. Lett., **49**, 993 (1982).

[Mic50] L. Michel, 'Interaction between four half-spin particles and the decay of the μ-meson'. Proc. Phys. Soc., **A63**, 514 (1950).

[Moh75] Peter J. Mohr, 'Lamb shift in a strong coulomb potential'. Phys. Rev. Lett., **34**, 1050 (1975).

[Mon47] Carol G. Montgomery, editor, *Technique of Microwave Measurements*. Volume 11 of *MIT Radiation Laboratory Series*, (McGraw-Hill, New York, 1947).

[MP186] MP-1-Group, *FLECS and ALECS User's Manual*. LAMPF, mp-1-3415 edition, 1986.

[MP187] MP-1-Group, *Q Release Notes and Distribution Information*. LAMPF, mp-1-3413-4 edition, 1987.

[Mun89] H.-J. Mundinger et al., 'Search for the conversion of muonium to anti-muonium'. 1989, to be published in Proceedings of the Rare Decay Symposium, TRIUMF.

[Ni87] B. Ni et al., 'Search for spontaneous conversion of muonium to antimuonium'. Phys. Rev. Lett., **59**, 2716 (1987).

[Ora84a] C. J. Oram, 'Measurement of the Lamb shift in muonium: The TRIUMF experiment'. In Robert S. Van Dyck, Jr. and Norval E. Fortson, editors, *Atomic Physics 9*, page 75, (World Scientific, Singapore, 1984).

[Ora84b] C.J. Oram et al., 'Measurement of the Lamb shift in muonium'. Phys. Rev. Lett., **52**, 910 (1984).

[Ort85] H. Orth and P. Koch, 'Studies of MCP efficiency for p^+ and H'. 1985, Internal Yale memo on work done at Stonybrook.

[Owe86] D.A. Owen, 'Lamb shift in muonium: a review of theory and experiment'. Ann. Phys. Fr., **11**, 249 (1986).

[Pal83] V.G. Pal'chikov, Yu.L. Sokolov, and V.P. Yakovlev, 'Measurement of the Lamb shift in the hydrogen atom (n=2)'. JETP Lett., **38**, 418 (1983).

[Phi55] James A. Phillips, 'Charge equilibrium ratios of hydrogen ions from solids'. Phys. Rev, **97**, 404 (1955).

[Pif76] A.E. Pifer et al., 'A high stopping density μ^+ beam'. NIM, **135**, 39 (1976).

[Ram56] Norman F. Ramsey, *Molecular Beams.* (Oxford University Press, Oxford, 1956).

[Rei78] H.-W. Reist et al., 'Development of a low-momentum "surface" muon beam for LAMPF'. NIM, **153**, 61 (1978).

[Saf80] K.A. Safinya et al., 'Measurement of the $2^2P_{3/2}$–$2^2S_{1/2}$ fine-structure interval in atomic hydrogen'. Phys. Rev. Lett., **45**, 1934 (1980).

[Sal51] E.E. Salpeter and H.A. Bethe, 'A relativistic equation for bound-state problems'. Phys. Rev., **84**, 1232 (1951).

[Sal52] E.E. Salpeter, 'Mass corrections to the fine structure of hydrogen-like atoms'. Phys. Rev., **87**, 328 (1952).

[Sal68] A. Salam, 'Weak and electromagnetic interactions'. In *'Elementary Particle Theory: Relativistic Groups and Analyticity'*, page 367, (Almqvist and Wiskell, Stockholm, 1968). Nobel Symposium 8.

[Sam67] J.A.R. Sampson, *Techniques of Vacuum Ultraviolet Spectroscopy.* (Wiley, New York, 1967).

[Sap83] J.R. Sapirstein, '$\alpha(Z\alpha)^2 E_F$ Binding corrections to hyperfine splitting in hydrogenic atoms'. Phys. Rev. Lett., **51**, 985 (1983).

[Sau77] F. Sauli, *Principles of Operation of Multiwire Proportional and Drift Chambers.* Technical Report 77–09, CERN, 1977.

[Sau86] F. Sauli, 'Ultraviolet photon detection and localization with multiwire chambers'. NIM, **A248**, 143 (1986).

[Shl74] Sally Shlaer, *An MBD Primer.* Technical Report LA-5511-MS, LASL, 1974.

[Shy71] T.W. Shyn et al., 'Measurement of the $2^2S_{1/2}$–$2^2P_{3/2}$ energy separation (ΔE - S) in hydrogen (n=2)'. Phys. Rev., **A3**, 116 (1971).

[Sim80] G.G. Simon et al., 'Absolute electron-proton cross sections at low momentum transfer measured with a high pressure gas target system'. Nucl. Phys., **A333**, 381 (1980).

[Ste60] R.M. Sternheimer, 'Range straggling of charged particles in Be,C,Al,Cu, Pb, and air'. Phys. Rev., **117**, 485 (1960).

[Taf57] E.A. Taft and H.R. Philipp, 'Photoelectric emission from the valence band of some alkali halides'. J. Phys. Chem. Solids, **3**, 1 (1957).

[Taq86] D. Taqqu, 'Phase space compression of muon beams'. NIM, **A247**, 288 (1986).

[Tho79] P.A. Thompson et al., 'The stopped muon channel at LAMPF'. NIM, **161**, 391 (1979).

[Tri53] Sol Triebwasser, Edward S. Dayhoff, and Willis E. Lamb, Jr., 'Fine structure of the hydrogen atom. Part V'. Phys. Rev., **89**, 98 (1953).

[Tro66] W. Peter Trower, *'High Energy Particle Data IV Range-Momentum and dP/dx Plots of Charged Particles in Matter.* Technical Report UCRL-2426, Lawrence Radiation Laboratory, 1966.

[Ueh35] E.A. Uehling, 'Polarization effects in the positron theory'. Phys. Rev., **48**, 55 (1935).

[Wei67] S. Weinberg, 'A model of leptons '. Phys. Rev. Lett., **19**, 1264 (1967).

[Wil79] M.W. Williams and E.T. Arakawa, 'Optical properties of crystalline MgF_2 from 115nm to 400nm'. Appl. Opt., **18**, 1477 (1979).

[Wiz79] J.L. Wiza, 'Microchannel plate detectors'. NIM, **162**, 587 (1979).

[Woo85] Kim A. Woodle, *Part I. Measurement of the Lamb Shift in Muonium.* PhD thesis, Yale, 1985.

[Woo90] K.A. Woodle et al., 'Measurement of the Lamb shift in the n = 2 state of muonium'. Phys. Rev., **A41**, 93 (1990).

*U.S. GOVERNMENT PRINTING OFFICE 1990-0-773-034/20069